Title
Kernel-based anatomical image-guided optical tomographic reconstruction

Author
Baikejiang, Reheman

Publication Date
2017

Peer reviewed|Thesis/dissertation

UNIVERSITY OF CALIFORNIA, MERCED

Kernel-based anatomical image-guided optical tomographic reconstruction

A dissertation submitted in partial satisfaction of the
requirements for the degree
Doctor of Philosophy

in

Biological Engineering and Small-scale Technologies

by

Reheman Baikejiang

Committee in charge:

Professor Changqing Li, Chair
Professor Arnold D. Kim
Professor Roummel F. Marcia
Professor Wei-Chun Chin

2017

The dissertation of Reheman Baikejiang is approved, and it is acceptable in quality and form for publication on microfilm and electronically:

(Professor Arnold D. Kim)

(Professor Roummel F. Marcia)

(Professor Wei-Chun Chin)

(Professor Changqing Li, Chair)

University of California, Merced

2017

DEDICATION

To my wife Xamxikamer and daughter Besire

TABLE OF CONTENTS

LIST OF FIGURES

LIST OF TABLES

ACKNOWLEDGEMENTS

When I was looking for a research project during my first year at the University of California, Merced, I came across the website of Professor Changqing Li's Biomedical Imaging Lab. The multidisciplinary aspect and clinical applicabilities of Professor Li's research captured my attention. I have been truly fortunate to be one of the early members of this lab and to be able to work in a great environment created by Professor Li. It is my great pleasure to acknowledge all of the lab members for enriching both academic and personal aspects of my life.

Professor Li is an expert in the field of biomedical optics. Despite his busy schedule, is always able to help me and my fellow graduate students. His critical scientific insights have challenged and directed me to strive for intellectual advancement. He has taught me how to deliver a compelling presentation with clarity and how to write scientific papers and grants. In addition to my advisor, I thank my academic committee members: Professors Arnold D. Kim, Roummel F. Marcia, and Wei-Chun Chin. Their comments and suggestions have been very helpful toward my studies and research. They provided the research direction and inspired me greatly along the way.

Furthermore, I would like to thank my colleagues in the biomedical imaging lab at UC Merced. I would like to express special thanks to Ms. Yue Zhao, who conducted FMT data acquisition and collaborated on several projects; Dr. Dianwen Zhu, who taught me image reconstruction algorithms; and Dr.Wei Zhang for his help on DOT instrumentation design and experiments.I also thank my collaborator Mr. Andre M. Hernandez from the University of California, Davis for conducting phantom CT scans, and Mr. Brett Z. Fite from the University of California, Davis for performing rat brain MRI scans. I am very grateful to Professors. Jinyi Qi, Guobao Wang, John M. Boone, Shadi Aminololama Shakeri, and Ramsey D. Badawi at the University of California, Davis for helpful discussions and fruitful collaborative work. I also thank my colleague Michael Lun and former lab member Kun Zhang for providing the friendliest atmosphere anyone can imagine. It has been a blessing to have you all around.

Finally, I would like to thank other friends and family members for keeping

tabs on me. Most importantly, my sincerest thanks to my lovely wife Xamxikamer and daughter Besire.

This dissertation research received financial support in the form of several summer fellowships and travel awards from the graduate program of Biological Engineering and Small Technologies (BEST), School of Engineering, UC Merced. Outstanding Self-Financed Students Studying Abroad Award from Xinjiang, China. I also acknowledge research support from California Breast Cancer Research Program (IDEA: 20IB-0125).

VITA

Ph.D. Candidate in Biological Engineering and Small-scale Technologies

University of California, Merced 2012 - 2017

M.S. in Applied Mathematics

Osaka University, Japan 2009 - 2012

B.S. in Information and Computational Science

Xinjiang University, China 2001 - 2006

PUBLICATIONS

R. Baikejiang, W. Zhang, D. Zhu, A. M. Hernandez, S. A. Shakeri, G. Wang, J. Qi, and C. Li, "Kernel-based anatomically-aided diffuse optical tomography reconstruction," *Biomed Phys Eng Express* [Submitted]

R. Baikejiang, Y. Zhao, B. Z. Fite, K. W. Ferrara, and C. Li, "Anatomical image guided fluorescence molecular tomography reconstruction using kernel method," *J. Biomed. Opt* **22**(5), 055001 (2017)[doi:10.1117/1.JBO.22.5.055001].

R. Baikejiang, W. Zhang, and C. Li, "Gaussian kernel based anatomically-aided diffuse optical tomography reconstruction," *Proc. SPIE* **10059**, 1005912 (2017) [doi:10.1117/12.2252786].

Y. Zhao, **R. Baikejiang**, and C. Li, "Application of kernel method in fluorescence molecular tomography," *Proc. SPIE* **10057**, 100570P (2017) [doi:10.1117/12.2252782].

R. Baikejiang, W. Zhang, and C. Li, "Diffuse optical tomography for breast cancer imaging guided by computed tomography: a feasibility study," *J. Xray. Sci. Technol* **25**(3),341–355 (2017) [doi:10.3233/XST-16183].

R. Baikejiang, W. Zhang, D. Zhu, and C. Li,"CT guided diffuse optical tomography for breast cancer imaging," *Proc. SPIE* **9788**, 97882K (2016) [doi:10.1117/12.2216402].

Y. Zhao, D. Zhu, **R. Baikejiang**, and C. Li, "3D mouse shape reconstruction based on phase-shifting algorithm for fluorescence molecular tomography imaging system," *Appl. Opt.* **54**(32), 9573–9582 (2015) [doi:10.1364/AO.54.009573].

Y. Zhao, D. Zhu, **R. Baikejiang**, and C. Li, "Fluorescence molecular imaging system with a novel mouse surface extraction method and a rotary scanning scheme," *Proc. SPIE* **9319**, 93190T (2015) [doi:10.1117/12.2076476].

D. Zhu, Y. Zhao, **R. Baikejiang**,Z. Yuan, and C. Li, "Comparison of regularization methods in fluorescence molecular tomography," *Photonics* **1**(2), 95–109 (2014) [doi:10.3390/photonics1020095].

ABSTRACT OF THE DISSERTATION

Kernel-based anatomical image-guided optical tomographic reconstruction

by

Reheman Baikejiang

Doctor of Philosophy in Biological Engineering and Small-scale Technologies

University of California Merced, 2017

Professor Changqing Li, Chair

Optical tomography, specifically, diffuse optical tomography (DOT) and fluorescent molecular tomography (FMT) are promising functional imaging modalities with a high sensitivity and specificity. However, the inverse problem of DOT and FMT are ill-posed and ill-conditioned due to strong optical scattering in deep tissues, which results in poor spatial resolution for deep target imaging. It is well known that DOT and FMT image quality can be improved substantially by applying structural guidance in the reconstruction algorithm.

In this dissertation, First, I conducted a feasibility study of computed tomography (CT) guided DOT system for breast cancer imaging. I built a noncontact projection style prototype DOT which consists of a laser at the wavelength of 650 nm and an electron multiplying charge coupled device (EMCCD) camera. We have validated the CT-guided DOT reconstruction algorithms with numerical simulations and phantom experiments, in which different imaging setup parameters, such as projection number of measurements and width of measurement patch, have been investigated.

Secondly, inspired by the kernel methods in machine learning, I introduced a kernel-based image reconstruction algorithm into anatomical image-guided DOT. Compared with conventional Laplacian approaches that include structural priors by regularization matrix, the developed method applied in this research incorpo-

rates a kernel matrix with the projection model into the objective function and does not require image segmentation. The optical absorption coefficient at each finite element node is represented as a function of a set of features obtained from anatomical images such as computed tomography (CT) images. The proposed kernel method is validated with numerical simulations and agar phantom experiments. The proposed method utilized a CT volume data set without segmentation from a clinical breast CT system in the DOT.

Lastly, I implemented kernel-based anatomical guidance into the FMT image reconstruction. In FMT, the fluorophore concentration at each node is defined as a function of a set of feature vectors, which is directly extracted from the voxel intensities of the corresponding anatomical 3D images. This research studied the effects of voxel size and a number of nearest neighbors in the kernel method on the quality of reconstructed FMT images. The results indicate that the spatial resolution and the accuracy of the reconstructed FMT images have been improved substantially after applying the anatomical guidance with the proposed kernel method. The proposed method utilized magnetic resonance imaging (MRI) rat brain image in FMT simulation, which further proved that we do not need to segment the anatomical image for the kernel method. The proposed kernel method was found to be robust to the false positive guidance in the anatomical image.

As future work, the DOT prototype system will be integrated with a dedicated CT system, and clinical trials will be conducted using kernel-based image reconstruction algorithm.

Chapter 1

Overview

1.1 Optical tomography

1.1.1 Introduction to optical tomography

Optical tomography has been a rapidly developing technology in biomedical imaging for the last few decades[1, 2, 3]. Optical tomography utilizes non-ionizing Near-infrared (NIR) photons in the wavelength range from 650 to 950 nm[4]. In this range, biological tissues especially soft tissues such as breast and brain tissues, are relatively transparent, which enables the detection of transmitted photons through the tissue[5]. Optical absorption spectra vary with the oxygenation and deoxygenation states of hemoglobin (Hb) which is related to hypermetabolism[6]. Hemoglobin concentration itself relates to the angiogenesis[6]. Both hypermetabolism and angiogenesis are the major physiological markers of cancers due to the fast cancer cell proliferation[7]. Therefore, optical absorption serves as intrinsic contrast for functional imaging. Besides absorption, optical scattering spectra provide information about the size distribution of optical scattering particles such as organelles in tissue, which potentially reveals cellular structure changes of the cancerous tissues[8].

Optical tomography is significantly different from microscopic imaging which based on unscattered or slightly backscattered ballistics(coherent) photons[9]. High spatial resolution (a fraction of μm) is the main advantages of ballistic imaging.

However, ballistic imaging constrained to a depth from where ballistic and/or snake photons can be detected by the detectors which is usually less than one millimeter[10]. Optical tomography can reach to little bit depth, up to several centimeters (cm). There are numbers of techniques belong to the optical tomography category. Here I briefly discuss few of them:

Optical coherence tomography (OCT)

OCT is a tomographic technique suitable for the imaging of surface layers of highly scattering, nontransparent samples, as probing is obtained from backscattered photons[11]. Basically, it comprises of a short-coherence light source and an interferometer with one well-defined reference arm and a probe arm that is directed into the sample[12]. OCT is analogous to ultrasonography. Spatial resolution is in the range of a few micrometers(1 to 10µm) and penetration depth also reaches up to a few millimeters(1-2 mm)[13].

Diffuse optical tomography (DOT)

DOT is suitable for samples larger than those used in OCT, such as human breast and infant's brain[14]. DOT allows for a spatially resolved analysis of optical scattering and absorption properties, which is required for quantitative assessment of functional parameters such as total hemoglobin and hemoglobin oxygenation. The spatial resolution of DOT is in the order of 20% of the imaging depth[9].

Fluorescent molecular tomography (FMT)

FMT is a special case of DOT since the physics for diffusive photon propagation is identical. Instead of recovering intrinsic contrasts, FMT recovers extrinsic contrasts such as fluoresce dye concentration[15]. It has better spatial resolution than DOT, but require fluorescent dye injection. Currently it is suitable for small animal imaging due to the toxicity of the contrast agents.

Photoacoustic tomography (PAT)

PAT can treated as a hybrid imaging modality among optical imaging and ultrasonic imaging, because the spatial resolution is determined by the acoustic signals that are from optical absorbers excited by a short pulsed laser[9]. Due to its hybrid nature, PAT overcomes the limitations of optical scattering thus can image the optical absorbers at a superfine spatial resolution of ultrasonic imaging, while it still has the limitations of acoustic imaging such as air-tissue interface problem.

Ultrasound-modulated optical tomography (UOT)

UOT is another hybrid imaging technique that takes advantage of both optical contrast and ultrasonic resolution[9]. In UOT, some of the scattered photons are temporarily modulated by a focused ultrasonic wave inside the biological tissue, which results in phase and frequency shift of transmitted photons. Such modulated photons can be discriminated from background un-modulated photons, and their origins can be directly derived from the position of the ultrasonic column inside the tissue[16]. UOT allows recovering optical contrast at depths of few centimeters with a millimeter resolution[9].

X-ray luminescence computed tomography (XLCT)

XLCT is an emerging hybrid imaging modality in which X-ray photons are used to excite phosphors emitting optical photons that are measured for optical tomography imaging[17, 18, 19]. The X-ray beam position and size are used as anatomical guidance in the optical reconstruction[20]. XLCT is possible to have the high sensitivity of optical imaging and high spatial resolution of X-ray imaging[21]. Recently, it has been demonstrated that a 23 mm deep target with a concentration of 0.01 mg/mL could be reconstructed successfully, which indicate that XLCT is suitable to image a mouse-sized object[22].

This dissertation focus on two applications of optical tomography in biomedical imaging, namely: DOT and FMT.

1.1.2 Photon transport and diffusion theory

Most biological tissues are characterized by strong optical scattering and week absorption in the optical wavelength range from 650 to 1000 nm. Photon propagation through highly scattering media can be modeled analytically by the radiative transfer equation (RTE), also known as Boltzmann transport equation. Neglecting coherence, polarization and non-linearity, the RTE can be derived from the principle of conservation of energy. Assuming optical properties such as refractive index, absorption coefficient, scattering coefficient and scattering anisotropy are time-invariant but space variant, RTE is written as[23, 24]

$$\left(\frac{1}{c}\frac{\partial}{\partial t} + \hat{s}\cdot\nabla + \mu_t\right) L(\vec{r},\hat{s},t) = \mu_s \int_{4\pi} L(\vec{r},\hat{s},t)P(\hat{s}'\cdot\hat{s})d\Omega' + S(\vec{r},\hat{s},t), \quad (1.1)$$

where $L(\vec{r},\hat{s},t)$ is the radiance at position $\vec{r}$, at time t, propagating along the unit direction vector $\hat{s} = (\sin\theta\cos\phi, \sin\theta\sin\phi, \cos\theta)$, where θ and ϕ denote the polar and azimuthal angles, respectively. The unit of radiance is the watt per steradian per square meter (W m^{-2} sr^{-1}). $\mu_t = \mu_a + \mu_s$ is the extinction coefficient. μ_a and μ_s, the absorption and scattering coefficients, are the inverse of the absorption and scattering mean free path respectively. c is the speed of light in the medium. The phase function $P(\hat{s}'\cdot\hat{s})$ is the probability density function and the product $P(\hat{s}'\cdot\hat{s})d\Omega$ represents the probability of light with propagation direction $\hat{s}'$ being scattered into the $d\Omega$ around direction $\hat{s}$. $S(\vec{r},\hat{s},t)$ is the source radiance.

The intro-differential equation above is hard to be solved deterministically since it has six degree of freedom, three in space, two in direction, and time. Monte Carlo method is the widely accepted state-of-the-art stochastic method. However, the statistical nature of the method requires tracking a large number of photons, which is computationally expensive and not feasible for for image reconstruction. Under the assumption that the radiance in highly scattering medium is nearly isotropic after sufficient scattering, RTE can be approximated by the diffusion equation through a truncated spherical harmonics expansion (P1 approximation)[24, 9].

Diffusion equation in time domain can be written as:

$$\frac{\partial\Phi(\vec{r},t)}{c\partial t} - \nabla\cdot[D\nabla\Phi(\vec{r},t)] + \mu_a\Phi(\vec{r},t) = S(\vec{r},t), \quad (1.2)$$

where Φ is the fluence rate(or intensity), defined as the number of photons passing through the surface of a unit sphere per unit time regardless of the flow direction, S is an isotropic source of photons, and $D = [3(\mu_a + \mu_s')]^{-1}$ is the diffusion coefficient in units of millimeters. Here $\mu_s' = (1-g)\mu_s$ is the reduced scattering coefficient, where g is scattering anisotropy, which is average of cosine of scattering polar angel by single scattering. By Fourier transform, we can obtain the diffusion equation in frequency domain:

$$\left(\frac{i\omega}{c} + \mu_a\right)\Phi(\vec{r},\omega) - \nabla\cdot[D\nabla\Phi(\vec{r},\omega)] = S(\vec{r},\omega), \tag{1.3}$$

where ω is the angular modulation frequency in radians. A zero-frequency special case of frequency domain mode is the continuous wave (CW) mode:

$$\mu_a\Phi(\vec{r}) - \nabla\cdot[D\nabla\Phi(\vec{r})] = S(\vec{r}), \tag{1.4}$$

This dissertation focuses on CW mode due to its simplicity. Boundary conditions are required to solve the diffusion equation in the imaging domain. There are two types of boundary conditions that exist according the differences between the refractive index of scattering imaging medium and non-scattering ambient medium. When refractive index of the two medium are same, refractive-index-matched boundary condition can applied. From mathematical standpoint, these type of boundary conditions belongs to the Cauchy boundary conditions. However, air-tissue interface is dominant in biomedical imaging, which requires refractive-index-mismatched boundary condition, which also know as Robin type (Type III) boundary condition. In the time domain:

$$\Phi(\vec{r},t) - 2C_R D\nabla\Phi(\vec{r},t)\cdot\hat{n} = 0, \tag{1.5}$$

where $\hat{n}$ is the unit normal outward vector. The coefficient C_R can be derived from the Fresnels law:

$$C_R = \frac{1+R_{eff}}{1-R_{eff}} \tag{1.6}$$

where R_{eff} is the effective reflection coefficient which represents the percentage of the outgoing radiance toward the ambient medium that is converted to incoming radiance toward the scattering medium. Frequency domain and continuous wave

domain boundary conditions can be derived by Fourier transform and taking zero-frequency, respectively.

1.1.3 Diffuse optical tomography

Diffuse optical tomography (DOT), also known as near-infrared (NIR) tomography, refers to the optical imaging of biological tissue in the diffusive regime[14]. Since NIR light can penetrate several centimeters into biological tissue, DOT can image the human breast and infant brain without any ionizing risk. Due to the ill-posedness of inverse problem in DOT image reconstruction, recovering imaging information with good spatial resolution is challenging[25].

The basic principle of DOT is that NIR light source projects lights on the surface of specimen and then diffused photons are detected by the high sensitive photon detectors such as Charge couple device(CCD) camera at the surface of specimen. The spatial distribution of optical absorption and reduced scattering coefficients can be reconstructed using various algorithms (Figure 1.1). The spatial resolution of DOT is poor due to the high scattering.

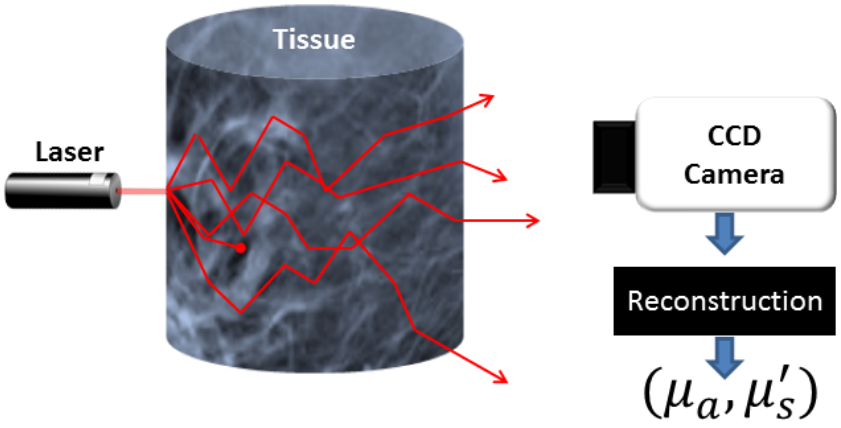

Figure 1.1: Schematic of DOT imaging

Forward problem of DOT

In the CW domain, NIR light propagation in turbid media is modeled by the diffusion equation [26], which is given as

$$-\nabla \cdot [\kappa(r)\nabla\Phi(r)] + \mu_a(r)\Phi(r) = Q_0(r) \tag{1.7}$$

where $\Phi(r)$ and $Q_0(r)$ are the photon density and isotropic light source at position r, respectively, and $\kappa(r)$ is the optical diffusion coefficient defined by

$$\kappa(r) = \frac{1}{3[\mu_a(r) + \mu_s'(r)]} \tag{1.8}$$

with μ_a and μ_s' representing the absorption coefficient and the reduced scattering coefficient, respectively. The air-tissue boundary is represented by the refractive index mismatch Robin (also known as Type-III) boundary condition, described as[27]

$$-2\alpha\hat{n} \cdot \kappa(r)\nabla\phi(r) = \Phi(r) \tag{1.9}$$

where $\hat{n}$ is the unit normal vector to boundary surface and α depends upon the relative refractive index mismatch between the air and tissue interface. It is determined by fitting the measurement data with the numerical calculations from the forward model. Eq.1.7 can be solved by a finite element method based a finite element mesh[28]

Inverse problem of DOT

The objective function (Ω), which minimizes the difference of modeled data (obtained from forward model) with the measurements,if we only reconstruct the absorption coefficients, can be written as [29]

$$\Omega = \min_{\mu_a}\{||y - F(\mu_a)||_2^2 + \lambda||L(\mu_a - \mu_{a0})||_2^2\} \tag{1.10}$$

where λ is the regularization parameter and L is a dimensionless penalty matrix which can be obtained from other structural imaging modality such as CT. When the structural information is not available, the L matrix can be replaced with an identity matrix I. The updating equation based on the Newton iterative method can be written as[30, 31, 32]

$$(J^T J + \lambda L^T L)\delta\mu_a = J^T(y - F(\mu_a)) \tag{1.11}$$

where J represents the Jacobian (sensitivity) matrix with a dimension $NM \times NN$, where NM represents the number of measurements and NN is the number of nodes. The update is represented by $\delta\mu_a = \mu_a - \mu_{a_0}$. In general, the initial value μ_{a_0} is obtained from data fitting procedure[33]. The L matrix is calculated before the reconstruction. This type of inclusion of prior information is often referred as soft-priors [34, 35].

1.1.4 Fluorescent molecular tomography (FMT)

FMT is an *in vivo* imaging modality to visualize physiological processes in small animals due to its high sensitivity to detect low concentration of target molecules. Since it shares same photon propagation model with DOT, it can also refers as fluorescence DOT(fDOT)[36] . Instead of detecting intrinsic contrasts like optical absorption and scattering coefficients, FMT detects the concentration of fluorescent dye injected prior to imaging, which targets specific molecular. The basic principle of FMT is that fluorescence dye is injected into a small animal, excited by the light in the NIR range from the surface of the small animal, and then the emitted fluorescent photons from fluorescent dye detected by the high sensitive photon detectors such as CCD camera at the surface of specimen (Figure 1.2). Similar to DOT, spatial resolution of FMT is poor due to the strong scattering. Imaging depth of FMT is depends on the wavelength of light (both excitation and emission). Green and blue lights, which have wavelength shorter than 500 nm, have an imaging depth of only few millimeter, whereas red and NIR light, which have a wavelength longer than 650 nm, have an imaging depth of up to 10 cm[37].

Fluorescence probes

FMT distinguish itself from DOT by detecting the concentration of target specific fluorescence probes administrated to the imaging object before imaging. Fluorescence probes are mainly divided into three groups: small synthetic, organic

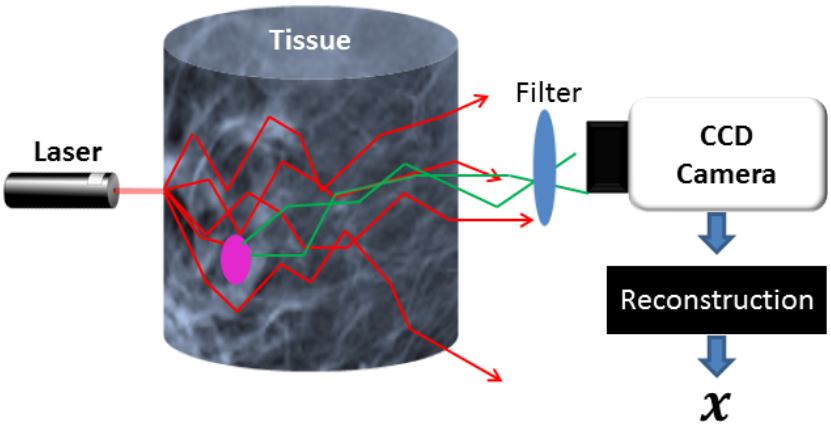

Figure 1.2: Schematic of FMT imaging

dyes; genetically encoded fluorescent proteins; and nanoparticles[37]. Fluorescence dye molecules and fluorescent proteins have the structure, which can determine the absorption and excitation spectrum. Quantum dots have a broad excitation but a narrow emission spectrum. Quantum dot will emit light of specific frequencies, which can be precisely designed by changing the dots's size, shape and material. Phosphor nanoparticles are another type nanoparitcles, which have attracting wide attention recently due to its lower toxicity compared to quantum dots and emission wavelength is shorter than its excitation wavelength.

Indocyanine green (ICG) is one of the widely used cyanine dye in fluorescent imaging. It has a peak spectral absorption at about 800 nm and emits fluorescence between 750 nm and 950 nm[38]. Since there is a big overlap between the excitation and emission spectrum, filtering out the scattered light from the excitation beam is necessary. Although there are numerous fluorescence probes have superior effectiveness in cancer detection, only few of them are Food and Drug Administration (FDA) approved. Recently, ICG is approved by FDA and was adopted for clinical use[39].

Forward problem of FMT

For FMT in the CW domain, the light propagation model in 3D is described by a set of coupled differential equations which are given below[40, 41]:

$$\begin{cases} -\nabla \cdot [D_{ex}(\boldsymbol{r})\nabla\Phi_{ex}(\boldsymbol{r})] + \mu_{\alpha,ex}\Phi_{ex}(\boldsymbol{r}) &= \delta_s(\boldsymbol{r}-\boldsymbol{r}_s) \\ \boldsymbol{n}\cdot[D_{ex}(\boldsymbol{r})\nabla\Phi_{ex}(\boldsymbol{r})] + \alpha_{ex}\Phi_{ex}(\boldsymbol{r}) &= 0 \\ -\nabla \cdot [D_{em}(\boldsymbol{r})\nabla\Phi_{em}(\boldsymbol{r})] + \mu_{\alpha,em}\Phi_{em}(\boldsymbol{r}) &= \Phi_{ex}(\boldsymbol{r})\boldsymbol{x}(\boldsymbol{r}) \\ \boldsymbol{n}\cdot[D_{em}(\boldsymbol{r})\nabla\Phi_{em}(\boldsymbol{r})] + \alpha_{em}\Phi_{em}(\boldsymbol{r}) &= 0 \end{cases} \tag{1.12}$$

where ∇ denotes the gradient operator, $D(\boldsymbol{r}) = \{3[\mu_s'(\boldsymbol{r})+\mu_a(\boldsymbol{r})]\}^{-1}$ is the diffusion coefficient, $\mu_\alpha(\boldsymbol{r})$ is the absorption coefficient and $\mu_s'(\boldsymbol{r})$ is the reduced scattering coefficient. $\Phi(\boldsymbol{r})$ is the photon fluence at the location $\boldsymbol{r}$. $\delta_s(\boldsymbol{r}-\boldsymbol{r}_s)$ is Dirac delta function defining point sources,and $\boldsymbol{r}_s$ is the location of the excitation point source. $\boldsymbol{x}$ is the product of the unknown fluorescent dye concentration and the quantum yield at each node to be reconstructed[42], $\boldsymbol{n}$ is the outward unit normal vector of the boundary, and α is the Robin boundary coefficient. In Eq. (4.1), subscripts ex and em mean corresponding terms at the excitation and emission wavelengths, respectively. Eq. (4.1) can be solved by the finite element method (FEM) based on a finite element mesh and is linearized to the following equation:

$$K_{ex}\Phi_{ex} = \delta_s(\boldsymbol{r}-\boldsymbol{r}_s), \quad K_{em}\Phi_{em} = \Phi_{ex}\boldsymbol{x} \tag{1.13}$$

where K_{ex} and K_{em} are the stiffness matrices at the excitation and emission wavelengths, respectively. With the conjugate gradient approach[43], the above equations can be described as[40]:

$$\boldsymbol{A}\boldsymbol{x} = \boldsymbol{b} \tag{1.14}$$

where $\boldsymbol{A} \in \mathbf{R}^{N_m \times N_n}$ is the system matrix, $\boldsymbol{x} \in \mathbf{R}^{N_n \times 1}$ is the unknown fluorephore distribution or the FMT image to be reconstructed, $\boldsymbol{b} \in \mathbf{R}^{N_m \times 1}$ is the measurement vector, N_n is the finite element node number, and N_m is the number of measurement.

Inverse problem of FMT

The inverse problem of FMT is to find distribution of the fluorephore within the imaging domain based on linear equation (1.14). Conjugate gradient (CG), preconditioned conjugate gradient (PCG), and algebraic reconstruction technique (ART) are the most popular methods applied to solve this of type problem. However, due to the ill-posed and ill-conditioned nature of the inverse problem of FMT,

regularization methods are desired. The objective function of the FMT with regularization will be:

$$\boldsymbol{x} = \arg\min_{\boldsymbol{x},\boldsymbol{x}\geq\boldsymbol{0}} \Phi(\boldsymbol{x}) =: ||A\boldsymbol{x} - \boldsymbol{b}||_2^2 + \lambda||\boldsymbol{x}||_p^p \tag{1.15}$$

where λ is regularization parameter is the regularization term and $0 < p \leq 1$. When $p = 2$ the regularization term becomes well-known Tikhonov regularization. There are variety of optimization methods to solve the above equation, however, Majorization-minimization (MM) algorithms stands out by its speed for large matrix. Here I follow Zhu and Li[44] to majorize the least squares fitting term:

$$\begin{aligned} ||\boldsymbol{b} - \boldsymbol{A}\boldsymbol{x}||_2^2 &= \sum_{i=1}^{m}(b_i - (Ax)_i)^2 \\ &\leq \sum_{i=1}^{m}\sum_{j=1}^{n}\beta_{ij}\left[b_i - (\boldsymbol{A}\boldsymbol{X}^k)_i - \frac{a_{ii}}{b_{ij}}(x_j - x_j^k)\right]^2 \\ &= \sum_{j=1}^{n}\left[\frac{(x_j - x_j^k)^2}{2}\sum_{i=1}^{m}\frac{a_{ij}^2}{\beta_{ij}} - x_j\sum_{i=1}^{m}a_{ij}(b_i - \boldsymbol{A}\boldsymbol{x}^k)_i) + g_j(x_j^k)\right] \end{aligned} \tag{1.16}$$

where $g_j(x_j^k)$ denotes a function of x_j^k only and non-negative parameters β_{ij} satisfies $\sum_{j=1}^{n}\beta_{ij} = 1$. Following the [45], we set $\beta_{ij} = a_{ij}/\sum_j a_{ij}$. Using the first order condition we have the update equation:

$$(x_j - x_j^k)\sum_{i=1}^{m}\frac{a_{ij}^2}{\beta_{ij}} - \sum_{i=1}^{m}a_{ij}(b_j(\boldsymbol{A}\boldsymbol{x}^k)_i) = 0 \tag{1.17}$$

Then we obtain the non-negative ordinary least squares(ols) solution in vector form:

$$\mathbf{x}_{osl}^{k+1} = \left(\mathbf{x}^k + \frac{1}{\kappa}A^t(b - Ax^k)\right)_+ \tag{1.18}$$

where $\kappa_j = \sum_{i=1}^{m}\frac{a_{ij}^2}{\beta_{ij}}$ and $u_+ = max(0, u)$.

1.2 Multimodality imaging

1.2.1 Introduction of multimodality imaging

Biomedical imaging, in general, can be divided into two groups: anatomical imaging and functional imaging. Anatomical imaging modalities such as

CT, MRI, and ultrasound imaging provide morphological information at high-resolution; however, these modalities provide little insight into physiological and metabolic changes. On the other hand, functional imaging modalities such a positron emission tomography (PET), single photon emission computed tomography (SPECT), and optical tomography can provide functional and/or molecular information with relatively low spatial resolutions. Since there is no single imaging modality which can have both high resolution anatomical structures and high sensitive functional information together, combining two or more imaging modalities is an obvious approach.

Over the last two decades, there has been increasing interest in combining the anatomical imaging modalities with functional imaging modalities to integrate the strengths of both, and at some point, eliminate weaknesses of an individual modality. The idea to combine two system is usually referred to as hybrid or dual-modality, which was first introduced by Hasegawa *et al.* at the University of California San Francisco, who combined a clinical CT scanner with SPECT camera as the first clinical SPECT/CT device in early 1990s[46]. Following the SPECT/CT, PET/CT scanners were also introduced at the end of 1990s[47], this opened new field research in universities and companies around the world[48]. Following the success story of SPECT/CT and PET/CT, currently, integration of MRI with PET or SPECT is one of the most active areas of multimodality imaging. Besides combining anatomic imaging modality with functional imaging modality, combining two anatomical imaging modality (hybrid X-ray/MR systems)[49] or two functional imaging modalities (Optical/PET and Optical/SPECT) are also investigated [50, 51].

Optical tomography, as a type of functional imaging modality with a relatively low spatial resolution, has also attracted significant attention to combined with high-resolution anatomical imaging modalities.

1.2.2 Anatomical guidance in DOT

Inclusion of a priori information into DOT can be implemented by minimizing the the following objective function

$$\Omega = \min_{\mu_a}\{||y - F(\mu_a)||_2^2 + \lambda||L(\mu_a - (\mu_{a0})||_2^2\} \tag{1.19}$$

Here λ is same as in LevenbergMarquardt method and L is a dimensionless penalty matrix which can be obtained from other structural imaging modalities such as CT. The L matrix is calculated before the reconstruction procedure and it is used through out the process to penalize the solution without change. This type of inclusion of priori information is often referred as soft-priors [35, 52].

Two types of L matrix are widely used in literature, Laplacian-type that is derived from the finite difference approximation to the Laplace equation and Helmholts-type which is derived from the finite difference approximation to the Helmholtz equation. In Laplacian-type, the L matrix is a matrix that relates each nodal property of the numerical model to all other nodes. Therefore given a node i within the mesh, its relationship to another node j having Laplacian structure within the same mesh can be given as [34, 35] ,

$$L_{ij} = \begin{cases} 0 & \text{if } i \text{ and } j \text{ are not in the same region} \\ -1/N & \text{if } i \text{ and } j \text{ are in the same region} \\ 1 & \text{if } i = j \end{cases} \tag{1.20}$$

where N is number of finite element nodes comprising a given region. In this case, $L^T L$ approximates a second-order Laplacian smoothing operator within each region, and works to average the update within a same region, while allowing discontinuity between different regions.

Helmholtz-type L-matrix is given as [53]

$$L_{ij} = \begin{cases} 0 & \text{if } i \text{ and } j \text{ are not in the same region} \\ \frac{-1}{N+(\kappa h)^2} & \text{if } i \text{ and } j \text{ are in the same region} \\ 1 & \text{if } i = j \end{cases} \tag{1.21}$$

where N is same as in Laplacian-type. Variable h is chosen to be the distance between the finite element nodes. $\kappa = 1/l$ is the wave number, generally chosen to be the inverse of the diameter (l) of the region in the imaging domain. In this case, $L^T L$ approximates a second-order Helmholtz smoothing operator. It is shown

that for small values of κ, which corresponds to a large l recover the same optical property distribution as Laplacian-type.

1.2.3 Anatomical guidance in FMT

Similar to DOT, the inverse problem of FMT is also ill-posed and ill-conditioned due to strong optical scattering in deep tissues. Structural priors are proven to be highly effective to improve the spatial resolution of reconstructed images[54, 55]. When structured priors are present, the objective function of the FMT with Laplacian regularization will be[55]:

$$\boldsymbol{x} = \arg\min_{\boldsymbol{x},\boldsymbol{x}\geq\boldsymbol{0}} \Phi(\boldsymbol{x}) =: ||A\boldsymbol{x} - \boldsymbol{b}||_2^2 + \lambda||\boldsymbol{L}\boldsymbol{x}||_2^2 \tag{1.22}$$

here regularization matrix L is same as in DOT.

Besides structural priors, there are functional priors, that improve accuracy of the forward modeling by using accurate optical properties for each region segmented from other imaging modality. Relatively accurate optical properties can be assigned to each region either by literature search or DOT reconstruction. The latter is also refereed to as DOT guided FMT, which achieved improved distribution of fluorophore concentration in phantom study[56]. The improvement of FMT image quality by applying both structural and functional prior information was demonstrated by scholars[57, 58]

1.3 Thesis Outline

In this thesis, I describe the theory and the anatomical image-guided DOT/FMT techniques used for breast cancer imaging and small animal imaging, respectively. I will also present my contribution to this filed, kernel based image reconstruction algorithm.

In chapter 2, I will present feasibility study of CT-guided DOT system for breast cancer imaging. In this study, to validate its feasibility, we have built a prototype DOT imaging system which consists of a laser at the wavelength of 650 nm and an electron multiplying charge coupled device (EMCCD) camera. We

have validated the CT guided DOT reconstruction algorithms with numerical simulations and phantom experiments, in which different imaging setup parameters, such as projection number of measurements and width of measurement patch, have been investigated. Our results indicate that an air-cooling EMCCD camera is good enough for the transmission mode DOT imaging. We have also found that measurements at six angular projections are sufficient for DOT to reconstruct the optical targets with 2 and 4 times absorption contrast when the CT guidance is applied. Finally, we have described our future research plan on integration of a multispectral DOT imaging system into a breast CT scanner. The key components of the multispectral DOT imaging system have been described and discussed.

In chapter 3, a kernel method is introduced to include anatomical guidance into the DOT image reconstruction. In this kernel method, the optical absorption coefficient at each finite element node is represented as a function of a set of features obtained from anatomical images such as computed tomography (CT) images. Compared with Laplacian approaches that include structural priors, the proposed method does not require image segmentation. The proposed kernel method is validated with numerical simulations of 3D DOT reconstruction using synthetic CT data. 5% Gaussian noise was added to both the numerical DOT measurements and the simulated CT image. The proposed method was also validated by an agar phantom experiment with the anatomical guidance from a cone beam CT scan. The effects of voxel size and number of nearest neighbors in the kernel method on the reconstructed DOT images were studied. The results indicate that the spatial resolution and the accuracy of the reconstructed DOT images have been improved substantially after applying the anatomical guidance with the proposed kernel method. Furthermore, we demonstrated that the kernel method was able to utilize clinical breast CT images as anatomical guidance without segmentation. In addition, we found that the proposed kernel method was robust to the false positive guidance in the anatomical image.

In chapter 4, the kernel method is introduced to include anatomical information into the FMT reconstruction is presented. The proposed method introduces the anatomical guidance into the projection model of FMT. The primary advantage

of the proposed method is that it does not require segmentation of targets in the anatomical images. Numerical simulations and phantom experiments have been performed to demonstrate the proposed approach's feasibility. Numerical simulation results indicate that the proposed kernel method can separate two FMT targets with an edge-to-edge distance of 1 mm and is robust to false positive guidance. For the phantom experiments with two FMT targets, the kernel method has reconstructed both targets successfully, which further validates the proposed kernel method. We have compared the proposed kernel method with the soft prior method thoroughly and found that the kernel method without target segmentation is able to achieve similar anatomical guided results as the soft prior method.

Chapter 5 summarizes the dissertation and also discuss the future work.

Chapter 2

Diffuse optical tomography for breast cancer imaging guided by computed tomography: a feasibility study

2.1 Introduction

In the United States of America, breast cancer ranks second in all cancers in terms of cancer mortality in female population[59]. Breast cancer screening, especially if being capable of early detection, is one of the efficient approaches to reduce the mortality rate caused by breast cancer [60]. Mammography has been used widely for breast cancer screening, but it is difficult to diagnose breast cancers for breasts with high mammographic density and/or micro-calcifications[61]. Ultrasound imaging has higher sensitivity than mammography in imaging dense breast but with low specificity in screening breast cancers[62, 63]. Magnetic resonance imaging (MRI) was reported to have results correlated better with pathology findings than mammography and obtained promising results when dynamic contrast agents are applied[64, 65, 66]. However, MRI is expensive and exogenous agents are needed for better contrast. In 1990s, DOT has emerged with promises

as an imaging tool for breast cancer screening and diagnosis because of its unique features such as non-ionizing radiation, low cost, and high intrinsic absorption contrast [67].

We use continuous wave (CW) measurement data due to its simplicity and low cost. CW measurements at multiple wavelengths in the near infrared (NIR) wavelength range were used to reconstruct different absorption chromophores in tissues[68, 69, 70, 71, 72]. Most DOT breast imaging systems used fibers to deliver lasers to breast surface and collected the diffused light on the breast surface, in which the measurement number was determined by the optode pairings [73, 74, 75, 76, 77, 78, 69, 79, 80]. To increase the number of measurement data, Culver *et al.* reported a charge coupled device (CCD) camera based DOT imaging system[81]. Turner *et al.* used a CCD camera to measure early photons in a DOT imaging system[82]. In this study, we used an EMCCD camera to measure light intensity on the breast surface in a transmission mode.

DOT is an ill-conditioned inverse problem and suffers low spatial resolution. To enhance the DOT reconstruction, anatomical priors were introduced[32, 83, 84, 85, 86, 87]. Fang *et al* reported a Tomosynthesis/3D-mammogram guided DOT imaging system [88, 89]. Brooksby *et al.* and Ntziachristos *et al.* reported MRI guided, fiber based DOT imaging systems [90, 91, 35]. Zhu and colleagues used ultrasound imaging to guide the DOT imaging[92, 76]. These studies have shown substantial improvements in quality and accuracy of DOT imaging with structural priors. However, these systems have limitations. Tomosynthesis is not true three-dimensional (3D) imaging modality thus its structural guidance is not sufficient. And the imaged breast is compressed during the Tomosynthesis/3D-mammogram scan which might cause discomfort to patients. For MRI guidance, MRI is very expensive some patients with some metal implants cannot be imaged by MRI. For ultrasound imaging guidance, approximations are requite for coregistering the two-dimensional (2D) ultrasound images to the 3D optical measurements[92] . Our proposed CT guided DOT imaging system will not have these limitations.

In this paper, we report a novel CT guided DOT system for breast cancer imaging. The spatial resolution of the DOT system is improved with the anatom-

ical guidance obtained from CT imaging. There are several advantages of this proposed system. Firstly, although breast CT system uses X-ray photons, the radiation dose is less than or equivalent to that of a two-projection mammography, which is minimal[93, 94]. Secondly, because we use an EMCCD camera to acquire optical measurement data, our system is non-contact, does not need coupling fluid, and will not bring any pain or discomfort during the scanning. Lastly, with the use of an EMCCD camera we can have abundant measurement data for DOT reconstruction, although the camera may have limited sensitivity of measurements.

The rest of this article is organized as follows. In section 2.2, we introduce methods and materials. Then we report numerical simulation and phantom experiments. Finally, we end the paper with summary and future work.

2.2 Methods and materials

2.2.1 DOT prototype system

The DOT prototype system built in our lab consisted of an EMCCD camera (C9100-13,Hamamatsu) with a lens (CM 120 12101,Schneider Xenon 25mm f \0.95), a diode laser at 650 nm with a collimator (BWF-OEM-650-200-100-0.22, B&W Tek, Inc), a linear stage (XN10-0060-E01-71 C044289, Velmex, Bloomfield,NY) and a rotary stage (B4872TS-ZRS C042679, Velmex, Bloomfield,NY). As shown in Fig. 2.1, the imaged phantom was placed on the rotation stage. The EMCCED camera was mounted on its right side with a distance of 25 cm so that the field of view (FOV) of the camera covered the whole phantom. The laser collimator was mounted on a linear stage and was 1 cm away from the phantom surface on the left side. A laser beam was collimated to have a diameter less than 2 mm on the phantom surface. During the experiments, the EMCCD camera stayed stationary while the rotary stage rotated the phantom with an angular step of 60 degrees. For each rotation angle, the linear stage moved the laser beam 6 steps in vertical direction with a step size of 5 mm. This system generated 36 illumination points on the phantom of interest. For each illumination position, three images were taken by the EMCCD camera and averaged to reduce measurement noises.

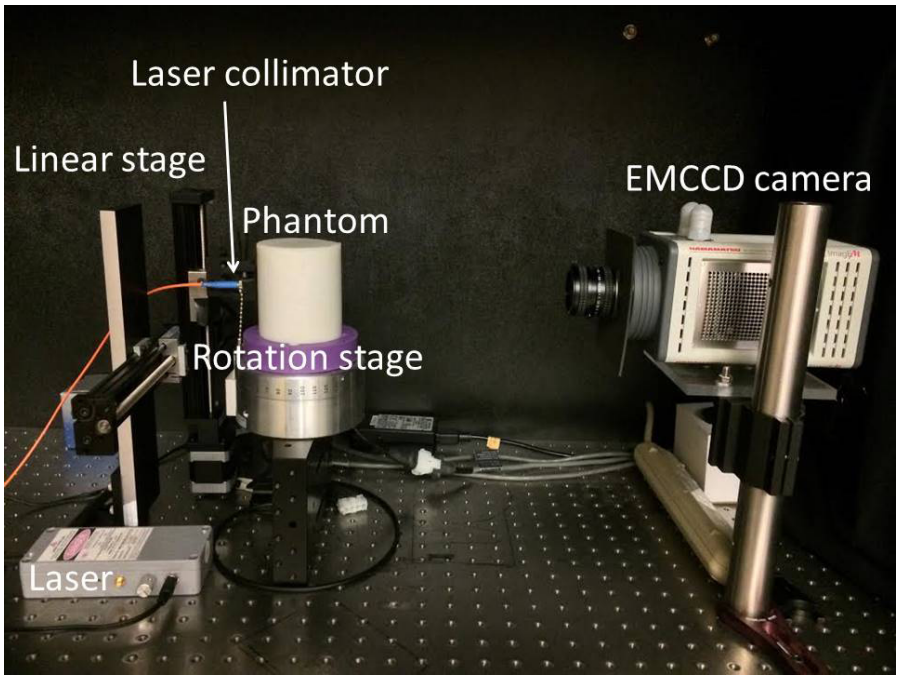

Figure 2.1: Photo of the DOT prototype system

2.2.2 Forward model and reconstruction algorithm

The propagation of light in turbid media such as biological tissues can be modeled precisely by the radiative transfer equation (RTE)[9, 23, 25, 95]. Because it is difficult to solve the RTE, the diffusion equation is widely accepted as an approximation to the RTE in DOT imaging. The finite element method (FEM) is used to solve the diffusion equation [95, 3]. And due to the ill-posed nature of the inverse problem in DOT, regularization methods are used to stabilize the DOT reconstruction [96, 97].

Forward modeling

In the CW domain, NIR light propagation in turbid media is modeled by the diffusion equation [26], which is given as

$$-\nabla \cdot [\kappa(r)\nabla\Phi(r)] + \mu_a(r)\Phi(r) = Q_0(r) \tag{2.1}$$

where $\Phi(r)$ and $Q_0(r)$ are the photon density and isotropic light source at position r, respectively, and $\kappa(r)$ is the optical diffusion coefficient defined by

$$\kappa(r) = \frac{1}{3[\mu_a(r) + \mu_s'(r)]} \tag{2.2}$$

with μ_a and μ_s' representing the absorption coefficient and the reduced scattering coefficient, respectively. The air-tissue boundary is represented by the refractive index mismatch Robin (also known as Type-III) boundary condition, described as[27]

$$-2\alpha\hat{n} \cdot \kappa(r)\nabla\phi(r) = \Phi(r) \tag{2.3}$$

where $\hat{n}$ is the unit normal vector to boundary surface and α depends upon the relative refractive index mismatch between the air and tissue interface. It is determined by fitting the measurement data with the numerical calculations from the forward model.

Reconstruction algorithm

The objective function (Ω), which minimizes the difference of modeled data (obtained from forward model) with the measurements,if we only reconstruct the absorption coefficients, can be written as [29]

$$\Omega = \min_{\mu_a}\{||y - F(\mu_a)||_2^2 + \lambda||L(\mu_a - \mu_{a0})||_2^2\} \tag{2.4}$$

where λ is the regularization parameter and L is a dimensionless penalty matrix which can be obtained from other structural imaging modality such as CT. When the structural information is not available, the L matrix can be replaced with an identity matrix I. The updating equation based on the Newton iterative method can be written as[30, 31, 32]

$$(J^T J + \lambda L^T L)\delta\mu_a = J^T(y - F(\mu_a)) \tag{2.5}$$

where J represents the Jacobian (sensitivity) matrix with a dimension $M \times N$, where M represents the number of measurements, and N is the number of nodes. The update is represented by $\delta\mu_a = \mu_a - \mu_{a_0}$. In general, the initial value μ_{a_0}

is obtained from data fitting procedure[33]. The L matrix is calculated before the reconstruction. This type of inclusion of prior information is often referred as soft-priors [34, 35].

2.2.3 Mapping of measurement data

Correctly mapping of photon intensity information from an EMCCD camera image to detector nodes on a finite element mesh is critical for the DOT image reconstruction. To improve mapping accuracy, we made a reference cylinder which had 24×9 checkerboard on its surface. Each checkerboard is a square with a width of 10.21 mm that was equal to 1/24 of the cylinder circumference. The 3D physical coordinates of corners for each square were known on the cylinder surface. To map correctly, we took one image of the reference cylinder with our prototype system. There were 6×4 checks in the side field of view. We found pixel coordinates of all 35 corners for square on the EMCCD camera image manually. Then, using those pixel coordinates and their corresponding physical coordinates, we generated linear mapping matrix for mapping finite element nodes coordinate to the corresponding EMCCD camera image pixel. Fig. 2.2 shows mapping results using the linear matrix we generated. Ideally, if the mapping was perfect, each red dot in Fig. 2.2 should be on the crossing points on the checkerboard exactly. Most of the nodes inside the FOV were matched very well, while the nodes far away from the center were not mapped well with the corners of squares because we used a simple linear mapping method and the surface of the cylinder was not flat. The linear mapping matrix is good enough to be used in the phantom experiments because the measurement nodes were not far away from the center.

2.2.4 Measurement setup

In our DOT prototype system, the EMCCD camera was used as a detector, which could only measure half of the phantom surface in a transmission measurement mode. For each angular projection, the linear stage moved the laser source 6 steps in vertical direction with a step size of 5 mm. This system generated 6

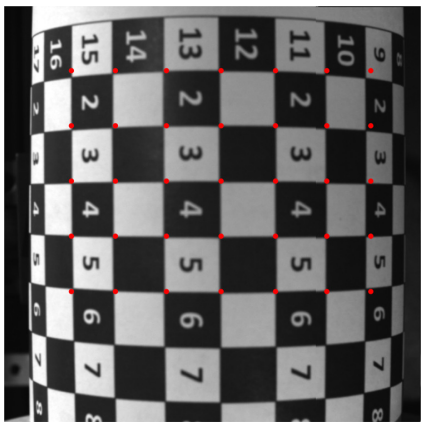

Figure 2.2: Mapped reference nodes in an image taken by the EMCCD camera

source illumination points on the phantom of interest for each projection. For each source position, we used all finite element nodes inside a 6 cm wide and 4 cm high measurement patch on the other side of the phantom (Fig. 2.3b). The numerical simulations reported later have helped us to select the width of the measurement patch.

2.2.5 Phantom recipe and geometry

A cylindrical phantom with a diameter of 78 mm and a height of 60 mm was made with Agar, Titanium dioxide (TiO_2), Indian ink and water.A jelly like soft base phantom made with a through hole at the target location, which is 15 mm away from the center line of the cylinder. Then, a cylindrical target with a diameter of 10 mm and a height of 10 mm was inserted into the hole on the background phantom. The top 20 mm and the bottom 30 mm of the hole filled with same material as base phantom (Fig. 2.3a). The phantom was fabricated to have $\mu_a = 0.005$ mm^{-1} and $\mu_s' = 1.0$ mm^{-1} at the wavelength of 650 nm. The target had an absorption coefficient of 0.02 mm^{-1} and a reduced scattering coefficient of 1.0 mm^{-1} at the wavelength of 650 nm.

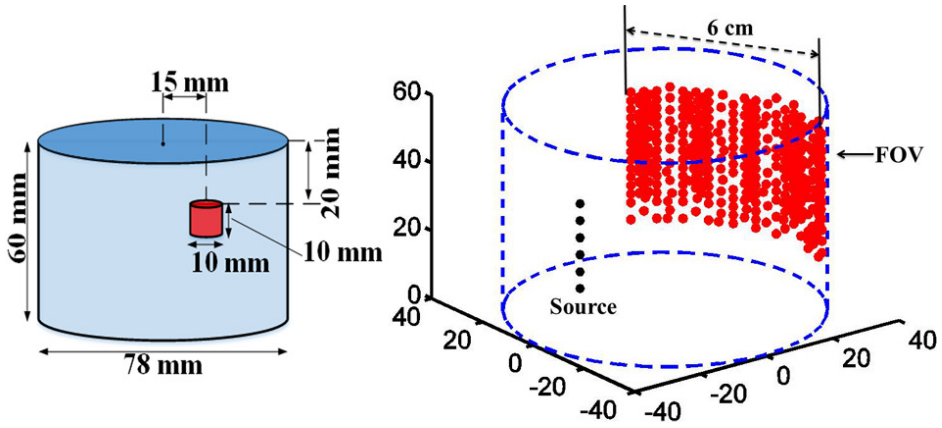

(a) (b)

Figure 2.3: (a) Phantom geometry. (b) Source nodes (black) and detector nodes (red) in a 6 cm wide measurement patch for an angular projection.

2.2.6 Measurement data calibration with a homogeneous phantom

We used a cylindrical phantom whose surface was not flat. Different measurement points on the cylindrical surface had different orientations and distances to the EMCCD camera, which resulted in different photon collection coefficients at different pixels. We calibrated our measurements with the same approach described in Ref. [98]. At first, we made a homogeneous phantom with the same optical properties and the same geometrical dimensions as the heterogeneous phantom of interest. Secondly, we obtained a set of measurement data D_{ij} at same setup for the heterogeneous phantom. Thirdly, optical properties such as absorption coefficient μ_a, reduced scattering coefficient μ_s' and boundary condition parameter α, were determined by data fitting[33]. Then, we calculated the calibration coefficients $f_{ij} = D_{ij}^*/D_{ij}$, where D_{ij}^* are the measurements from forward modeling with optical properties obtained in the 3rd step. Finally, we multiplied ratio factor f_{ij} by the measurement data M_{ij} from the heterogeneous phantom to obtain the final calibrated measurements for DOT reconstruction.

2.3 Results

2.3.1 Results of numerical simulations

The measurement projection number and the measurement data volume are important factors for data acquisition time, reconstruction time and DOT image quality. We conducted a series of numerical simulations to figure out the optimal number of projections and the width of the EMCCD camera measurement patch. In the numerical simulations, we used a cylindrical phantom with a diameter of 78 mm and a height of 60 mm. A cylindrical target (diameter of 10 mm and height of 20 mm) was placed at 15 mm away from the center line of the phantom. Here we simulated four different data acquisition types: (a) four projections with 3 cm wide measurement patch; (b) four projections with 6 cm wide measurement patch; (c) six projections with 3 cm wide measurement patch; (d) six projections with 6 cm measurement patch. In all cases, the number of source position in each angular projection was 6, and placed 5 mm apart from each other vertically. The height of detection patch was 4 cm for all cases. We set the reduced scattering coefficient to 1 mm^{-1} for both target and background uniformly. The absorption coefficient was 0.007 mm^{-1} for background and 0.028 mm^{-1} for target as shown in Table. 3.1.

Table 2.1: Optical properties and geometry dimensions of the phantom for simulations.

	Diameter	**Height**	μ_a	μ_s'
Background	78.0 mm	60.0 mm	0.007 mm^{-1}	1.0 mm^{-1}
Target	10.0 mm	20.0 mm	0.028 mm^{-1}	1.0 mm^{-1}

First, we compared reconstruction results among the above four cases with 5% Gaussian noise added. From Fig. 2.4, we see that we cannot reconstruct the target with measurements from four projections. Although we can clearly see target location in the reconstructed image using measurements from six projections with 6 cm wide measurement patch, the value of the reconstructed absorption coefficient is much less than the ground truth. Then we used a virtual CT image

as structural prior in DOT reconstruction. From Fig. 2.5, we see that, we were able to reconstruct good results for all four cases. Finally, We tested this with 30% Gaussian noise added. From Fig. 2.6, we see that the target location is at the right position, but the reconstructed absorption coefficient is much less that ground truth value in case (a) of four projections with 3 cm wide measurement patch. There are some artifacts on the boundary for cases (b) and (c). The simulation for six projections with 6 cm wide measurement patch performs best in both target location and quantitative accuracy. From the profile plots in Fig. 2.7, we can also verify that the quality of the reconstructed absorption coefficient images from six projections with 6 cm wide measurement patch is the best when a virtual CT image was used as structural prior in the DOT reconstruction. From Fig. 2.7, we calculate the errors of the reconstructed absorption coefficient in the target to be 3.57% and 3.22% for 5% and 30% Gaussian noise cases, respectively, with the virtual CT guidance and measurements at 6 projections with 6 cm wide patch.

2.3.2 Phantom experiment

We evaluated our single wavelength, EMCCD camera based DOT imaging prototype system by preforming two set of an agar phantom experiments. The phantom recipe and geometry was described in method section. The first phantom experiment has 4:1 absorption contrast and the second has 2:1 absorption contrast. The optical properties and geometrical dimensions are given in Table. 2.2 For each illumination position, we used all finite element surface nodes in a 6 cm wide and 4 cm high patch on the other side of the phantom as detector nodes. The number of nodes inside the patch for each projection are slightly different, and the total number of measurements are 14520 for all projections. We compared reconstruction results among 4 different cases: (a) uncalibrated measurements data without structural guidance; (b) calibrated data without structural guidance; (c) uncalibrated data with structural guidance; and (d) calibrated data with structural guidance. For cases (b) and (d), we calibrated measurement with the method described in section 2.2.6. For cases (c) and (d), we used the physical location information of the target as the virtual structural prior because the CT scanner was not available

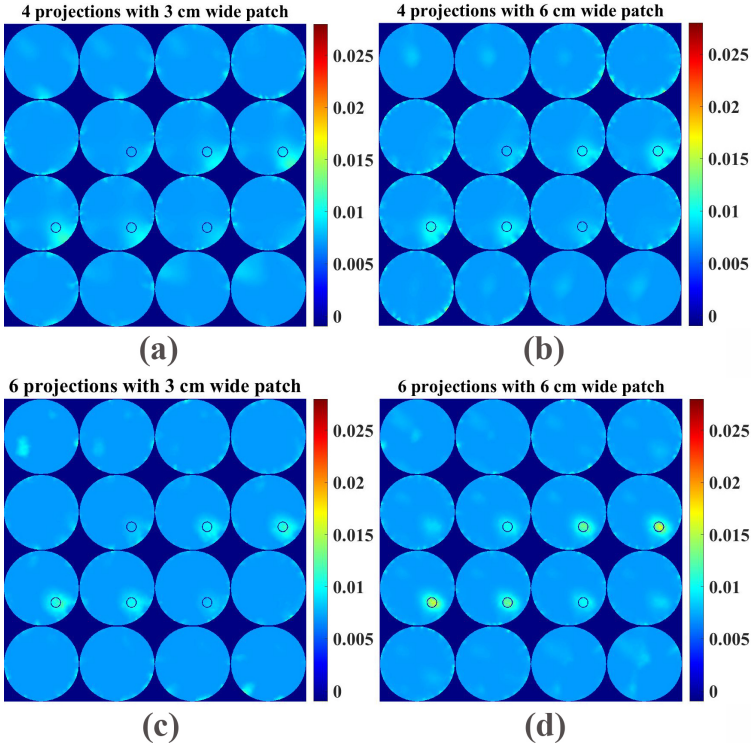

Figure 2.4: Transverse sections of the reconstructed absorption coefficient images from simulated measurements with 5% Gaussian noise added for cases (a) four projections with 3 cm wide measurement patch; (b) four projections with 6 cm wide measurement patch; (c) six projections with 3 cm wide measurement patch; and (d) six projections with 6 cm wide measurement patch.

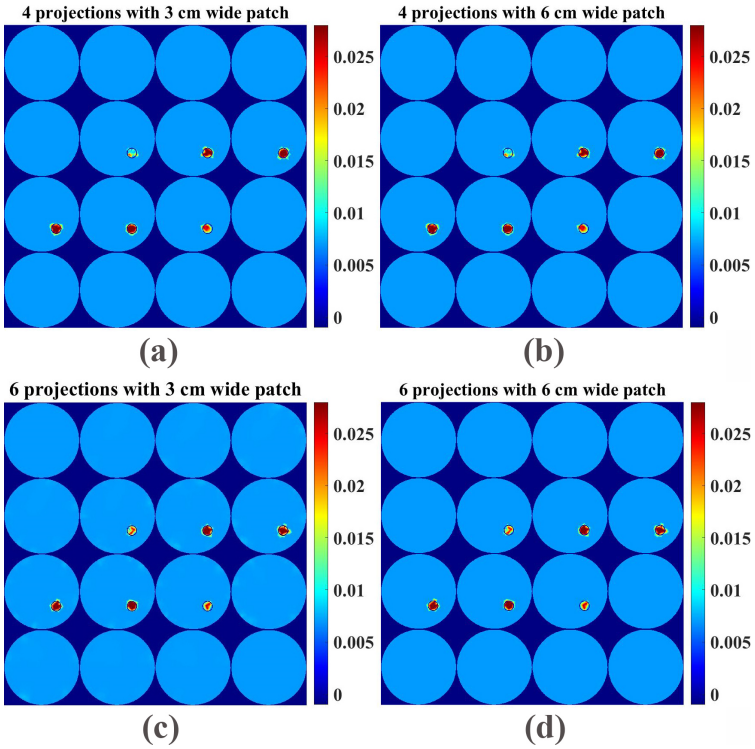

Figure 2.5: Transverse sections of the reconstructed absorption coefficient images with virtual CT guidance from simulated measurements with 5% Gaussian noise added for cases (a) four projections with 3 cm wide measurement patch; (b) four projections with 6 cm wide measurement patch; (c) six projections with 3 cm wide measurement patch; and (d) six projections with 6 cm wide measurement patch.

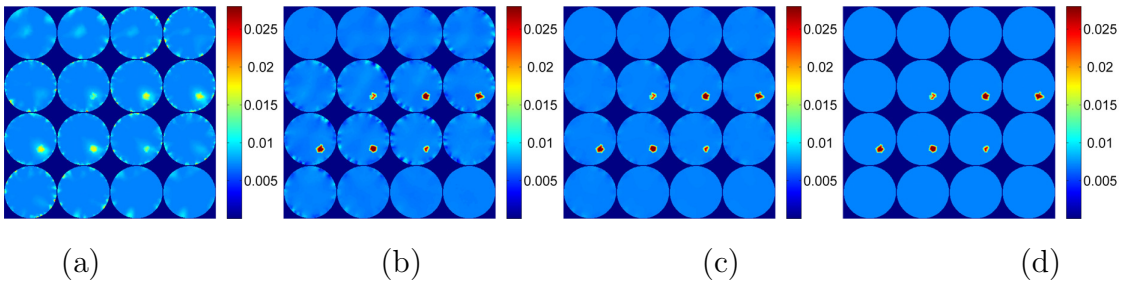

Figure 2.6: Transverse sections of the reconstructed absorption coefficient images with virtual CT guidance from simulated measurements with 30% Gaussian noise added for cases (a) four projections with 3 cm wide measurement patch; (b) four projections with 6 cm wide measurement patch; (c) six projections with 3 cm wide measurement patch; and (d) six projections with 6 cm wide measurement patch.

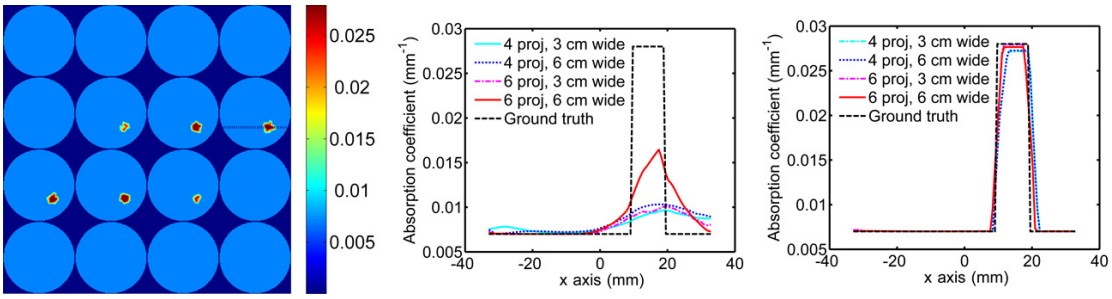

(a) (b) (c)

Figure 2.7: (a) Ground truth absorption coefficient image for simulation,the dotted black line indicates the profile position. Profiles of the reconstructed absorption coefficient images along the black doted lines for (b) simulated measurements with 5% Gaussian noise (Fig. 2.4) ; (c) simulated measurements with 5% Gaussian noise and with virtual CT guidance (Fig. 2.5); (d) simulated measurements with 30% Gaussian noise and with virtual CT guidance (Fig. 2.6).

during the experimental time.

Table 2.2: Optical properties and geometrical dimensions of the experimental phantoms.

	Diameter	**Height**	$\boldsymbol{\mu_a}$	$\boldsymbol{\mu_s'}$
Background	78.0 mm	60.0 mm	0.005 mm^{-1}	1.0 mm^{-1}
Target (4:1 $\boldsymbol{\mu_a}$ contrast)	10.0 mm	10.0 mm	0.02 mm^{-1}	1.0 mm^{-1}
Target (2:1 $\boldsymbol{\mu_a}$ contrast)	10.0 mm	10.0 mm	0.01 mm^{-1}	1.0 mm^{-1}

The reconstructed results of 4:1 absorption contrast phantom are plotted in Fig. 2.8, from which we can see that there are many artifacts at the boundary in the reconstructed absorption coefficient image using uncalibrated data without structural guidance (as shown in Fig. 2.8a). Calibration with the homogeneous phantom improves reconstruction results even without structural prior but there are still some artifacts at the boundary and the reconstructed absorption coefficient at targets is less than the true value (as shown in Fig. 2.8b). Reconstruction with

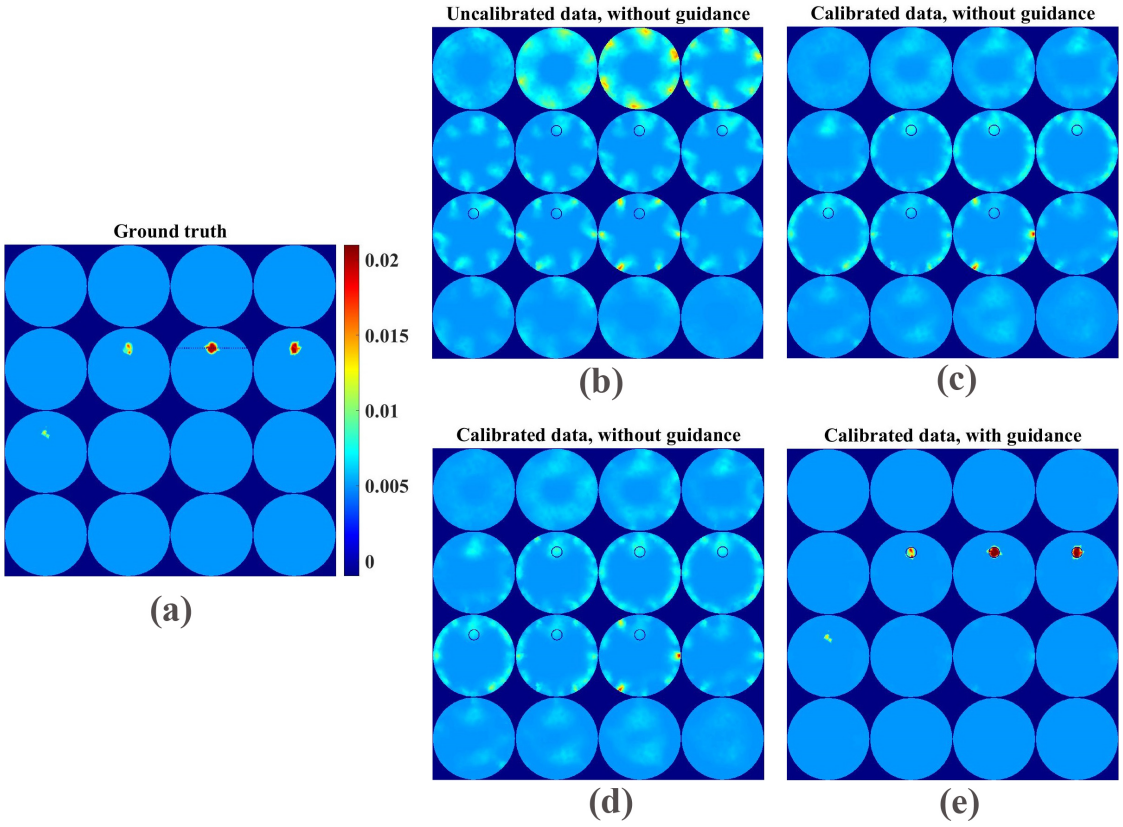

Figure 2.8: Transverse sections of the reconstructed absorption coefficient images with measurements at six projections, a target with 4:1 absorption (μ_a) contrast for cases (a) uncalibrated data without structural guidance; (b) calibrated data without structural guidance; (c) uncalibrated data with structural guidance; and (d) calibrated data with structural guidance.

structural guidance using uncalibrated measurement data outperformed the previous two cases with some artifacts at boundary (as shown in Fig. 2.8c). And the recovered absorption coefficient at the target is much less than the exact value (as shown in Fig. 2.8). Reconstruction with the structural prior using calibrated measurements performs best in both target location and the reconstructed absorption coefficients (as shown in Fig. 2.8d).

From the reconstructed results of 2:1 absorption contrast phantom (Fig. 2.9), we can also see that measurement calibration and virtual structural guidance improves the reconstruction results. Reconstructed image using uncalibrated data without structural guidance almost same as corresponding results from 4:1 ab-

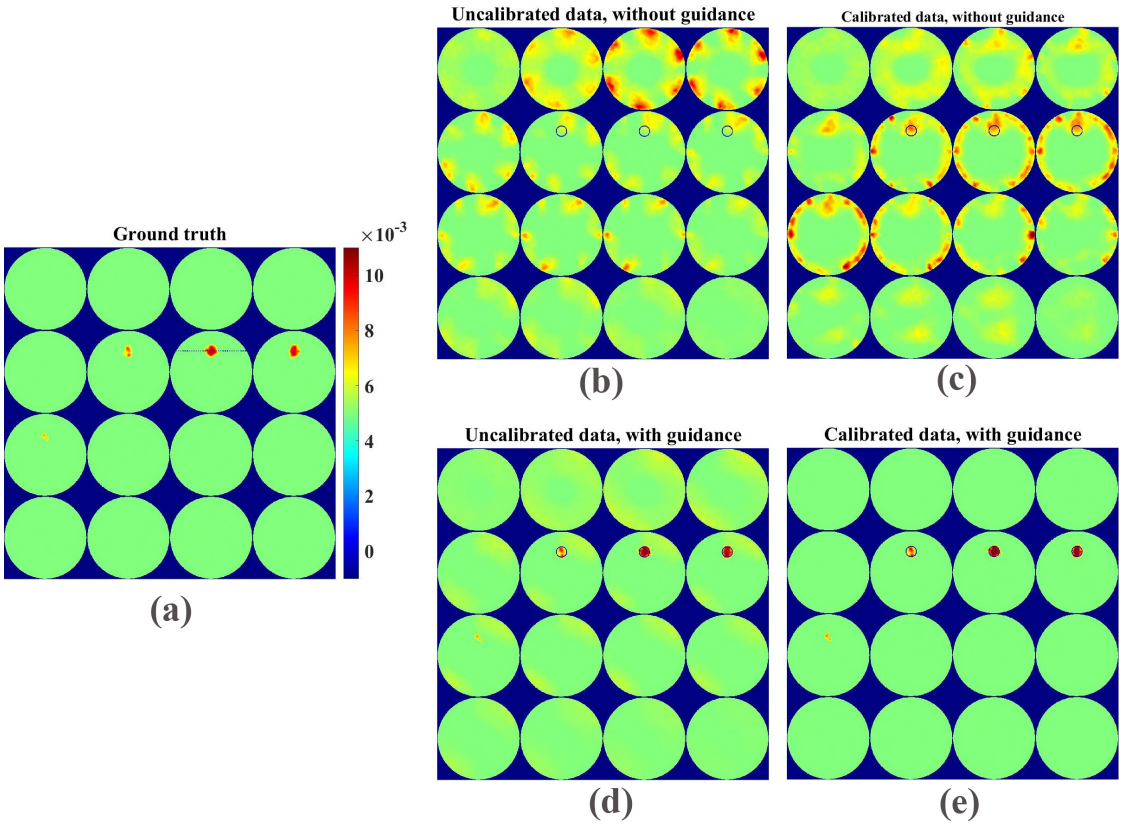

Figure 2.9: Transverse sections of the reconstructed absorption coefficient images with measurements at six projections, a target with 2:1 absorption (μ_a) contrast for cases (a) uncalibrated data without structural guidance; (b) calibrated data without structural guidance; (c) uncalibrated data with structural guidance; and (d) calibrated data with structural guidance.

sorption contrast. (as shown in Fig. 2.9a), which can not provide useful functional information. In cases (b) and (c), reconstructed image qualities improved to some extent, but there are still significant artifacts. Reconstruction with the structural prior using calibrated measurements gives us the best reconstructed optical properties in target region with accurate location (as shown in Fig. 2.9d).

To analyze the reconstructed images quantitatively, we plot the profiles along the position indicated by the black dotted line. From the profile plots in Fig. 2.10, we can also verify that the quality of the reconstructed images from calibrated data with a virtual CT image as structural prior in DOT reconstruction is reaches to ground truth image. For the 4 times absorption case, the mean squared errors

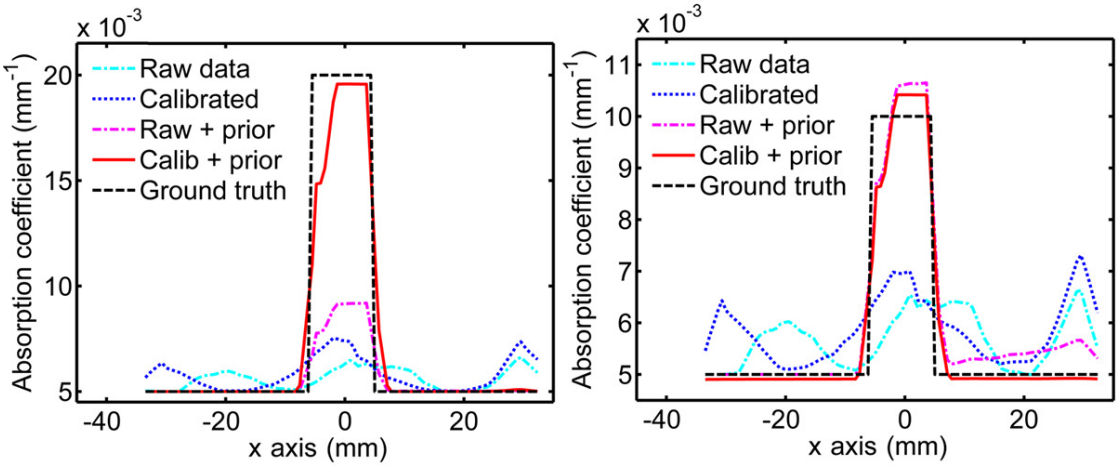

Figure 2.10: Ground truth absorption coefficient image for (a) 4:1 absorption contrast experiment and (b) 2:1 4:1 absorption contrast experiment. Profiles of the reconstructed absorption coefficient images along he black doted lines for (c) 4:1 absorption contrast experiment (Fig. 2.8) and (d)2:1 absorption contrast experiment (Fig. 2.9);

of the reconstructed absorption coefficient in the target for calibrated data with virtual CT guidance is 3.8%. The error is 1.4% for the 2 times absorption contrast case. The target size errors are 1 mm and 3 mm for 4 and 2 times absorption contrast cases, respectively.

2.4 Discussion and future work

We have built the prototype DOT imaging system that mimics the future CT guided DOT imaging system by using the same EMCCD camera and the same collimated laser beam. With both numerical simulations and phantom experiments, we have studied the effects of the projection number and the width of FOV on the reconstructed DOT images. Although we used the virtual CT guidance in the studies, the feasibility study in this paper lays a solid path for our future CT guided DOT imaging with the real system. The major purpose of the proposed CT guided DOT imaging system is to monitor the breast cancer response to the chemotherapy. Neoadjuvant chemotherapy is widely used in the treatment of locally ad-

vanced breast cancer. Monitoring the response to the chemotherapy can improve survival and reduce morbidity. Tumor responsive to the chemotherapy has vascular changes that can be monitored by DOT noninvasively. The total hemoglobin concentration reduction is a major sign for the responsive breast tumors.[99, 100, 101] Photon scattering in DOT makes it difficult to localize tumor size and position. CT can provide guidance in DOT reconstruction algorithms to minimize the effects of optical scattering for accurately monitoring of breast cancers response to the chemotherapy. The major challenge for the CT guided DOT imaging system is that CT does not have very good soft tissue contrast to differentiate tumor very well from its background. Patients with neoadjuvant chemotherapy usually have late stage breast cancers. The CT contrast agents could enhance the breast cancer imaging of CT. Furthermore, the soft prior guidance algorithm can correct the mismatched guidance to some extent (up to 7%) as reported in Ref. [84].

The homogeneous phantom based calibration method as described in section 2.7 works well for phantom experiments. This method can be applied to in vivo breast imaging by scanning a homogeneous phantom with the same geometry and similar optical properties of the imaged breast. We can obtain the imaged breast geometry from the CT images and then print a mold with a 3D printer. The optical properties can be estimated by the fitting algorithm as described in reference [98]. Another approach, one of our future research topics, is to use a ray tracing software (LightTools, Synopsys Inc.) to calculate the photon collection efficiency at different detector positions on the breast surface.

One possible limitation of the proposed CT guided DOT imaging system is the small dynamic range of the EMCCD camera. Another possible limitation is the reflected optical photons from the scanners to the EMCCD camera. One way to overcome this limitation is painting black all the components inside the system.

We have investigated the feasibility study of the CT guided DOT imaging with 2 times and 4 times absorption contrast targets for both numerical simulation and phantom experiments. Although these studies can prove the feasibility, we need to include the scattering effects in the future studies, especially when we will include four lasers at four different wavelengths in the future system.

In the future, we will build a multispectral EMCCD camera based DOT imaging system which consists of 4 diode CW lasers, an optical switch, a fiber holder, collimators, an EMCCD camera and a rotation stage. Four CW lasers at wavelengths of 650, 715, 880, and 915 nm will be connected to a 4-to-12 optical switch which passes one laser to one of 12 fibers and the laser beam will be collimated at the other end of the fiber with a collimator. Measurements at six projections with rotational increments of 60 degrees will be taken to cover the whole surface of the breast. Altogether, there will be 4 lasers with total 72 excitation positions for each of them. For each laser excitation position, pictures will be taken by the EMCCD camera as measurements in a transmission mode. The EMCCD camera based DOT imaging system will be integrated into a breast CT imaging system[93]. The breast CT imaging system has a powerful rotation gantry, on which optical fiber holder and EMCCD camera will be mounted. The schematic of the proposed CT guided DOT imaging system is plotted in Fig. 10. We have selected an optical switch from Dicon Fiberoptics. The switch time is about 0.5 seconds. The rotation time per 60 degrees is estimated to be 5 seconds. The exposure time per measurement picture is estimated to be 1 second per wavelength and position. So that the total measurement time for the DOT imaging is estimated about 8 minutes.

2.5 Conclusion

In this paper, we proposed a novel CT guided DOT system for breast cancer imaging, which uses an EMCCD camera as a detector without any coupling liquid. We evaluated our prototype system with a set of numerical simulations and phantom experiments. From numerical simulations, we confirmed that the measurement data from six projections with 6 cm wide measurement patch are enough to reconstruct good absorption image with high quantitative accuracy if CT guidance is applied. From phantom experiments, we see that our proposed CT guided DOT system is able to reconstruct 2 times absorption contrast image at very high spatial resolution and quantitative accuracy. In the future, we will combine our prototype DOT system with a dedicated breast CT system and evaluate

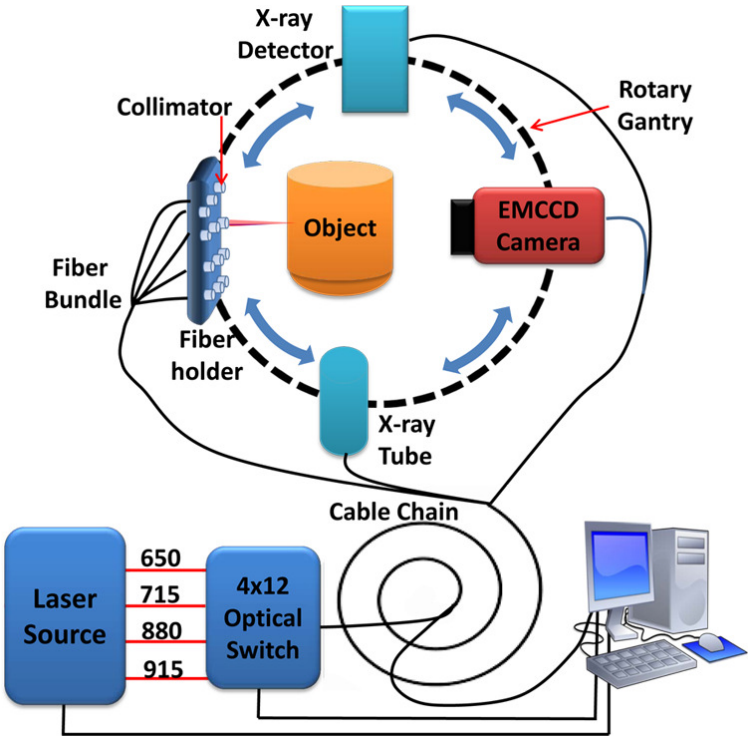

Figure 2.11: Schematic of CT guided DOT system.

the system performance with phantom experiments and patient data. Our preliminary measurements of the output laser power variation due to the rotation and the collimated laser beam size changes due to different laser project distances have further proved the feasibility of our proposed CT guided DOT imaging system.

Chapter 3

Kernel-based anatomically-aided diffuse optical tomography reconstruction

3.1 Introduction

Diffuse optical tomography (DOT) is a non-invasive, non-ionizing radiation biomedical imaging modality[102] that can recover the spatial distribution of tissue optical properties such as absorption and scattering coefficients[14, 74]. With measurements at multiple wavelengths, DOT has the capacity of estimating hemoglobin concentrations, oxygenation level, and water content of tissues[103, 104]. Its applications include, but are not limited to, brain imaging[105, 106, 107], breast cancer characterization[108, 109, 110, 8, 111], prostate cancer monitoring[112, 113, 114, 115], and joint tissue imaging[116, 117]. However, DOT suffer from low spatial resolution due to strong optical scattering in tissues. Furthermore, DOT image reconstruction is known to be a nonlinear, ill-posed, and ill-conditioned problem[25]. During the last two decades, many research groups and companies have made numerous efforts to improve the spatial resolution of DOT systems. A variety of algorithms have been proposed to improve the accuracy of the inverse problem of DOT[73, 118, 119, 120, 27, 121, 122, 123, 124, 125, 126, 127, 128]. However, DOT

system standalone is still inferior to the other functional imaging modalities such as functional magnetic resonance imaging (fMRI), single-photon emission computed tomography (SPECT), and positron emission tomography (PET).

To improve the spatial resolution of DOT imaging, anatomical image guided reconstruction methods were introduced. Pogue, Brooksby, and Zhao, *et al.* have, for the first time, introduced the structural guidance from the magnetic resonance imaging(MRI) into the near-infrared tomographic imaging[129, 34, 130]. Ntziachristos *et al.* have also reported simultaneous magnetic resonance and near-infrared mammography[131, 90]. Zhu *et al.* reported optical differentiation of benign versus malignant breast masses using ultrasound (US)-guided DOT system[132, 133, 134]. Fang *et al.* reported combined optical and x-ray tomosynthesis breast imaging[89, 88].

There are two types of approaches to including anatomical information into the DOT image reconstruction. One is the hard prior method, which is also known as parameter reduction[32]. In the hard prior method, the optical properties within the same region are forced to be uniform, which reduces the total number of unknowns from the node number in the finite element mesh to the number of distinct regions segmented from an anatomical image. The disadvantages of the hard prior method include its dependence on the accuracy of segmentation and a strong bias to the incomplete or incorrect structural priors. The second is referred to as the soft prior method[32], which allows different updates of the reconstructed optical properties in the same segmented region. However, both hard and soft priors require region segmentation from the anatomical images, which can only be performed by a radiologist or an expert of image processing. To eliminate the need for image segmentation, a direct regularization method in which the anatomical image gray-scale values are used to construct the regularization matrix was introduced to DOT[135, 136, 137].

In this paper, inspired by the kernel method of PET image reconstruction[138], we introduce the kernel method based image reconstruction as a new approach to include anatomical guidance into DOT. Compared with the conventional hard and soft prior approaches, the proposed kernel method does not require target

region segmentation. Compared with a direct regularization method proposed in Ref. [135], instead of utilizing single pixel intensities corresponding to the finite element nodes, we also use neighboring voxels, which allows us capture more structural information from the anatomical image. The kernel-based image model is directly incorporated into the forward model of DOT, which exploits the spatial smoothness of the image in the feature space.

In this study, we only consider the optical absorption coefficient contrast between the target and the background for simplification. In the proposed kernel method, the optical absorption coefficient at a node i is defined as a function of a set of features, $\boldsymbol{f}_i$,which is directly extracted from the voxel intensities of the corresponding anatomical images. Then, the kernelized DOT image model is incorporated into the forward model of DOT.

3.2 Methods

3.2.1 Kernel-based anatomically-aided reconstruction algorithm

In the inverse problem of DOT, the objective function (Ω), which minimizes the difference between modeled data (obtained from the forward model of DOT) and the measurements, if we only reconstruct the optical absorption coefficients, can be written as:

$$\Omega(\mu_a) = \frac{1}{2}||\boldsymbol{y} - \mathcal{F}(\mu_a)||_2^2 \tag{3.1}$$

where μ_a is the optical absorption coefficient and $\mathcal{F}(\mu_a)$ is the prediction from the DOT forward model in continuous wave mode. Here we present the Gaussian kernel method to encode anatomical information in the DOT image reconstruction. This can be accomplished by defining a kernel function for each finite element node. The optical absorption coefficient at node i can be written as a linear combination of kernels in a way similar to PET[139, 138, 140]

$$\mu_{ai} = \sum_j \alpha_j \kappa(\boldsymbol{f}_i, \boldsymbol{f}_j) \tag{3.2}$$

where $\boldsymbol{f}_i$ and $\boldsymbol{f}_j$ are are feature vectors corresponding to finite element node i and j from anatomical image, respectively. These anatomical feature vectors are directly extracted from the corresponding voxels in the 3-dimensional(3D) anatomical images for each finite element node. The finite element mesh and the anatomical images should be co-registered. It is also worth noting that the voxels corresponding to finite element nodes on the surface of the mesh and outside of the mesh are excluded from the feature vector extraction. The vector $\boldsymbol{\alpha}$ is referred to as the coefficient image to be reconstructed. There are a variety of choices of the kernel function κ[139, 141]. Here we use the radial Gaussian kernel[142],

$$\kappa(\boldsymbol{f}_i, \boldsymbol{f}_j) = exp(\frac{-||\boldsymbol{f}_i - \boldsymbol{f}_j||^2}{\sigma^2}) \tag{3.3}$$

where the parameter σ controls the edge sensitivity. The above kernel representation can be written in a matrix-vector form as

$$\boldsymbol{\mu}_a = \boldsymbol{K}\alpha \tag{3.4}$$

where the element (i, j) of the kernel matrix $\boldsymbol{K}$ is equal to $\kappa(\boldsymbol{f}_i, \boldsymbol{f}_j)$. For computational efficiency, a k-nearest neighbor(knn) search is carried out for each feature vector corresponding to each finite element node using the *knnsearch* function in MATLAB. The search is carried out according to Euclidean distance between the feature vectors, not a physical distance of finite element nodes in the Cartesian coordinate. Only those elements corresponding to the k-nearest neighbors are remained in the kernel matrix and the rest of them are set to be 0. This results in the following definition of the kernel matrix:

$$\boldsymbol{K}_{ij} = \begin{cases} \kappa(\boldsymbol{f}_i, \boldsymbol{f}_j), & \boldsymbol{f}_j \in knn \text{ of } \boldsymbol{f}_i \\ 0, & \text{otherwise} \end{cases} \tag{3.5}$$

by substituting (3.4) into (3.1), the kernelized objective function is obtained as

$$\Omega(\boldsymbol{\alpha}) = \frac{1}{2}||\boldsymbol{y} - \mathcal{F}(\boldsymbol{K}\alpha)||_2^2 \tag{3.6}$$

when $\boldsymbol{K}$ is an identity matrix, the above equation equal to the original objective function (3.1). By finding partial derivative of objective function on α and setting

it equal to zero:

$$\frac{\partial \Omega}{\partial \alpha} = \boldsymbol{K}^T \boldsymbol{J}^T \delta = 0 \tag{3.7}$$

where $\boldsymbol{\delta}$ is the data-model misfit, $\delta = \boldsymbol{y} - \mathcal{F}(\boldsymbol{K}\alpha)$, $\boldsymbol{J}$ is the Jacobian, and T is matrix transpose operator. Using the Taylor expansion of $\mathcal{F}(\boldsymbol{K}\alpha)$ around α_{n-1} gives us:

$$\mathcal{F}(\boldsymbol{K}\alpha_n) = \mathcal{F}(\boldsymbol{K}\alpha_{n-1}) + \boldsymbol{J}\boldsymbol{K}\Delta\boldsymbol{\alpha}_n + \cdots, \tag{3.8}$$

where $\Delta\boldsymbol{\alpha} = \boldsymbol{\alpha}_n - \boldsymbol{\alpha}_{n-1}$. Rewriting δ utilizing the first two terms of (3.8) (ignoring the rest, equivalently linearizing the problem) gives us

$$\delta_n = \boldsymbol{y} - \mathcal{F}(\boldsymbol{K}\alpha_n) = \boldsymbol{y} - \mathcal{F}(\boldsymbol{K}\alpha_{n-1}) - \boldsymbol{J}\boldsymbol{K}\Delta\alpha_n = \delta_{n-1} - \boldsymbol{J}\boldsymbol{K}\Delta\alpha_n \tag{3.9}$$

Rewriting (3.7) for the n^{th} iteration

$$\boldsymbol{K}^T \boldsymbol{J}^T \delta_n = 0 \tag{3.10}$$

Substituting (3.9) into (3.10), we have:

$$\boldsymbol{K}^T \boldsymbol{J}^T (\delta_{n-1} - \boldsymbol{J}\boldsymbol{K}\Delta\alpha_n) = 0 \tag{3.11}$$

Further simplification leads to an update equation

$$[\boldsymbol{K}^T \boldsymbol{J}^T \boldsymbol{J}\boldsymbol{K}]\Delta\alpha_n = \boldsymbol{K}^T \boldsymbol{J}^T \delta_{n-1} \tag{3.12}$$

since the matrix $\boldsymbol{K}^T\boldsymbol{J}^T\boldsymbol{J}\boldsymbol{K}$ is ill-conditioned, a diagonal term(the Tikhonov regularization) is added to stabilize the inverse problem. In this case the update equation becomes:

$$[\boldsymbol{K}^T \boldsymbol{J}^T \boldsymbol{J}\boldsymbol{K} + \lambda \boldsymbol{I}]\Delta\alpha_n = \boldsymbol{K}^T \boldsymbol{J}^T \delta_{n-1} \tag{3.13}$$

After the coefficient image α is obtained, the desired optical absorption coefficient image can be calculated as

$$\mu_a = \boldsymbol{K}\alpha \tag{3.14}$$

3.2.2 Numerical simulation

Optimization of the Kernel method

The voxel number for each corresponding node and the number of nearest neighbors in *knnsearch* are important parameters in constructing kernel matrix $\boldsymbol{K}$ and have significant effects on the kernel method. In this paper, we studied four different voxel numbers, 3×3×3, 5×5×5, 7×7×7, and 9×9×9. The lengths of feature vectors were 27, 125, 343, and 729 respectively. For *knnsearch*, three different values of k (16, 32, 64), the number of nearest neighbors, were also studied. To evaluate and compare the quality reconstructed DOT images quantitatively, we used a combinations of 4 metrics listed below. Their detailed definitions can be found in Ref. [44]. They are volume ratio (VR), Dice similarity coefficient (Dice), contrast-to-noise ratio (CNR), and mean square error (MSE). In general, for a reconstructed image to have better quality, it has a VR and Dice close to one, a small MSE, and a large CNR[143].

In the numerical simulations, we used a cylindrical phantom with a diameter of 78 mm and a height of 60 mm. A cylindrical target (diameter of 10 mm and height of 10 mm) was placed at 15 mm away from the center line of the phantom and 20 mm below the top surface of the phantom in the vertical direction as depicted in Figure 3.1(a). The numerical phantom was discretized into a 3D tetrahedral finite element mesh with 9,877 nodes, 54,913 elements and 2,921 surface nodes. Numerical DOT measurement data at six angular projections were generated by the DOT forward model[144]. In each angular projection, six source positions separated 5 mm apart were placed on one side of the phantom in the vertical line as indicated by the black dots in Figure 3.1(b). A rectangular region on the opposite side of the numerical phantom was chosen to be the field of view (FOV) and all surface nodes within this region were used as measurement detectors as indicated by the red dots in Figure 3.1(b). Then, 5% Gaussian noise (signal to noise ratio (SNR) of 36.85 dB) was added to the numerical DOT measurement data. The optical reduced scattering coefficient was set to 1 mm^{-1} for both target and background uniformly. The optical absorption coefficient was 0.007 mm^{-1} for the phantom background and 0.028 mm^{-1} for the target as shown in Table 3.1.

Table 3.1: Optical properties and geometry dimensions of the phantom for the numerical simulation.

	Diameter	**Height**	μ_a	μ_s'
Background	78.0 mm	60.0 mm	0.007 mm^{-1}	1.0 mm^{-1}
Target	10.0 mm	10.0 mm	0.028 mm^{-1}	1.0 mm^{-1}

A synthetic 3D CT image with a matrix size of 527×527×401 was generated with an isotropic voxel size of 0.15 mm as shown in Figure 3.1(c). The voxel intensities of target region and the background were set to 1.5 and 0.34, respectively, which are close to the CT image intensity in the phantom experiments described below. 5% white Gaussian noise (SNR of 36.85 dB) was also added to the synthetic CT images.

CT contrast effect in kernel method for CT guided DOT reconstruction

The voxel intensity in the CT image is used to generate the kernel matrix and therefore further analysis is required to assess how the ratio of the target pixel intensity to the background pixel intensity affects the performance of the proposed kernel method. For this purpose, 3 more synthetic CT images with different CT contrasts were used for the kernel method when $k = 64$ and voxel number of 7×7×7. In these simulations, the background voxel intensity of the CT image was set to be uniform as 0.34. For the target region, voxel intensity values of 0.68, 1.02, and 2.04 were used for the contrast ratios of 2:1, 3:1, and 6:1, respectively. For these three cases, all other factors such as the phantom geometry and optical properties were the same as described in the above section.

Effect of false positive guidance in the kernel method

A false positive target in the synthetic CT image (see Figure 3.1d) was used to investigate how false positive guidance affects the proposed kernel method. For this purpose, the top target is the true optical absorption target and the bottom target is the false optical absorption target. Both targets were defined with the

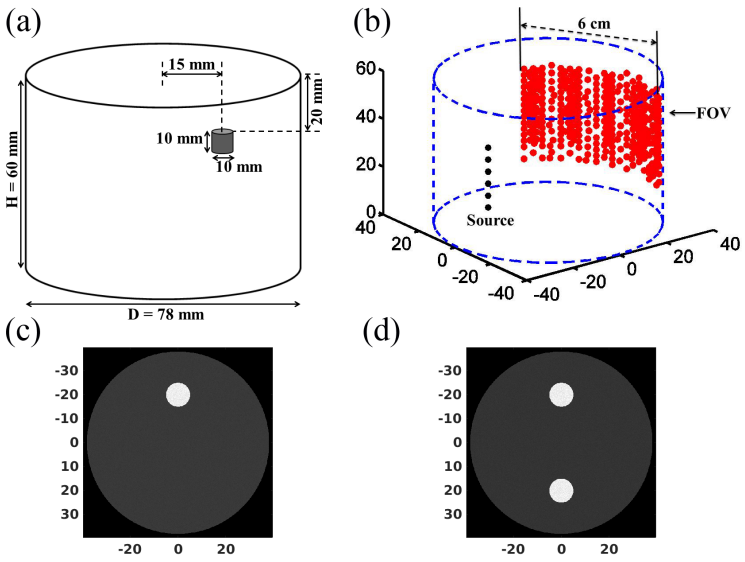

Figure 3.1: (a) Phantom geometry. (b) Source nodes (black) and detector nodes (red) in a 6 cm wide measurement patch for an angular projection.(c) One cross section of simulated CT image with 5% Gaussian noise. (d) The CT image with a true target (top) and a false positive target (bottom) used for the anatomical guidance in the false positive simulation.

same contrast and size in the CT images. In this numerical simulation, all other factors were the same as described in section 4.2.4.

Clinical breast CT image as anatomical guidance in the kernel method

The ultimate goal of the proposed kernel method in CT guided DOT is the applications in the clinical studies. Compared with the phantom CT image, the breast CT image has much more heterogeneous background and different CT contrast. In this study, a clinical breast CT image as shown in Figure 3.2(a) was used, in which the CT image at different coronal planes of the breast is plotted. This CT data set is from a 48-year old women presented for diagnostic workup of a palpable lump in the left breast at the one o'clock position. On mammography, she was found to have heterogeneously dense breast tissue and a mostly obscured 2 cm mass corresponding to the palpable finding. As part of a clinical trial, the patient underwent a contrast-enhanced dedicated breast CT scan 103 seconds after the injection of 100 mL of Visipaque 320 at a rate of 4 mL/sec. On the contrast-enhanced

breast CT image as shown in Figure 3.2(a), the oval 20x24x17mm (APxMLxSI) mass becomes conspicuous. The histopathology showed a low-grade infiltrating mammary carcinoma, which was estrogen and progesterone receptor positive and Her-2, negative. We have performed segmentation of the breast CT image and display the segmented image in Figure 3.2(b), where the highlight region is the oval mass and the grey region is the background. The segmentation was used in the soft prior method for anatomical guidance.

When the patient was scanned on the breast CT scanner, there was no optical imaging system. In this study, optical measurements were simulated with the forward model previously-reported by our group[144]. From the CT image, a 3D finite element mesh was generated with 27,146 tetrahedral elements, and 6,187 nodes, as displayed in Figure 3.2(c). Similar to the numerical phantom studies, numerical measurements in six angular projections were used with an angular step of 60 degrees. For each angular projection, we selected a patch with a width of 6 cm and a height of 4 cm to mimic the FOV of a CCD camera. All the surface nodes in the patch were used as DOT detectors. For each angular projection, we selected 6 nodes at the opposite side of the patch as the laser illumination position. The laser illumination position had an interval of 0.5 cm. The laser beam illuminated the six positions sequentially. For each illumination position, the light intensities on the detectors in the FOV were recorded as the measurements. With six angular projections, we have 36 laser source positions and 14,082 total measurements. We added 5% Gaussian noise (SNR of 36.85 dB) onto the numerical DOT measurement data. In the forward model, we have set the nodes in the target region with the optical absorption coefficient of 0.028 mm^{-1} and the reduced scattering coefficient of 1.0 mm^{-1}. The nodes in the background region had the optical absorption of 0.007 mm^{-1} and the reduced scattering coefficient of 1.0 mm^{-1}.

During the DOT reconstruction, for the kernel method, we used the breast CT image (Figure 3.2a) without segmentation as the anatomical guidance to generate the kernel matrix $\boldsymbol{K}$. For the soft prior method, we had to segment the breast CT image (Figure 3.2b) because the finite element nodes in the target region and the background should be known to generate the regularization matrix $\boldsymbol{L}$ in the soft

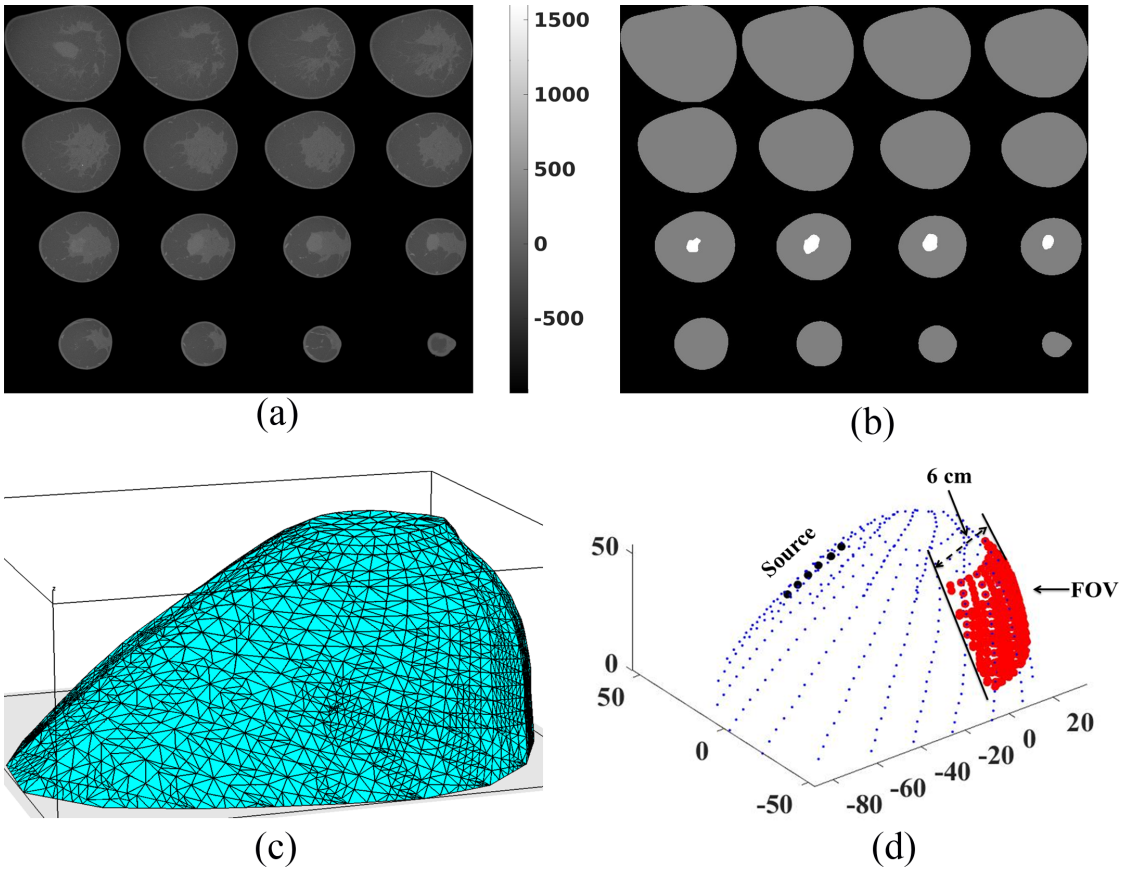

Figure 3.2: (a) Transverse sections of the CT image of a breast cancer patient. (b) The segmentation of the CT image shown in (a) where the tumor is highlighted. (c) The finite element mesh of the breast for DOT reconstruction. (d) The laser illumination positions (black dots) and the detector nodes (red dots) of a typical angular projection.

prior method[84].

3.2.3 Phantom experimental setup

In the phantom experiment, we used a cylindrical phantom with a diameter of 78 mm and a height of 60 mm that was made of 2% Agar, titanium dioxide (TiO_2) as scattering particles, Indian ink as an optical absorber, and water. A jelly-like agar phantom was fabricated with a through hole at the target location, which is 19.82 mm away from the center line of the cylinder. A cylindrical target with a diameter of 10.86 mm and a height of 13.63 mm was made inside a transparent

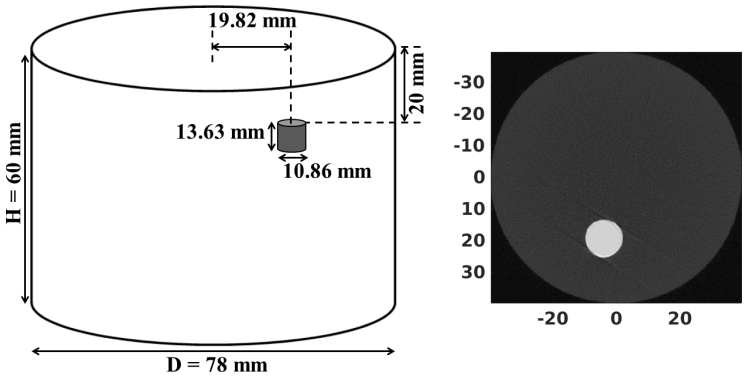

(a) (b)

Figure 3.3: (a) Phantom geometry. (b) One slice CT image of phantom in experiment

glass tube with a wall thickness of 0.3 mm. Then, the target inside the glass tube was inserted into the hole of the background phantom. The center of the target was 19.82 mm away from the center of the base phantom, which was calculated from the CT image. The top 20 mm and the bottom 30 mm of the hole were filled with the same material as the base phantom (Figure 3.3a). The base phantom was fabricated to have μ_a= 0.007 mm^{-1} and μ_s' = 1.0 mm^{-1} at the wavelength of 650 nm. The target had an optical absorption coefficient of 0.028 mm^{-1} and a reduced scattering coefficient of 1.0 mm^{-1} at the wavelength of 650 nm as listed in Table 3.2.

We used the same finite element mesh as that in the numerical simulation to discretize the agar phantom. The experimental measurement data were acquired with a DOT prototype system built in our lab that was consisted of an EMCCD camera (C9100-13,Hamamatsu) with a lens (CM 120 12101, Schneider Xenon 25mm f\0.95), a diode laser at 650 nm with a collimator (BWF-OEM-650-200-100-0.22, B&W Tek, Inc), a linear stage (XN10-0060-E01-71 C044289, Velmex, Bloomfield,NY) and a rotary stage (B4872TS-ZRS C042679, Velmex, Bloomfield,NY). Details of the prototype DOT imaging system were described in Ref. [144]. During the experiments, the EMCCD camera stayed stationary while the rotary stage rotated the phantom with an angular step of 60 degrees. For each rotation angle,

the linear stage moved the laser beam six steps in the vertical direction with a step size of 5 mm. For each illumination position, an image was taken by the EMCCD camera and mapped onto the detector nodes within the measurement patch depicted in Figure 3.1(b). This experimental setup generates same source-detector pairs as those in the numerical simulation. Measurement data were calibrated with a homogeneous phantom by the same approach as described in Ref. [98].

A CT volume data set with a matrix size of 470×470×368 and an isotropic voxel size of 0.169 mm was reconstructed using 500 projections acquired on a dedicated breast CT system. Details of the breast CT system were described in Ref. [93]. Briefly, the x-ray tube was operated at a current of 160 mA and the voltage of 50 kVp with 0.15 mm of added copper (Cu) filtration. 500 angular projections were acquired. A filtered back-projection algorithm was used to reconstruct the CT image with a Shepp-Logan filter. A coronal slice of the reconstructed CT data set used to calculate the target's size and position is shown in Figure 3.3(b). Because the optical absorption contrast alone does not have CT contrast, and only the glass tube was observed in the reconstructed CT images, we filled the target regions by pixels having the same CT contrast as the glass tube to provide anatomical guidance in the kernel method. The mean voxel intensities of the target region and the background are 1.50 and 0.34, respectively.

Table 3.2: Optical properties and geometry dimensions of the phantom for experiment

	Diameter	**Height**	$\boldsymbol{\mu_a}$	$\boldsymbol{\mu_s'}$
Background	78.0 mm	60.0 mm	0.007 mm^{-1}	1.0 mm^{-1}
Target	10.86 mm	13.63 mm	0.028 mm^{-1}	1.0 mm^{-1}

3.3 Results

3.3.1 Numerical Simulation Results

Optimization of the kernel method

Numerical simulation with one target was conducted to evaluate the proposed kernel method. The geometric and optical properties of the numerical phantom are described in section 4.2.4. Figure 3.4(a) shows transverse sections of the ground truth optical absorption coefficient image of the simulation phantom. Numerical measurements were generated by the DOT forward model as described in section 4.2.4. First, for comparison, we reconstructed the DOT image by Levenberg-Marquardt algorithm with the CT structural guidance through the approaches of soft prior and without any structural guidance, respectively[84]. The reconstructed optical absorption coefficient image is plotted in Figure 3.4(b) for the case without the structural prior and Figure 3.4(c) for the case with the soft prior. Figure 3.4(b) indicates that the reconstructed optical absorption coefficient in the target region is nearly half of its true value we assigned in the simulation, and there are strong artifacts near the bottom and top boundaries of the cylindrical phantom. With the soft prior method, we can reconstruct very good optical absorption coefficient image with accurate target size and optical absorption coefficient in the target region as shown in Figure 3.4(c), which is consistent with our previous studies[145, 144]. Then, we performed the DOT reconstruction with the proposed kernel DOT. To investigate how the parameters in the kernel method affect the DOT reconstruction, we studied four different voxel numbers (3×3×3, 5×5×5, 7×7×7, and 9×9×9) and three different nearest neighbors (k = 16, 32, 64) with 12 combinations of the kernel-based DOT reconstructions. Reconstructed DOT images with fixed voxel number (3×3×3) and different k of 16, 32, 64 are plotted at the middle row of Figure 3.4, from which we find that k = 64 outperformed the the cases with k = 16 and k = 32. The bottom row of Figure 3.4 shows the reconstructed DOT images with the kernel method for a fixed k = 64 and different voxel numbers of 5×5×5, 7×7×7, and 9×9×9. From these figures, it is seen that the qualities of the reconstructed DOT images are slightly improved by increasing

the number of voxel for the kernel method.

Table 3.3: For the numerical simulation, the calculated VR, Dice, CNR and MSE with kernel method for different numbers of nearest neighbor k and different voxel numbers, with soft prior and no prior.

k	Voxel size	VR	Dice	CNR	MSE
16	**3×3×3**	0.47	0.64	30.35	3.51e-07
32	**3×3×3**	0.52	0.68	31.57	3.37e-07
64	**3×3×3**	0.52	0.68	32.32	3.28e-07
64	**5×5×5**	0.52	0.68	32.43	3.30e-07
64	**7×7×7**	0.52	0.68	32.51	3.26e-07
64	**9×9×9**	0.52	0.68	32.50	3.27e-07
Soft prior		1.0	1.0	891.03	3.51e-08
No prior		1.19	0.04	3.78	1.52e-06

To evaluate the simulation results quantitatively, we calculated image quality metrics such as VR, Dice, CNR, and MSE for the reconstructed DOT images in Figure 3.4 for the cases without anatomical guidance case (Tikhonov regularization alone), with the soft prior method and the six combinations of the kernel method. We have listed the quantitative image quality metrics in Table 3.3, which indicates that the reconstruction with the soft prior method is the best with VR and Dice coefficients of 1 and the lowest recorded MSE. We also see that the DOT reconstruction without any structural guidance is the worst with a VR much less than 1 and a Dice coefficient of 0. For the cases with kernel method, MSE decreased nearly linearly when k and voxel number increased. Reconstructed DOT image for k=64 and voxel number of 7×7×7 is the best among all the cases of the kernel method with the highest CNR of 32.51 and the lowest MSE of 3.26e-07. VR and Dice coefficients are the same for all the combinations of the kernel method, except for the case k=16 and voxel number of 3×3×3 with the lowest VR of 0.47 and Dice of 0.64.

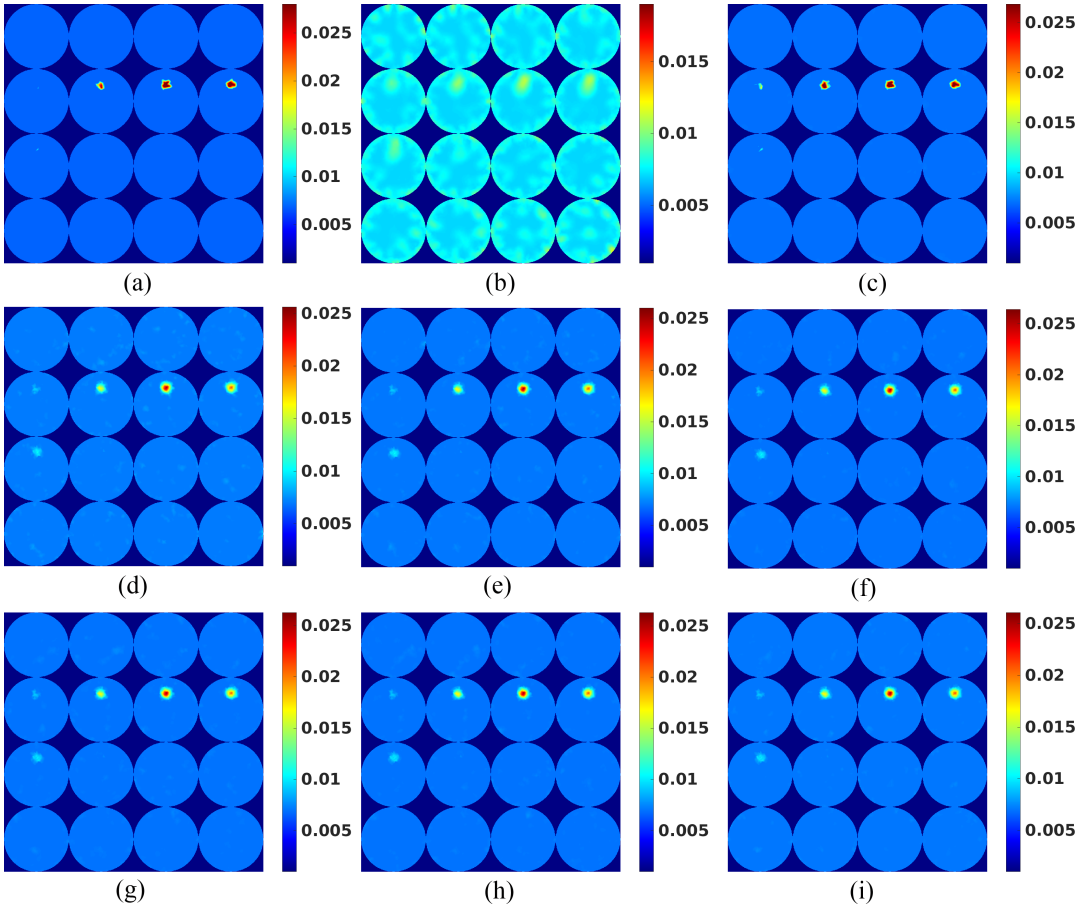

Figure 3.4: The optical absorption coefficient images for numerical simulation. (a) Ground truth image; (b) the reconstructed image without structural prior; (c) reconstructed image with soft prior from the CT guidance. The reconstructed optical absorption coefficient images with kernel method for a fixed voxel numbers of 3×3×3 and (d) $k = 16$, (e) $k = 32$, (f) $k = 64$; and for a fixed $k = 64$ with different voxel number of (g) 5×5×5, (h) 7×7×7, (i) 9×9×9.

CT contrast effect in kernel method for CT guided DOT reconstruction

The reconstructed optical absorption coefficient images with the kernel method when k=64 and voxel number of 7×7×7 are plotted in Figures 3.5a, 3.5b, and 3.5c for the CT contrast 2:1, 3:1, and 6:1, respectively. Figure 3.5 indicates that the reconstructed images are similar to those in the previous simulations, in which the CT contrast is 4.4:1. The quantitative image metrics were calculated and listed in Table 3.4, from which we see that the metrics are also very close for these three cases, although the case with the contrast of 6:1 has slightly better CNR and MSE values, but lower VR and Dice coefficients. These results indicate that the proposed kernel method does not require a high CT contrast for its guidance in DOT reconstruction.

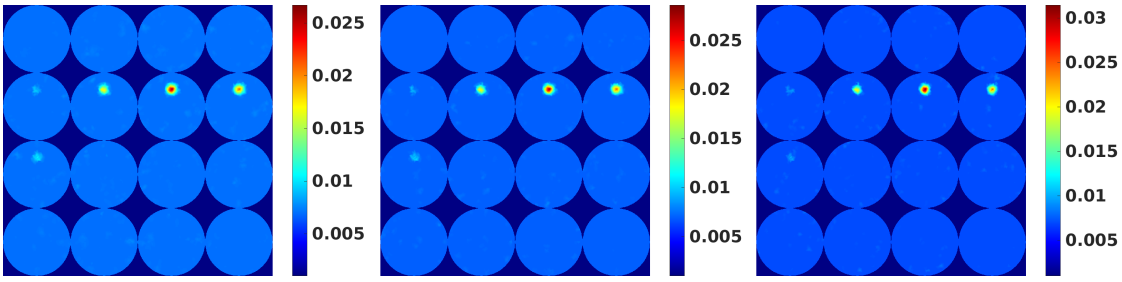

(a) (b) (c)

Figure 3.5: Reconstructed DOT images with the kernel method for a fixed voxel numbers of 9×9×9 and k = 64 with the structural guidance from the CT images of different contrasts: (a) 1:2, (b) 1:3, (c) 1:6.

Table 3.4: The calculated VR, Dice, CNR and MSE for the reconstructed optical absorption coefficient images as shown in Figure 3.5 with different background to target CT contrasts.

CT contrast	VR	Dice	CNR	MSE
1:2	0.57	0.72	33.09	3.23e-07
1:3	0.57	0.72	34.63	2.94e-07
1:6	0.47	0.65	35.33	2.68e-07

Effect of the false positive target in the kernel method

Using the anatomical guidance from the simulated CT image with a false positive target, we have performed the DOT reconstruction with both the soft prior and the kernel method. For the soft prior method, we have tried different regularization parameters and plotted the best reconstructed image in Figure 3.6(b). For the kernel method, we used the optimized parameters as $k = 64$ and voxel numbers of 7×7×7 and the reconstructed optical absorption coefficient image is plotted in Figure 3.6(c). Compared with the ground truth image plotted in Figure 3.6(a), it is clear that there is no false positive target observed in the reconstructed DOT images when both the soft prior method and the kernel method were used as shown in Figure 3.6(b) and Figure 3.6(c), respectively. It is also confirmed by the profile plot (as shown in Figure 3.6d) across the dotted line in Figure 3.6(a). From the profile plot, it is seen that there is no false positive target for the kernel method and a negligible false positive target for the soft prior method as the slight bump in the profile plot. This indicates that the kernel method is robust to the false positive guidance in the anatomical image.

Clinical breast CT image as anatomical guidance

The ground truth image is plotted in Figure 3.7(a). We have also performed the DOT reconstruction without any anatomical guidance for this case and the reconstructed optical absorption coefficient image is plotted in Figure 3.7(b), from which it is seen that the target is barely reconstructed. One possible reason is that we only used the measurements from six angular projections, which is not optimized for the DOT reconstruction without anatomical guidance. We have also reconstructed the optical absorption coefficient images with the soft prior method (Figure 3.7c) and the kernel method (Figure 3.7d). Both methods have reconstructed the target very well. It is not surprising to see that the reconstructed target in Figure 3.7(c) has a sharp boundary because segmentation of the target was applied in the soft prior method without adding any error. With the anatomical guidance from the CT image directly without segmentation, the kernel method with k=64 and the voxel number of 7×7×7 performed well without introducing

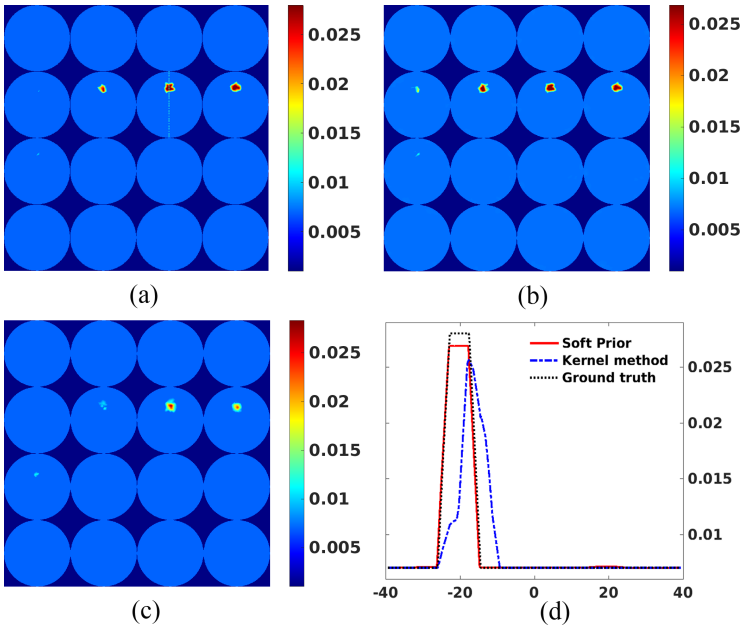

Figure 3.6: The optical absorption coefficient image: (a) the ground truth image; (b) the reconstructed image with soft prior; (c) the reconstructed image with the kernel method. (d) profile plot across the dotted line in figure (a)

any false positive targets from the fibroglandular tissues that are clearly seen in the CT image surrounding the oval mass as shown in Figure 3.7(c). We have also calculated the image quality metrics to evaluate the reconstructed DOT image quantitatively and listed them in Table 3.5.

Table 3.5: For Simulation with breast CT image, the calculated VR, Dice, CNR, and MSE for images in Figure 3.7.

	VR	**Dice**	**CNR**	**MSE**
No prior	0.35	0.0	1.37	1.14e-05
Soft-prior	1.0	1.0	36.78	1.06e-06
Kernel method	0.59	0.74	28.00	4.09e-07

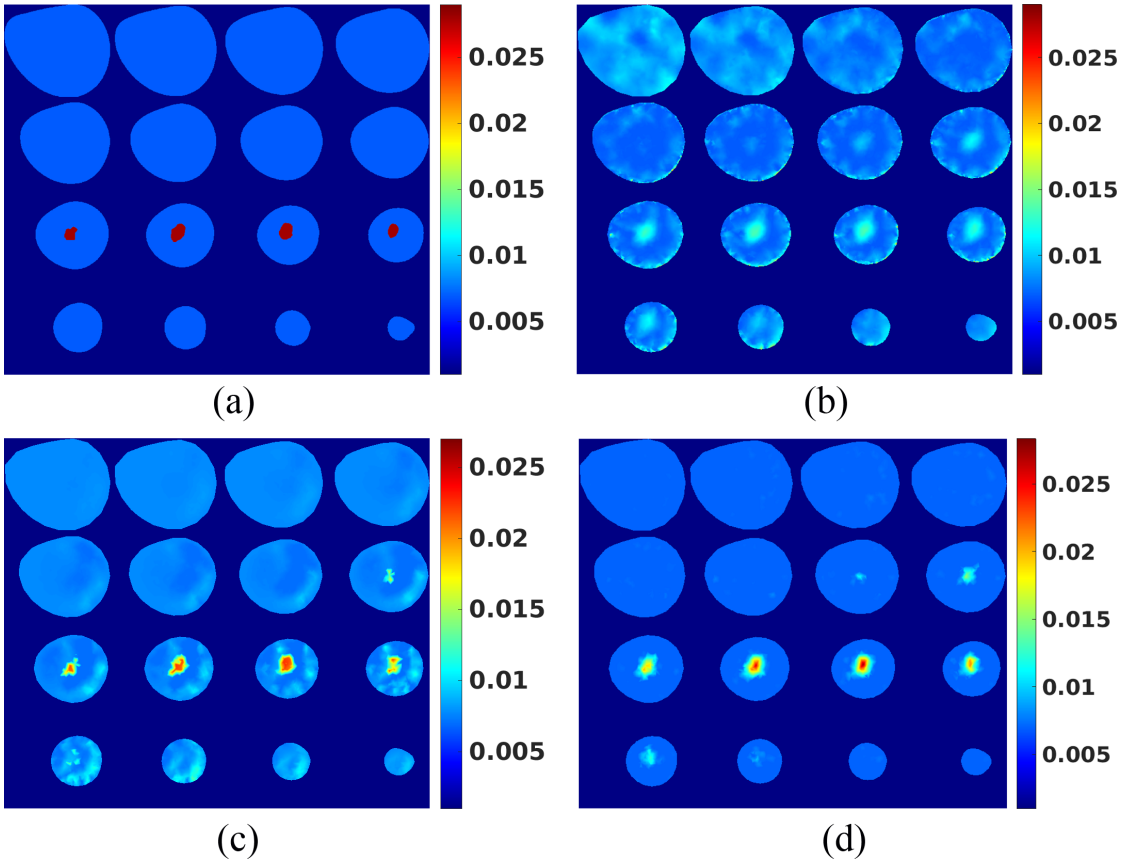

Figure 3.7: Reconstructed optical absorption coefficient images using the clinical breast CT image as anatomical guidance with (a) the ground truth image; (b) without the structural guidance; (c) the soft prior method and (d) the kernel method.

3.3.2 Phantom experimental results

An Agar Phantom experiment with one target was conducted to evaluate the proposed kernel method. Phantom geometries and the DOT prototype system are described in section 4.2.5. Figure 3.3(b) shows a cross section of the phantom CT image obtained from dedicated breast CT scanner. As described in the numerical simulation, we have performed the DOT reconstruction of this phantom experiment without the structural prior, with the structural prior through the method of soft-prior, and with the structural guidance by the proposed kernel method of 12 different cases with 3 different nearest neighbor k (16, 32, 64) and 4 different voxel numbers (3×3×3, 5×5×5, 7×7×7, 9×9×9). The reconstructed optical absorption coefficient images are plotted in Figure 3.8(a), for the case without the structural guidance, Figure 3.8(b), for the soft-prior case, and Figure 3.8(c) for the kernel method with k=64 and a voxel number of 7×7×7). Figure 3.8(c) is the best case among all the 12 cases of the kernel method. Figure 3.8(a) indicates that the target is missed for the DOT reconstruction without any structural guidance. From Figure 3.8(b), we see that the target is reconstructed at the right location, but the maximum value of optical absorption coefficients inside the target region is less than the true value. As indicated by Figure 3.8(c), the kernel method with $k = 64$ and the voxel number of 7×7×7 has a good reconstructed image. We calculated the image quality metrics for the results in Figure 3.8 and listed them in Table 4.4, from which, we know that the reconstructed image with the soft-prior method has the best metrics as we see in the numerical simulations. The main reason is that we extracted the target and background regions accurately from the CT image and did not add any noise in the soft prior guidance. However, the optical absorption coefficients in the target region are less than the true value. The kernel method reconstruction has the comparable results with the soft prior method in terms of the image evaluation metrics and has slightly better accuracy of the reconstructed value in the target region than the soft prior method.

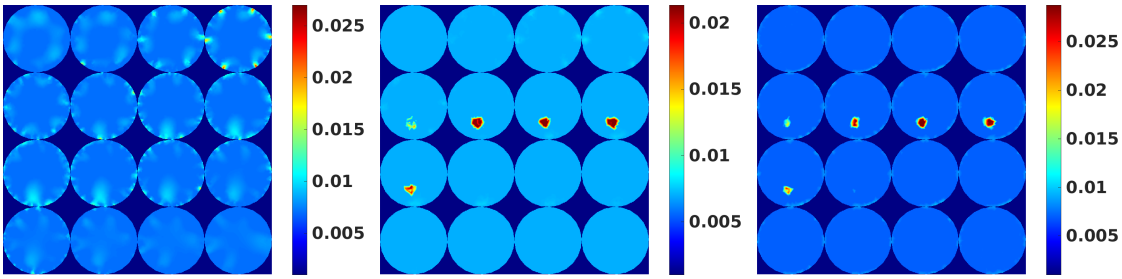

(a) (b) (c)

Figure 3.8: Reconstructed DOT images of the phantom experiment: (a) without the structural guidance; (b) with the structural guidance through the soft-prior method; (c) with the structural guidance by the kernel method ($k = 64$, voxel number 7×7×7).

Table 3.6: For the phantom experiment, the calculated VR, Dice, and CNR for images in Figure 3.8.

	VR	**Dice**	**CNR**
No prior	0.875	0.0	0.4842
Soft-prior	1.0	1.0	246.20
Kernel method	0.650	0.758	16.03

3.4 Discussions and Conclusion

We proposed a kernel method to introduce the anatomical guidance into the DOT image reconstruction. Compared with the conventional structural prior guided DOT reconstruction algorithms, such as soft prior, the proposed method has the advantages of not requiring the image segmentation and region classification as demonstrated by Figure 3.7. With the correct guidance as shown in Figure 3.4, the soft prior outperforms the proposed kernel method with better VR and DICE coefficient. However, the proposed methods yields higher optical absorption coefficients in the numerical simulation with breast CT data and phantom experiment. It also yields less artifacts near the source locations than the soft prior method as shown in Figure 3.7. Key parameters in this proposed method

are the voxel number and k-nearest neighbor. From the simulation study, we can see that k-nearest neighbor has signification impact to improve the quality of reconstructed image. However, voxel numbers are not changing the quality of the reconstructed images significantly, while increasing the computation time. In this study, we conclude k-nearest neighbor as k=64 and voxel number of 7×7×7 as optimum parameter.

In this study, we validated the proposed kernel method with both numerical simulations and phantom experiments. We only reconstructed the optical absorption coefficient images because our initial project goal is to reconstruct the hemoglobin concentration that is closely related to the optical absorption coefficient. We believe our current study is sufficient to validate the proposed kernel method, while, in the future we will apply the kernel method to reconstruct both the optical absorption and the reduced scattering coefficient images.

The proposed kernel method is validated by the CT image guidance. It is straightforward to apply the proposed kernel method for DOT imaging with other anatomical guidance such as MRI[91, 146]. We have studied the simultaneous PET and fluorescent molecular tomography (FMT) imaging for studies with mice model[147]. The proposed kernel method can be applied to the future PET guided DOT for the breast cancer imaging because a breast dedicated PET scanner has a spatial resolution of about 2.5 mm which is much higher than that of the DOT imaging[148].

In summary, simulation and phantom experiment results have validated the kernel method. Our results indicate that the higher number of nearest neighbors and larger voxel size improve the quality of the reconstructed images. The numerical simulation results indicate that the proposed kernel method is robust to CT contrast and the false positive targets in the guided CT image. With the clinical breast CT image, we demonstrated that we do not need the segmentation for the kernel method. Future work includes investigating the effects of false negative prior information in anatomical images on the performance of the proposed method. Moreover, a thorough examination of this method with a clinical data will be conducted in the future.

Chapter 4

Anatomical image guided fluorescence molecular tomography reconstruction using kernel method

4.1 Introduction

Fluorescence molecular tomography (FMT) has been emerging as an optical imaging modality for many years. FMT, as an important molecular imaging tool, has a broad range of applications in biomedical studies from drug development in small animal models[149, 150, 151, 152, 153, 154, 155, 156] to the clinical diagnosis in humans[157, 158, 159]. However, due to the strong scattering nature of optical photons in deep tissues and a limited number of measurements, the inverse problem of FMT is ill-posed and under-determined, which results in low spatial resolution in FMT imaging, in particular for targets in deep turbid media.

Many approaches have been proposed to improve the FMT image quality, including the use of multispectral wavelengths for both excitation and emission wavelengths, different illumination patterns[160, 161], charge-coupled device(CCD) cameras to increase the number of measurements[162, 163, 43, 164, 165],and im-

proved FMT reconstruction algorithms, especially the sparse enhancement FMT reconstruction for the sparse FMT targets[166, 167, 168, 169, 42, 170]. A region reconstruction methods implemented with level set method was also introduced to improve the FMT image reconstruction[171, 172]. A thorough review of FMT imaging in terms of instruments, methods and applications was presented in Ref.[173].

Although numerous efforts have been implemented to improve FMT, its spatial resolution is inferior to the other functional imaging modalities such as functional magnetic resonance imaging (fMRI), single-photon emission computed tomography (SPECT), and positron emission tomography (PET). To further improve the spatial resolution of FMT, structural guidance from anatomical images have been introduced into the FMT[174, 55, 152, 175]. Davis *et al.* reported the magnetic resonance imaging (MRI)-coupled FMT implemented with Laplacian-type regularization.[158, 174, 151, 54, 153]. Schulz *et al.* reported a hybrid system for simultaneous FMT and X-ray computed tomography[55, 176, 155, 156].Stuker *et al.* reported combined MRI and FMT system using single photon avalanche diode detectors[177]. Recently, microscopic positron emission tomography (microPET), with a spatial resolution up to 1 mm, has been used to guide FMT imaging[175, 178]. More recently, tri-modality[179] and even pentamodal tomographic imaging systems were also investigated[180].

One of major challenges in a multimodality FMT system is how to utilize anatomical information properly and easily in the FMT reconstruction. Soft prior method is a widely accepted approach, which allows variations within the regions. Local Laplace and weighted segments have also been introduced to FMT reconstruction[176, 55].It has been demonstrated that the combination of Laplace with weighted segments performed best in terms of quantification and localization. However, both methods require image segmentation, which is time-consuming and prone to human error. To eliminate the need for direct prior image segmentation, Holt *et al.* reported a direct regularization method, in which the anatomical image gray-scale values are introduced into a regularization operator[181]. Similarly, our proposed kernel method also eliminates the need for anatomical image segmenta-

tion. The major difference is that our approach does not need the regularization operator, which allows us to have maximum flexibility to implement this method.

In this paper, inspired by the kernel method in PET image reconstruction[138], we introduce the kernel-based image reconstruction as a new approach to incorporating anatomical guidance into FMT. Compared with the Laplacian-type regularization methods, the proposed kernel method does not require the target region segmentation. Furthermore, as demonstrated by the numerical simulations in this paper, the proposed kernel method is also robust to the false positive guidance and inhomogeneity in the anatomical images.

In the kernel method, the fluorophore concentration at a node i is defined as a function of a set of feature vectors, $\boldsymbol{f}_i$, which is directly extracted from the voxel intensities of the corresponding anatomical 3D images. Then, the kernelized FMT image model is incorporated into the forward model of FMT. Due to the simplicity of this model, we can combine it with any FMT reconstruction algorithm. In this study, we used a kernelized projection model of FMT with majorization-minimization (MM) approach[44, 143].

The rest of the paper is organized as follows: in Section 4.2, we describe the FMT forward model, the regularized reconstruction method of FMT, and the proposed kernel-based reconstruction algorithm. In Section 4.3, numerical simulations and experimental results are presented. Finally, we conclude the paper with discussions in Section 4.4.

4.2 Methods

4.2.1 Forward model and reconstruction algorithms of FMT

Light propagation in tissues is dominated by optical scattering and can be modeled by the diffusion equation[3]. For FMT in the continuous wave (CW) domain, the light propagation model in 3D is described by a set of coupled differential equations which are given below[40, 41]:

$$\begin{cases} -\nabla \cdot [D_{ex}(\boldsymbol{r})\nabla\Phi_{ex}(\boldsymbol{r})] + \mu_{\alpha,ex}\Phi_{ex}(\boldsymbol{r}) &= \delta_s(\boldsymbol{r}-\boldsymbol{r}_s) \\ \boldsymbol{n}\cdot[D_{ex}(\boldsymbol{r})\nabla\Phi_{ex}(\boldsymbol{r})] + \alpha_{ex}\Phi_{ex}(\boldsymbol{r}) &= 0 \\ -\nabla \cdot [D_{em}(\boldsymbol{r})\nabla\Phi_{em}(\boldsymbol{r})] + \mu_{\alpha,em}\Phi_{em}(\boldsymbol{r}) &= \Phi_{ex}(\boldsymbol{r})\boldsymbol{x}(\boldsymbol{r}) \\ \boldsymbol{n}\cdot[D_{em}(\boldsymbol{r})\nabla\Phi_{em}(\boldsymbol{r})] + \alpha_{em}\Phi_{em}(\boldsymbol{r}) &= 0 \end{cases} \tag{4.1}$$

where ∇ denotes the gradient operator, $D(\boldsymbol{r}) = \{3[\mu_s'(\boldsymbol{r})+\mu_a(\boldsymbol{r})]\}^{-1}$ is the diffusion coefficient, $\mu_\alpha(\boldsymbol{r})$ is the absorption coefficient and $\mu_s'(\boldsymbol{r})$ is the reduced scattering coefficient. $\Phi(\boldsymbol{r})$ is the photon fluence at the location $\boldsymbol{r}$. $\delta_s(\boldsymbol{r}-\boldsymbol{r}_s)$ is Dirac delta function defining point sources,and $\boldsymbol{r}_s$ is the location of the excitation point source. $\boldsymbol{x}$ is the product of the unknown fluorescent dye concentration and the quantum yield at each node to be reconstructed[42], $\boldsymbol{n}$ is the outward unit normal vector of the boundary, and α is the Robin boundary coefficient. In Eq. (4.1), subscripts ex and em mean corresponding terms at the excitation and emission wavelengths, respectively. Eq. (4.1) can be solved by the finite element method (FEM) based on a finite element mesh and is linearized to the following equation:

$$K_{ex}\Phi_{ex} = \delta_s(\boldsymbol{r}-\boldsymbol{r}_s), \quad K_{em}\Phi_{em} = \Phi_{ex}\boldsymbol{x} \tag{4.2}$$

where K_{ex} and K_{em} are the stiffness matrices at the excitation and emission wavelengths, respectively. With the conjugate gradient approach[43], the above equations can be described as[40]:

$$\boldsymbol{A}\boldsymbol{x} = \boldsymbol{b} \tag{4.3}$$

where $\boldsymbol{A} \in \mathbf{R}^{N_m \times N_n}$ is the system matrix, $\boldsymbol{x} \in \mathbf{R}^{N_n \times 1}$ is the unknown fluorephore distribution or the FMT image to be reconstructed, $\boldsymbol{b} \in \mathbf{R}^{N_m \times 1}$ is the measurement vector, N_n is the finite element node number, and N_m is the number of measurement.

Because of the ill-conditioned and ill-posed nature, Eq. (4.3) is usually solved as regularized least square problem with the non-negativity constraint:

$$\boldsymbol{x} = \arg\min_{\boldsymbol{x},\boldsymbol{x}\geq\boldsymbol{0}} \Phi(\boldsymbol{x}) =: ||A\boldsymbol{x}-\boldsymbol{b}||_2^2 + \lambda||\boldsymbol{x}||_1 \tag{4.4}$$

where λ is the L_1 regularization parameter.

In this study, for the case without anatomical guidance, Eq. (4.4) is solved by the MM approach that updates the FMT image iteratively to minimize the mismatch between the model predictions and the measurements[44, 143, 41].

4.2.2 Soft prior method

When structured priors are present, the objective function of the FMT with Laplacian regularization will be:

$$\boldsymbol{x} = \arg\min_{\boldsymbol{x},\boldsymbol{x}\geq\boldsymbol{0}} \Phi(\boldsymbol{x}) =: ||A\boldsymbol{x} - \boldsymbol{b}||_2^2 + \lambda||\boldsymbol{L}\boldsymbol{x}||_2^2 \tag{4.5}$$

In soft prior method, regularization matrix $\boldsymbol{L}$ is defined as[158]:

$$\boldsymbol{L}_{ij} = \begin{cases} 1, & \text{for } i = j \\ -\frac{1}{N}, & \text{if } i \text{ and } j \text{ are in the same region} \\ 0, & \text{otherwise} \end{cases} \tag{4.6}$$

where N is number of node in that region. In Eq. 4.5, regularization term $||\boldsymbol{L}\boldsymbol{x}||_2^2$ can be treated as special case of $||A\boldsymbol{x} - \boldsymbol{b}||_2^2$ when $\boldsymbol{b} = 0$. Then it can solved by the MM approach described in Refs. [44, 143, 41]

4.2.3 Kernel based anatomically-aided reconstruction algorithm

The anatomically-aided FMT reconstruction algorithms usually incorporate the anatomical guidance as a regularization matrix, which enhances the smoothness within the anatomical regions and also allows sharp transition between the different regions[181]. In this paper, we introduce the kernel method which includes the anatomical guidance into the projection model of FMT. The fluorophore distribution at the node i is defined with a kernel function as[182, 183, 138]

$$\boldsymbol{x}_i = \sum_j \boldsymbol{\alpha}_j \kappa(\boldsymbol{f}_i, \boldsymbol{f}_j) \tag{4.7}$$

where $\boldsymbol{f}_i$ and $\boldsymbol{f}_j$ are the anatomical feature vectors corresponding to the finite element nodes of i and j, respectively. These anatomical feature vectors are directly extracted from the corresponding voxels in the 3D anatomical images for

each finite element node. The finite element mesh and the anatomical images should be co-registered. In some reported multimodality FMT systems, accurate co-registrations were reported[155, 177], which makes the proposed method is easy to be implemented. It is also worth pointing out that voxel corresponding to finite element nodes on the surface of the mesh and outside of the mesh are excluded from the feature vector extraction. The length of the feature vectors depends on the voxels number. For example, for a voxel number of 3×3×3, the length of the feature vector is 27.

In Eq. 4.7, κ is the kernel function. There are a variety of choices of the kernel function κ[141, 184]. Here we use the radial Gaussian kernel[142],

$$\kappa(\boldsymbol{f}_i, \boldsymbol{f}_j) = exp(\frac{-||\boldsymbol{f}_i - \boldsymbol{f}_j||^2}{\sigma^2}) \tag{4.8}$$

where the parameter σ controls the edge sensitivity and yields more accurate results when $\sigma = 1$[185]. For computational efficiency, a k-nearest-neighbor (knn) search is carried out for each feature vector corresponding to each finite element node using the *knnsearch* function in MATLAB. The search is carried out according to Euclidean distance between the feature vectors, not a physical distance of finite element nodes in the Cartesian coordinate. Only those elements corresponding to the k-nearest-neighbors are stored in the kernel matrix and the rest of them are set to be 0. This will result in the following definition of kernel matrix:

$$\boldsymbol{K}_{ij} = \begin{cases} \kappa(\boldsymbol{f}_i, \boldsymbol{f}_j), & \boldsymbol{f}_j \in knn \text{ of } \boldsymbol{f}_i \\ 0, & \text{otherwise} \end{cases} \tag{4.9}$$

Thus, the kernel matrix is a sparse symmetric $N_n \times N_n$ matrix. The kernel matrix is normalized in this study for higher image quality[138]:

$$\bar{\boldsymbol{K}} = diag^{-1}[\boldsymbol{K}\boldsymbol{1}_N]\boldsymbol{K} \tag{4.10}$$

here $\boldsymbol{1}_N$ is a vector of all ones. Eq. (4.7) can be written in matrix-vector form:

$$\boldsymbol{x} = \bar{\boldsymbol{K}}\boldsymbol{\alpha} \tag{4.11}$$

where the vector $\boldsymbol{\alpha}$ is a new unknown vector referred as the coefficient image. By substituting Eq.(4.11) into (4.3), the kernelized inverse problem the FMT can be

written as

$$\boldsymbol{A}\bar{\boldsymbol{K}}\boldsymbol{\alpha} = \boldsymbol{b} \tag{4.12}$$

Combining the kernelized projection model (4.12) with objective function (4.4) leads to the following objective function:

$$\boldsymbol{\alpha} = \arg\min \Phi(\boldsymbol{\alpha}) =: ||\boldsymbol{A}\bar{\boldsymbol{K}}\boldsymbol{\alpha} - \boldsymbol{b}||_2^2 + \lambda||\boldsymbol{\alpha}||_1 \tag{4.13}$$

Because the reconstructed images are already regularized by the kernels, we set regularization parameter in Eq. (4.13) to zero in this study[138], and solved by the MM approach[44, 143].Once $\boldsymbol{\alpha}$ is obtained we can easily obtain the final fluorophore distribution image by the linear transformation $\boldsymbol{x} = \bar{K}\boldsymbol{\alpha}$.

4.2.4 Numerical simulation setup

Cylindrical simulation phantom

In this simulation, we used a cylindrical phantom with a diameter of 22 mm and a height of 80 mm. Cylindrical targets with a diameter of 1.4 mm and a length of 20 mm were embedded 20 mm below the top surface of the phantom. In the coordinate system, the base of the cylinder was a circle on the x-y plane centering the origin of the coordinate system and the height was along the z-axis. In this simulation, two targets were embedded at (-1.7,5.56) and (1.7,5.56) in the x-y plane with an edge-to-edge distance of 2 mm as shown in Fig. 4.1(a).

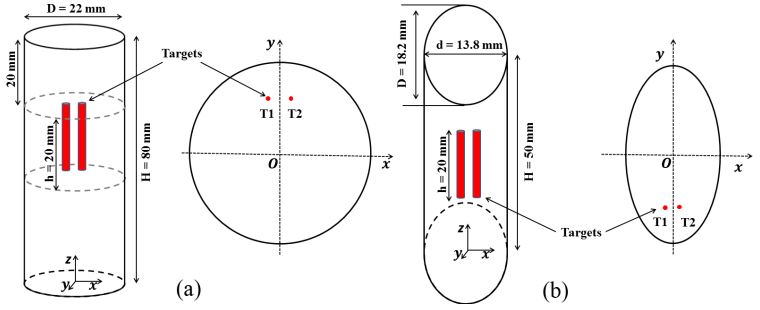

Figure 4.1: Numerical simulation phantom geometry of (a) the cylindrical phantom with target locations at T1 (-1.7, 5.56) and T2 (1.7, 5.56) and (b) the elliptic cylindrical phantom with target locations at T1 (-1.2, -5.0) and T2 (1.2, -5.0).

In this and following simulations, the phantom tissue optical properties were set to be μ_a= 0.012 mm^{-1} and μ_s'= 0.83 mm^{-1} at both the excitation wavelength (650 nm) and the emission wavelength (700 nm). We assigned the fluorophore concentration to be 1 in the target regions and 0 in the background regions. The numerical phantom was discretized with a 3-dimensional (3D) tetrahedral finite element mesh with 29,989 nodes and 155,310 elements. Numerical FMT measurement data was generated by Eq. (4.3) with a line pattern laser projected on the phantom surface. The line laser had a width of 1 mm and a length of 50 mm. We had 30 excitation positions of the line laser to cover the whole surface[186]. For each line laser excitation, the 9,280 surface nodes on the side of the cylinder were used as the measurement detectors. Then, we added 30% Gaussian noise to the numerical FMT measurement data.

The 3D CT images with 220×220×801 voxels was generated with the grid size of 0.1 mm. The intensities of target regions and the background were set to 0.24 and 0.06, respectively, which are close to the CT data in phantom experiment. We added 15% white Gaussian noise to the numerical CT images.

Elliptic Cylindrical numerical phantom

In this simulation,we used an elliptic cylindrical phantom with a horizontal semi-axis of 6.9 mm, vertical semi-axis of 9.2 mm and a height of 50 mm. Cylindrical targets with a diameter of 1.4 mm and a length of 20 mm were embedded 20 mm below the top surface of the phantom. In the coordinate system, the base of the cylinder was an ellipse on the x-y plane centering the origin of the coordinate system and the height was along the z axis. Two targets were embedded at (-1.2,-5.0) and (1.2,-5.0) in the x-y plane with an edge-to-edge distance of 1 mm as showed in Fig. 4.1(b). The phantom geometry was discretized with a 3D tetrahedral finite element mesh with 32,882 nodes and 191,359 elements. Numerical FMT measurement data were generated by Eq. (4.3) with a line pattern laser projected on the phantom surface. The line laser had a width of 1 mm and a length of 50 mm. We had 30 excitation positions of the line laser to cover the whole surface[186]. For each line laser excitation, the 6,013 surface nodes on the side surface of the

cylinder were used as the measurement detectors. Then, we added 30% Gaussian noise to the numerical FMT measurement data.

The transverse sections of CT image were generated using the "*phantom*" command in MATLAB (as shown in Fig. 4.5 in the result section). The area outside of the ellipse was trimmed. Then we stacked the phantom images to generate a 3D CT image with 234×176×501 voxels. Two targets with a diameter of 1.4 mm and a length of 20 mm were added in the 3D CT phantom. The intensity of targets is 0.99, which is 1% less than the intensity of the edges of the ellipse. This is because the tumor with CT contrast agent injection has contrast as high as bones in CT images [55]. Like the first simulation, we added 15% Gaussian noise to numerical CT images.

Numerical simulation using MRI images of a rat brain

The ultimate goal of the proposed kernel method is to apply it in anatomical images (such as CT or MRI) guided FMT for small animal studies. To validate the feasibility of the proposed method using *in vivo* anatomical guidance with heterogeneous structures, we used MRI images of a rat brain as the anatomical guidance. MRI imaging was performed with a Bruker Biospec 7 Tesla (7T) small-animal scanner (Bruker BioSpin MRI, Ettlingen, Germany). A 72 mm internal diameter linear resonator was used for radio frequency (RF) transmission and a four-channel rat brain phased array surface coil was used for signal reception. The rat brains were imaged coronally with a fast-spin echo sequence (RARE; axial: TE/TR = 8 ms/750 ms; FOV = 40 × 40 mm^2; MTX = 256 × 256; ST/SI = 1 mm/1 mm; ETL = 4). Data were acquired and reconstructed using ParaVision 5.1 software (Bruker BioSpin MRI). Experiment was conducted under a protocol approved by the University of California, Davis, Animal Use and Care Committee (Davis, CA). A male athymic nude rat, purchased from Harlan Laboratories (Hayward, CA) was inoculated with 3 × $10mm^6$ U87 MG cells/10 μ L intracranially. The rat was administered 0.5 mmol/kg of the small molecule gadolinium chelate, gadoteridol (Bracco Imaging) via bolus i.v. injection prior to T1w imaging.

From the MRI images, We used the open-source software *iso2mesh* to generated

a 3D finite element mesh with 181,686 tetrahedral elements, and 41,427 nodes[187]. We segmented the tumor in the MRI images as the FMT target region for simulate FMT measurement. Similar to the numerical phantom studies, numerical FMT measurement data was generated by Eq. (4.3) with a line pattern laser projected on the rat brain surface. We used 30 excitation positions of the line laser to cover the whole rat brain surface[186]. For each line laser excitation, the 20,055 surface nodes were used as the measurement detectors. The tissue optical properties were set to μ_a= 0.012 mm^{-1} and μ_s'= 0.83 mm^{-1} at both the excitation wavelength (650 nm) and the emission wavelength (700 nm). We assigned the fluorophore concentration to be 1 in the target regions and 0 in the background regions. Like other simulation studies, we added 30% Gaussian noise to the simulated FMT measurement data. In the kernel, we can extract the feature vectors easily from the MRI images because the FE mesh is generated from the same image, so they are already co-registered. Then, we generated the kernel matrix using the Eq. (4.8) and (4.9) to incorporate anatomical information into the FMT image reconstruction by minimizing the kernelized objective function (4.13).

During the kernel method FMT reconstruction, we used the MRI images without segmentation as the anatomical guidance to generate the $\boldsymbol{K}$ matrix. For the soft prior method, we used segmented images to generate the soft prior matrix without adding any segmentation error.

The voxel number for each corresponding node and the number of nearest neighbors in *knnsearch* are important parameters in constructing kernel matrix $\boldsymbol{K}$ and have significant effects on the kernel reconstruction method. In this paper we studied 3 different voxel numbers, 3×3×3, 5×5×5, and 7×7×7. The lengths of feature vectors were 27, 125, and 343 respectively. for *knnsearch*, different values of k(16, 32, 64, 128, 256), the number of nearest neighbors, were also studied.

4.2.5 Phantom experimental setup

To validate our algorithm, we conducted an agar phantom experiment. In this experiment, we used a cylindrical phantom with a diameter of 22 mm and a length of 80 mm. The phantom was composed of 1% intralipid, 2% agar, 20 μM bovine

hemoglobin (H2625, Sigma-Aldrich Inc., St. Louis, MO) and water. We embedded two capillary tubes with a length of 20 mm and a diameter of 1.4 mm as targets, in which 20 μM Sulfo-Cyanine5 dye (Lumiprobe Corporation, Hallandale Beach, FL) was injected. The geometry of the experimental phantom is shown in Figs. 4.2b, where the two red bars indicate two FMT targets. The edge-to-edge distance of the two targets was 2.94 mm.

The phantom geometry was discretized with a 3D tetrahedral finite element mesh with 37,333 nodes and 199,881 elements. During the FMT imaging, a line laser (1 mm wide and 50 mm long) at the wavelength of 643 nm scanned the surface of the phantom sequentially with 30 excitation positions that were distributed uniformly on the phantom surface. For each line laser excitation position, an emission picture at the wavelength of 720 nm was taken. All 9,384 surface nodes on the side surface of cylinder were used as the detector nodes and the measurements were obtained from acquired emission pictures. Details of the conical mirror based FMT imaging system were described in Ref. [188]. The phantom optical properties were $\mu_a = 0.012$ mm^{-1} , $\mu_s' = 0.83$ mm^{-1} at both 643 nm and 720 nm wavelengths.

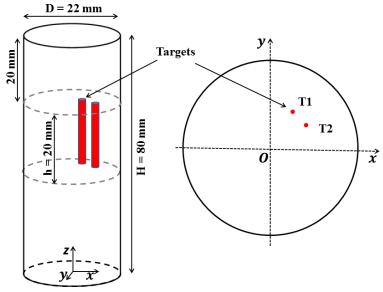

Figure 4.2: The geometry of the phantom experiment with target locations at T1 (1.72, 4.71) and T2 (5.01, 1.87).

The 3D CT images of the phantom with an isotropic voxel size of 0.15 mm were obtained with our lab-made micro-CT imaging system with 180 projections[189]. The micro-CT system consists of an x-ray source and a flat panel detector placed opposite to each other on a micro-CT gantry that rotates around the bed where the phantom was placed. The source-to-isocenter distance is 205.34 mm and the source-to-detector distance is 246.2 mm. The detector has a 49.2 mm by 49.2 mm

sensing area consists of a 1,024 by 1,024 pixel sensor with 48 µm pixel spacing. The X-ray tube was operated at a current of 0.5 mA and the voltage of 50 kVp. A filtered backprojection algorithm was used to reconstruct the micro-CT images with a Shepp-Logan filter. The obtained CT images are shown in Fig. 4.9(a), from which we calculated each targets' size and position. Because Sulfo-Cyanine5 dye does not have CT contrast, only the capillary tubes were observed in the reconstructed microCT images and the fluorescence dye (target) regions were filled by pixels having the same CT contrast as the capillary tubes as guidance in the kernel method.

4.2.6 FMT image evaluation criteria

According to our previous studies, the combinations of 4 metrics listed below can evaluate the quality of the reconstructed FMT images very well. Their detailed definitions can be found in Refs. [44, 143]. Briefly, The Volume Ratio (VR) measures the ratio between the true region of interest (ROI) and the reconstructed region of interest (rROI). The Dice similarity coefficient (Dice) measures the location accuracy of the reconstructed target. Ideally, VR and Dice coefficients should be 1. The Contrast-to-Noise Ratio (CNR) measures how well the reconstructed target is distinguished from its background. The higher the CNR coefficient is, the better the reconstructed image. The Mean Square Error (MSE) is the difference between the measurements and the model predictions. The MSE closer to zero is better.

4.3 Results

4.3.1 Simulation Results

Cylindrical phantom simulation with two FMT targets

In this simulation, we had two capillary tube targets embedded inside the cylindrical background phantom with an edge-to-edge distance of 2 mm as described in Fig. 4.1(a). For comparison, we have reconstructed FMT images with soft prior

method. The ground truth FMT images, simulated CT images, and the reconstructed FMT images with the soft prior method are plotted in Fig. 4.3. All the FMT reconstructions in this paper were conducted in 3D and results are shown by slices along the z-axis with equal distance. Then, we performed the reconstruction with the proposed kernel based FMT reconstruction algorithm. To investigate how the parameters in the kernel method affect the FMT reconstruction, we studied 3 different voxel numbers (3×3×3, 5×5×5,and 7×7×7) and 3 different nearest neighbors (k =16, 32, 64) with 9 combinations of the kernel based FMT reconstructions. The reconstructed FMT images are plotted in Fig. 4.4, in which each column indicates different voxel numbers and each row indicates different numbers of nearest neighbors. For all 9 cases, the two targets have been reconstructed and separated successfully as indicated by Fig. 4.4.

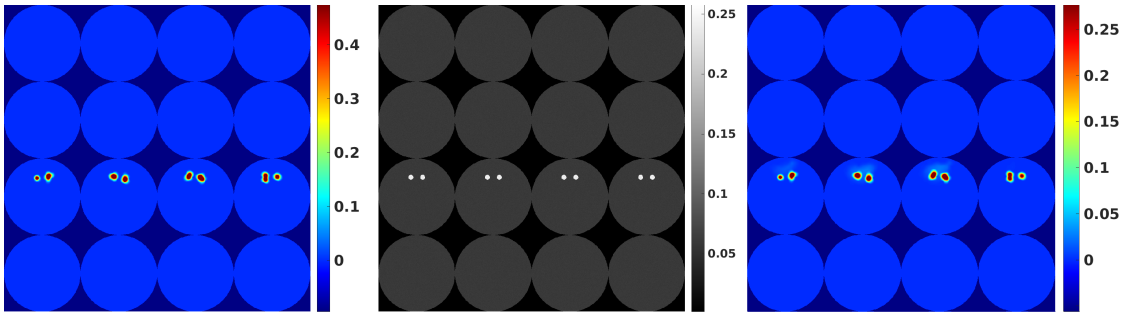

Figure 4.3: For the numerical simulation of two targets: (a) the ground truth image, (b) simulated anatomical guidance images, and (c)the reconstructed FMT image with soft prior method.

To evaluate the simulation results quantitatively, we calculated quantitative image quality metrics such as VR , Dice, CNR, and MSE for the FMT reconstruction with the soft prior method, and the 9 FMT reconstructions with kernel method, as shown in Table 4.1. For the kernel method, when the voxel number is fixed, we have better FMT reconstruction quality as the nearest neighbor k increases. For example, the Dice coefficient increased from 0.002 to 0.023 as k increased from 16 to 64 for the voxel number of 3×3×3. Similarly, for the fixed nearest neighbor k, we found that the FMT image quality becomes better with larger voxel numbers. The best FMT reconstruction result was obtained with $k = 64$ with 7×7×7

voxel size, which is highlighted in Table 4.1. From Table 4.1, we see that the soft prior method performed better than the kernel method in this simulation when the target regions were known accurately in the anatomical guidance.

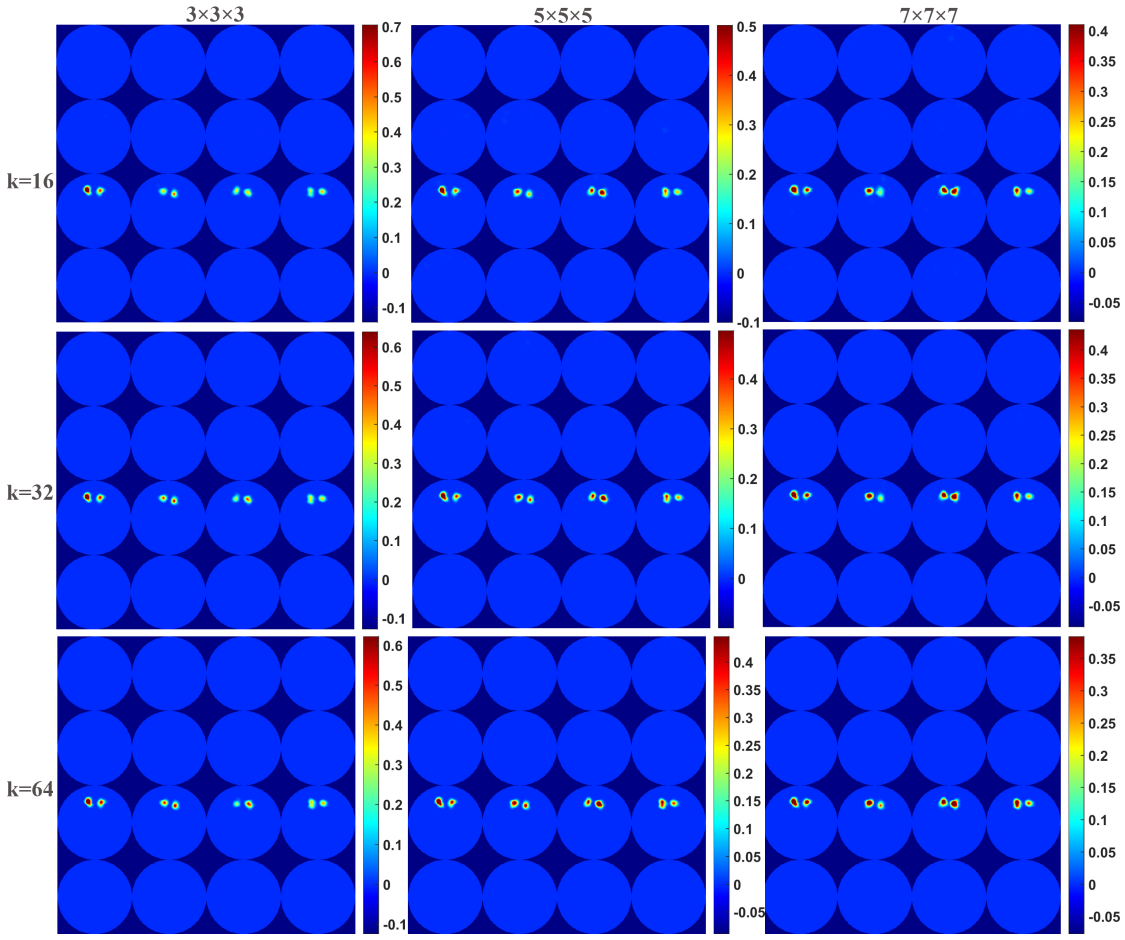

Figure 4.4: Reconstruction FMT images for the cylindrical phantom simulation of 2 targets by the kernel method with different nearest neighbor k as indicated by each row and different voxel numbers indicated by each column.

Elliptic cylindrical phantom simulation with two FMT targets

In this simulation, we had two capillary tube targets embedded inside the elliptic cylindrical background phantom with an edge-to-edge distance of 1 mm as described in Fig. 4.1(b). For comparison, we have also reconstructed FMT images with the soft prior method. The ground truth FMT images, simulate CT

Table 4.1: For the cylindrical phantom simulation of 2 targets, the calculated VR, Dice, CNR and MSE with kernel method for different numbers of nearest neighbor k and different voxel numbers, and soft prior method.

k	Voxel number	VR	Dice	CNR	MSE
16	3×3×3	0.124	0.002	18.264	3.88e-4
16	5×5×5	0.223	0.159	21.351	2.96e-4
16	7×7×7	0.387	0.306	19.554	3.44e-4
32	3×3×3	0.127	0.006	19.688	3.41e-4
32	5×5×5	0.243	0.187	22.713	2.51e-4
32	7×7×7	0.451	0.430	22.099	2.66e-4
64	3×3×3	0.139	0.023	20.029	3.29e-4
64	5×5×5	0.347	0.323	23.956	2.22e-4
64	7×7×7	**0.639**	**0.596**	**24.111**	**2.21e-4**
	Soft Prior	0.952	0.964	32.355	1.67-e4

images, and the reconstructed FMT images with the soft prior method are plotted in Fig. 4.5. Then, we performed the reconstruction with the proposed kernel based FMT reconstruction algorithm. To investigate how the parameters in the kernel method affect the FMT reconstruction, we studied 3 different voxel numbers (3×3×3, 5×5×5,and 7×7×7) and 3 different nearest neighbors (k = 64, 128, 256) with 9 combinations of the kernel based FMT reconstructions. The reconstructed FMT images with the kernel method are plotted in Fig. 4.6, in which each column indicates different voxel numbers and each row indicates different numbers of nearest neighbors. For all 9 cases, the two targets have been reconstructed and separated successfully as indicated by Fig. 4.6.

To evaluate the simulation results quantitatively, we calculated quantitative image quality metrics for the FMT reconstruction with the soft prior method and the kernel method with 9 combinations, as shown in Table 4.2. From the Table 4.2, when the voxel number is fixed, we have better FMT reconstruction image quality as the nearest neighbor k increases. One example is that the Dice

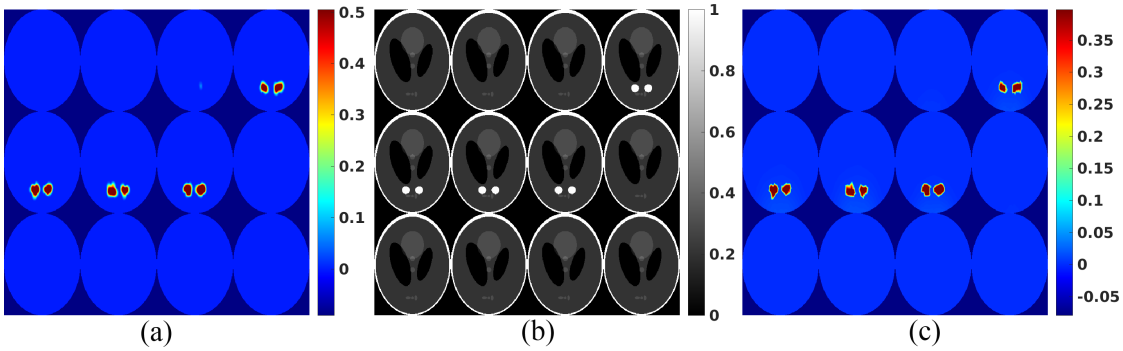

Figure 4.5: For the cylindrical phantom simulation of two FMT targets, (a) the ground truth image and (b) simulated CT images, and (c) the reconstructed FMT image with the soft prior method.

increase from 0.469 to 0.803 as k increase from 64 to 256 for the voxel number of 3×3×3. Similarly, for the fixed nearest neighbor k, we found that the FMT image quality becomes better with larger voxel number in this simulation setup up. The best FMT reconstruction result was obtained with $k = 256$ with 7×7×7 voxel size, which is highlighted in Table 4.2.

Numerical simulation with false target size in the numerical anatomical CT image

The numerical phantom geometry of this simulation study same as the second simulation plotted in Fig. 4.1b. However, the diameter of the right target in the simulated anatomical guidance CT images (Fig. 4.7b) was enlarged intentionally from 1.4 mm to 2.8 mm to study how the false target size affects the FMT reconstruction with the proposed kernel method. The enlarged target was moved to the right 0.7 mm so that the edge-to-edge distance of the two targets was still 1 mm in the simulated CT images as shown in Fig. 4.7(b). For comparison, we have performed the reconstruction with the soft prior method and with the kernel method of 3 different nearest neighbors k and 3 different voxel numbers as in the above section. Among all the reconstructions with the kernel method, unlike the previous simulation, we found that the reconstruction with the nearest neighbor of k=256 and the voxel number of 3×3×3 had the least error with a MSE

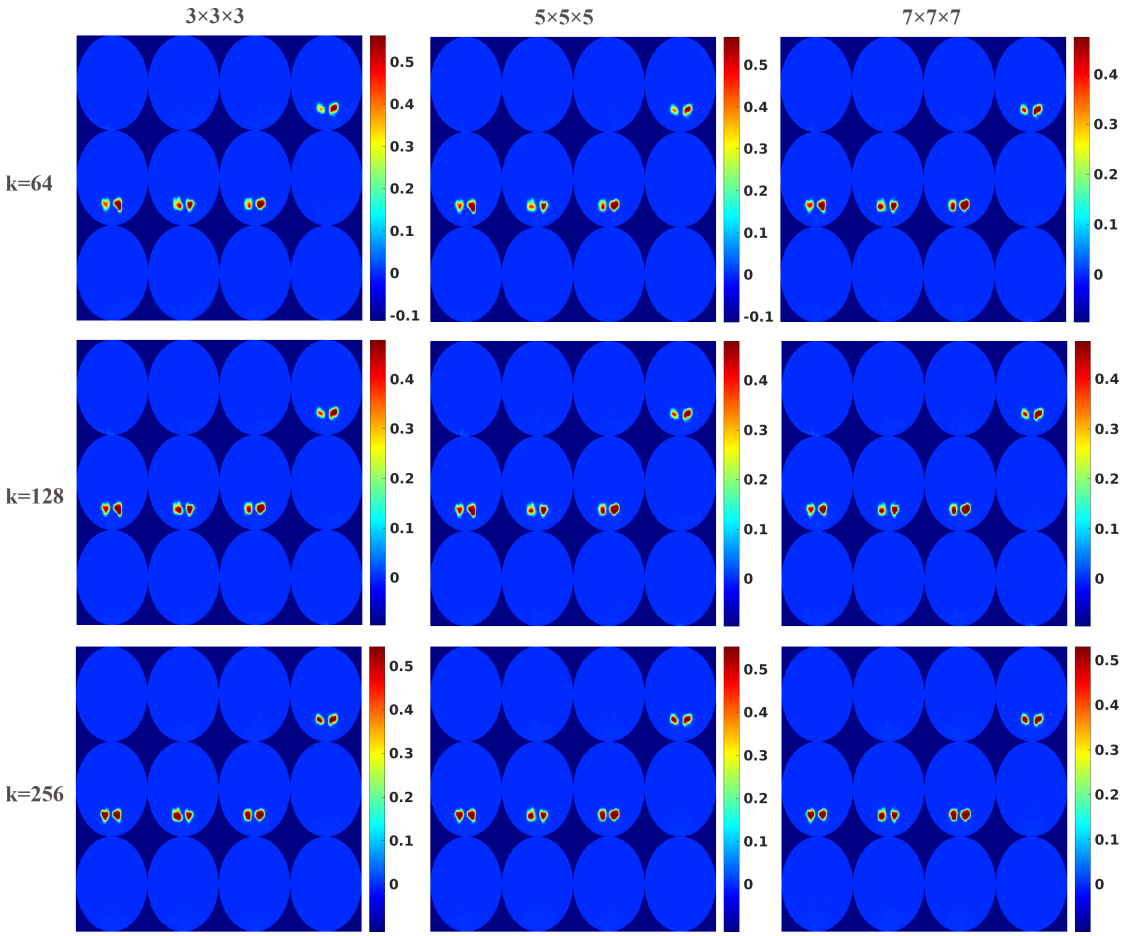

Figure 4.6: Reconstruction FMT images for the elliptic cylindrical phantom simulation with 2 FMT targets by the kernel method with different nearest neighbor k as indicated by each row and different voxel numbers indicated by each column.

of 8.54e-4, whereas the soft prior method had MSE of 1.31e-3. Fig. 4.7 plots the ground truth image (Fig. 4.7a), the reconstructed FMT image with the soft prior method (Fig. 4.7c), and the reconstructed FMT image by the kernel method with the nearest neighbor of $k = 256$ and the voxel number of 3×3×3 (Fig.4.7d). As indicated in Fig.4.7c, the two targets were barely separated with the soft prior method. Fig.4.7d is a representative reconstructed FMT image with the kernel method and indicates that the image quality is much better than that of Fig. 4.7c as demonstrated by the CNR of 12.214 for Fig. 4.7c and 17.543 for Fib. 4.7d. The calculated image quality metrics are listed in Table 4.3.

Table 4.2: For the numerical simulation of elliptic cylindrical phantom with 2 FMT targets, the calculated VR, Dice, CNR and MSE with kernel method for different numbers of nearest neighbor k and different voxel numbers, and with the soft prior method.

k	Voxel number	VR	Dice	CNR	MSE
64	3×3×3	0.366	0.469	18.971	6.22e-4
64	5×5×5	0.318	0.419	19.452	6.16e-4
64	7×7×7	0.519	0.635	22.262	4.82e-4
128	3×3×3	0.516	0.604	20.811	5.16e-4
128	5×5×5	0.481	0.590	21.113	5.39e-4
128	7×7×7	0.519	0.653	23.072	4.57e-4
256	3×3×3	0.713	0.803	25.028	1.35e-4
256	5×5×5	0.668	0.782	25.286	1.46e-4
256	7×7×7	**0.757**	**0.845**	**26.108**	**1.21e-4**
	Soft Prior	1.046	0.934	26.661	1.73e-4

Table 4.3: For the numerical simulation with a false target size, the calculated VR, Dice, CNR and MSE with kernel method of different numbers of nearest neighbor $k = 256$ and different voxel numbers, and soft prior method.

k	Voxel number	VR	Dice	CNR	MSE
256	3×3×3	**0.394**	**0.548**	**17.543**	**8.54e-4**
256	5×5×5	0.281	0.416	16.816	8.91e-4
256	7×7×7	0.409	0.537	16.728	9.06e-4
	Soft Prior	0.466	0.527	12.214	1.31e-3

Numerical simulation using MRI images of a rat brain

To validate the proposed kernel based FMT image reconstruction algorithm with guidance from realistic anatomical images, we conducted simulation study using *in vivo* rat brain MRI images as shown in Fig. 4.8(a). Details of the MRI images and simulation setup described in Section. 4.2.4. The contrast of tumor to

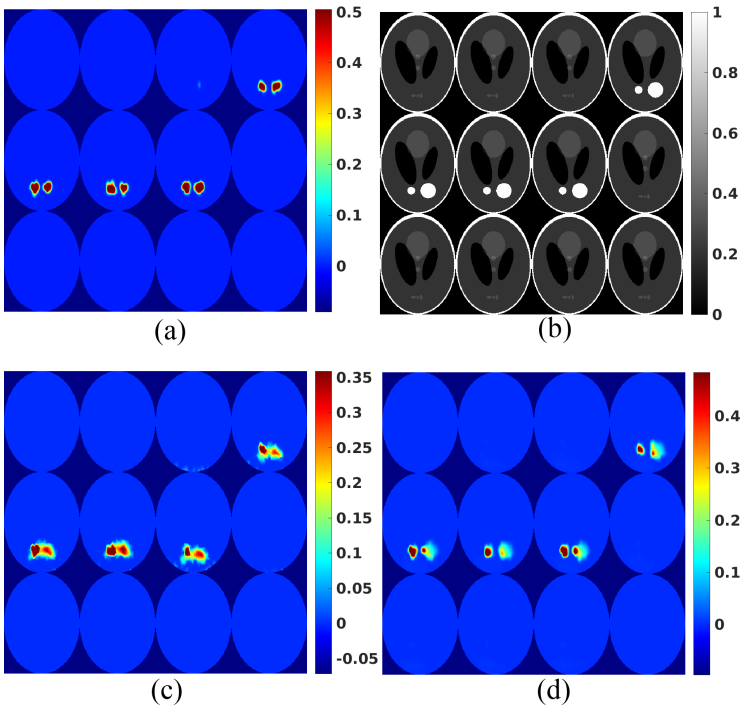

Figure 4.7: For numerical simulation with false larger target size, (a) the ground truth image, (b) simulated CT imges with falsy enlarged target. (c) the reconstructed FMT image with soft prior method, and (d) the reconstructed FMT image by the kernel method with the nearest neighbor of $k = 256$ and the voxel number of 3×3×3.

the background surrounding it is approximately 1:2. First, we reconstructed the FMT image using the soft prior method, in which only two regions considered. We have obtained very good FMT results from the soft prior method as shown in Fig. 4.8(b). Fig. 4.8(c) is the reconstructed FMT image obtained by the kernel method when using the MRI images as the anatomical guidance directly without segmentation. In the kernel method, we set the nearest neighbor of $k = 256$ and the voxel number of 3×3×3. From Fig. 4.8 we can see that the kernel method reconstructed the target very well with comparable results from the soft prior method. For the kernel method VR, Dice, CNR, and MSE are 0.529, 0.626, 23.007, and 7.14e-4, while for the soft prior method those metrics are 0.966, 0.974 , 42.622 and 3.12e-4, respectively.

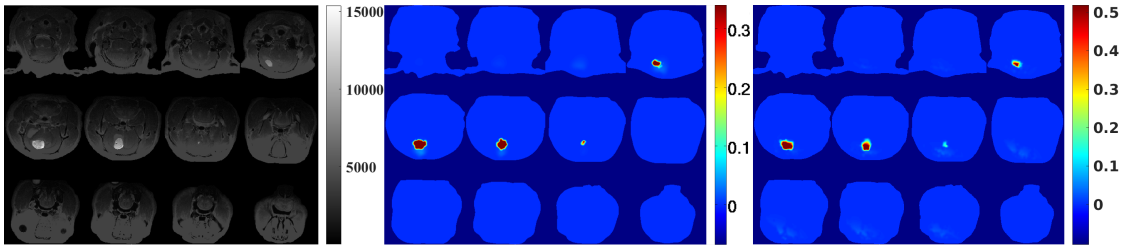

(a) (b) (c)

Figure 4.8: For numerical simulation with rat head MR image (a)MRI image, FMT reconstructed image with (b) soft prior method (c) kernel method with $k = 256$ and the voxel number of 3×3×3.

4.3.2 Phantom experimental results

Reconstruction with homogeneous background in CT images

The phantom's geometry is plotted in Fig. 4.2. As described in the numerical simulation section, we have performed the FMT reconstruction of this phantom experiment with the soft prior method and with kernel method of 15 different case with 5 different nearest neighbor k (16, 32, 64, 128, 256) and 3 different voxel numbers (3×3×3, 5×5×5, 7×7×7).The reconstructed FMT images along with anatomical CT images are plotted in Fig. 4.9. The kernel based reconstruction results (Fig. 4.9(d)) are as good as the results from the soft prior method (Fig. 4.9(c)) when the homogeneous anatomical images were used as guidance. For comparison, we have also reconstructed the target without anatomical guidance as shown in Fig. 4.9(b), from which we see that the two targets were reconstructed with large position errors. To analyze the reconstructed FMT images quantitatively, we have calculated the VR, Dice, and CNR as listed in Table 4.4 for each case, where the microCT images were referred as the ground truth image to calculate those metrics. The MSE has not been calculated because we do not know the exact fluorescent dye concentration. From Table 4.4, we know that the kernel method has the best reconstruction results with the nearest neighbor of 64 and the voxel number of 5×5×5, in which the VR, Dice and CNR are 0.714, 0.643, and 25.849, respectively. The VR, Dice, and CNR are 0.729, 0.757 and 30.312 for the FMT reconstruction with the soft prior method. These similar image quality metrics in-

dicate that the kernel method is as good as the soft prior method for FMT targets with homogeneous background.

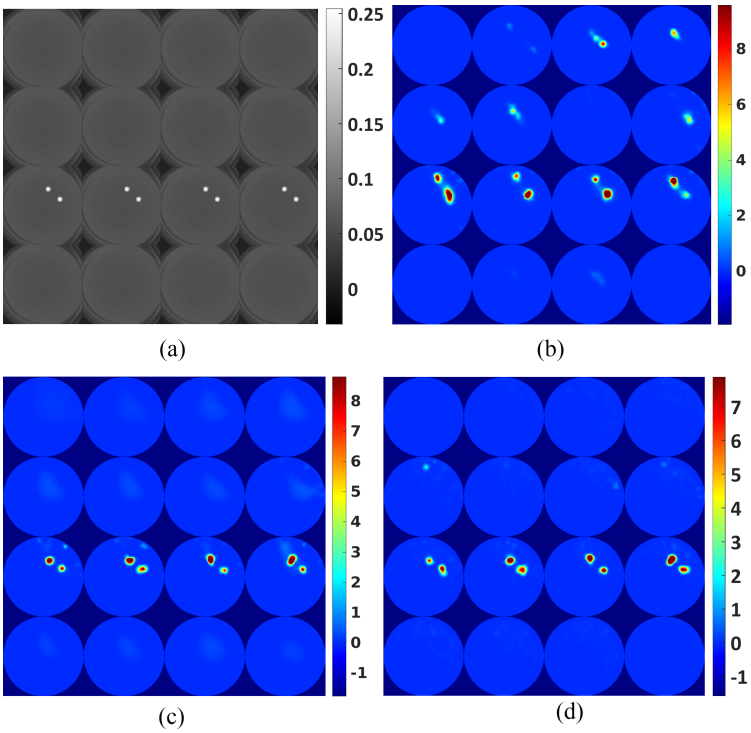

Figure 4.9: (a)Original CT images, FMT reconstruction result (b)without prior (c) with soft prior method homogenous background (d) with kernel method reconstruction using original CT images as guidance with $k = 64$ and the voxel number of 5×5×5.

Reconstruction with inhomogeneous background in CT images

To further validate the proposed method in a more complicated anatomical images, we added some artificial features in the physical CT images we obtained. As shown in Fig. 4.10(a), the darkest big cylinder has an intensity of less than 50% of the background. The other two big cylinders have an intensity of 50% more than the background intensity. We also added another three small cylinders at the random locations with a different intensities. Two of them had intensity of 5 times more than the background, which is slightly higher than the targets' intensity. This mimics bones in CT images or fat and bloods in MRI images.

Table 4.4: The calculated VR, Dice, and CNR for the phantom experiments with the soft prior and the kernel method.

	Homogeneous			Inhomogeneous		
	VR	**Dice**	**CNR**	**VR**	**Dice**	**CNR**
Soft prior	0.729	0.757	30.312	0.677	0.728	29.704
Kernel method	0.714	0.643	25.849	0.672	0.648	28.250
No prior	0.752	0.025	2.569			

For the reconstruction with the soft prior method we had 6 regions: two targets, three big cylinder artificial features, and the background. Unlike the homogeneous background case, here we obtained the best kernel method based FMT images with the nearest neighbor of 256 and the voxel number of 3×3×3, in which the VR, Dice and CNR are 0.672, 0.648, and 28.250, respectively. Those image quality metrics are slightly lower than those of the soft prior method: 0.677, 0.728, and 29.704 respectively. These results demonstrated that the kernel method is able to achieve comparable results to the soft prior method when there are inhomogeneous inclusions in the anatomical guidance images.

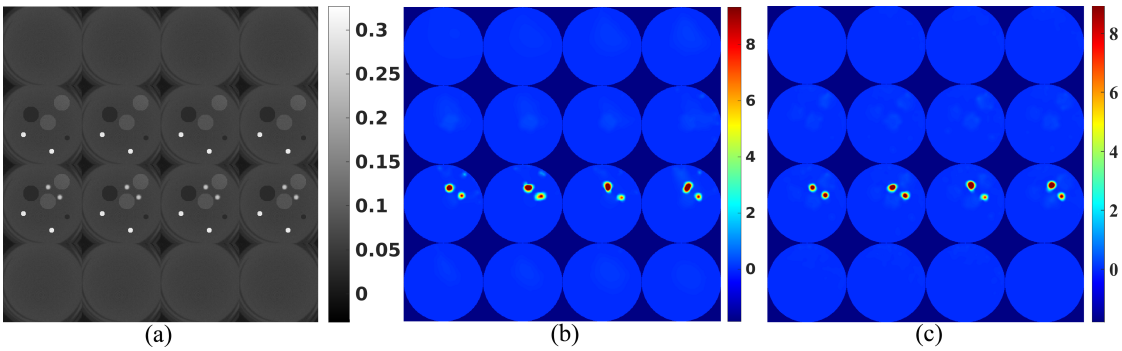

Figure 4.10: (a) CT image with artificial features (b) FMT reconstruction result with soft prior method inhomogenous background (c) kernel method reconstruction using CT image with artificial features as guidance with $k = 256$ and the voxel number of 3×3×3.

4.4 Discussions and Conclusion

In this paper, we have introduced the kernel method as a new approach to include the anatomical guidance in the FMT image reconstruction, in which a kernel matrix having the anatomical priors is created and incorporated into the projection model of FMT. It is worth noting that we used the forward model without the kernel method to generate the FMT measurements for numerical simulations. Numerical simulations and phantom experiments have been performed to demonstrate that the proposed kernel method has reconstructed the FMT targets successfully and have comparable results as the soft prior method.

Compared with conventional Laplacian-type regularization method to include anatomical priors such as soft priors, the kernel method has the advantage of easy implementation, in which we do not need to segment the target and background regions in the anatomical images. This advantage is more significant for some cases in which the targets are not easily differentiated and segmented. This may result in a concern of the misguidance from the false positive regions. To address this issue, we have performed two numerical simulations, one with false target size (from 1.4 mm to 2.8 mm in diameters) as described in section 4.3.1. Our results indicate the false target size guidance has some effects when two targets are very close. However, the kernel method performs better than the soft prior method. Another advantage of the kernel method is that we do not have to search for optimum regularization parameter, which is searched with the L-curve method in conventional regularization methods.

To generate the kernel matrix, three parameters must be set before the FMT image reconstruction. The first parameter is the Gaussian kernel coefficient σ. According to previous studies [138, 185], $\sigma = 1$ yields best results. The second parameter is the number of nearest neighbors k. From the results of both numerical simulations and phantom experiments, we found that the reconstructed image quality is better with a larger number of k. It also depends on the features of anatomical images.As indicated in numerical simulations with cylindrical geometry and phantom experiment with homogeneous background, for anatomical images with fewer features, we can obtain good reconstruction results considering

only 64 nearest neighbors in the kernel matrix. However, for the anatomical images with rich features, such as elliptic cylindrical simulation, the simulation with MRI data and phantom experiment with inhomogeneous background, we have to consider more nearest neighbors in the kernel matrix. We acknowledge that for the simulations and experiments presented the results of kernel method with up to k=64, we can obtain much better reconstruction results with k=256.The third parameter is the voxel number. As demonstrated in the first and second simulations, of anatomical images without any false information, the quality of reconstructed FMT images increase slightly as the voxel number increases for a fixed number of nearest neighbors k. However, for the numerical simulations with the false target size in anatomical images, kernel method with the smaller number of voxels performs better than the kernel method with the larger number of voxels. As it shown in Table 4.3, Dice and CNR are achieved highest with voxel number of 3×3×3 for the reconstruction with kernel method when k=256. MSE also reached the lowest for the case of voxel number 3×3×3. VR coefficient is not informative in the case because the incorrect bigger size of the target in the anatomical images introduce higher volume ratio to the reconstruction image. Similarly, Numerical simulation with MR images and phantom experiment with artificial features further demonstrate this trend by obtaining the best results with of voxel number of 3×3×3.

The kernel matrix was generated before the FMT reconstruction with the matrix generation times depending on the voxel size and the nearest neighbor number. Table 4.5 lists the $\boldsymbol{K}$ matrix generation time for elliptic cylindrical simulation with two targets. For the best image quality setup with the nearest neighbor of 256 and the voxel number of 3×3×3, the $\boldsymbol{K}$ matrix generation time was 20.09 seconds on a cluster with 12 nodes (2.8 GHz each node) and 128 GB memory. This is slightly longer than the time spent on the generating regularization matrix for the soft prior method, which was 12.28 seconds in this simulation with 5 regions. We acknowledge that, the time spent on generating the soft prior matrix refers to the time for generating matrix L from the region labeled vector. Since kernel matrices are are sparse, multiplications involved in reconstruction processes also do not

introduce significant computation time. In this study, the kernel method based FMT reconstruction converged in no more than 10 iterations which are around 5 seconds total.

Table 4.5: Construction time of the kernel matrix K with different k values and voxel sizes (in seconds).

Voxel number	$\boldsymbol{k = 16}$	$\boldsymbol{k = 32}$	$\boldsymbol{k = 64}$	$\boldsymbol{k = 128}$	$\boldsymbol{k = 256}$
3×3×3	3.36	3.78	5.46	8.88	**20.09**
5×5×5	11.32	12.78	16.81	23.58	38.79
7×7×7	28.89	34.59	43.05	57.30	96.42

In summary, we have introduced a kernel method based FMT reconstruction algorithm as a new approach to include the anatomical guidance. Numerical simulations prove that this method is robust in overcoming incorrect anatomical guidance. Phantom experiments further validate that the proposed method can improve the FMT reconstruction quality and does not increase the reconstruction time. In the future, we will apply the proposed kernel method to *in vivo* experiments on the hybrid systems.

Chapter 5

Conclusion and future work

In this present work, feasibility of CT guided DOT for breast cancer imaging has been studied. A non-contact CCD camera based prototype system was built and numerical simulations and phantom experiments were conducted. Numerical simulations indicated that the measurement data from six projections with a 6 cm wide measurement patch are enough to reconstruct a good absorption contrast image with high quantitative accuracy if CT guidance is applied. From phantom experiments, we see that our proposed CT guided DOT system is able to reconstruct 2 times absorption contrast targets with very high spatial resolution and quantitative accuracy.

Image segmentation, a tedious precess, is required for soft prior based anatomical guidance method. to remove this requirement, kernel-based image reconstruction algorithm was introduced to directly incorporating anatomical images into the DOT image reconstruction. We conducted numerical simulation and phantom experiments to validate the new algorithm. Simulation and phantom experiment results have validated the kernel method. Our results indicate that the higher number of nearest neighbors and larger voxel size improve the quality of the reconstructed images. The numerical simulation results indicate that the proposed kernel method is robust to CT contrast and the false positive targets in the anatomical guidance such as CT images. After applying the new method With the clinical breast CT images as the guidance, we demonstrated that we do not need the segmentation for the proposed kernel method.

We have also implemented kernel-based image reconstruction algorithm for anatomical image guided FMT. Numerical simulations and phantom experiments have been performed to demonstrate that the kernel method has reconstructed the FMT targets successfully and have comparable results as the soft prior method. Numerical simulations prove that this method is robust in overcoming incorrect anatomical guidance. Phantom experiments further validate that the proposed method can improve the FMT reconstruction quality and does not increase the reconstruction time.

In the future, we will build a multispectral EMCCD camera based DOT imaging system which consists of 4 diode CW lasers, an optical switch, a fiber holder, collimators, an EMCCD camera and a rotation stage. Four CW lasers at wavelengths of 650, 715, 880, and 915 nm will be connected to a 4-to-12 optical switch which passes one laser to one of 12 fibers and the laser beam will be collimated at the other end of the fiber with a collimator. Measurements at six projections with rotational increments of 60 degrees will be taken to cover the whole surface of the breast. Altogether, there will be 4 lasers with a total 72 excitation positions for each wavelength. For each laser excitation position, pictures will be taken by the EMCCD camera as measurements in a transmission mode. The EMCCD camera based DOT imaging system will be integrated into a breast CT imaging system. The rotation time per 60 degrees is estimated to be 5 seconds. The exposure time per measurement picture is estimated to be 1 second per wavelength and position. Therefore, the total measurement time for the DOT imaging is estimated at about 8 minutes.

The integrated CT-guided DOT system will allow us to use breast CT images directly to guide DOT image reconstruction applying the proposed kernel method. The multispectral aspect of the CT-guided DOT system will make it possible to monitor changes in hemoglobin concentrations and oxygenation. Further more, since we will have more measurement data, we can possible reconstruct reduced scattering coefficients along with optical absorption coefficients. The morphological imaging, including the scattering particle mean diameter imaging and the scattering particle volume fraction imaging can obtained from the reduced scattering

images at multiple wavelengths.

Regarding the image reconstruction algorithm, new version of kernel method, the highly-constrained back-projection (HYPR) method has been introduced into the dynamic PET image and it has been demonstrated that HYPR method is simpler to be implemented and can further improve the kernel-based dynamic PET image reconstruction[190]. In the future, HYPR kernel method can be introduced in the image reconstruction of DOT and FMT to improve the reconstructed images quality.

Furthermore, we can also employ deep convolutional neural network (CNN) to improve DOT and FMT image reconstructions. We can build a CNN which can be trained with data which obtained from higher number of projections, possibly 24 or 36 projections, then be used to improve the quality of reconstructed images from only 4 or 6 projections data. Similar methods proven to be efficient in low-dose CT image reconstruction[191]. Directly employing the method must be challenging since image reconstruction in DOT is nonlinear and requires computing a huge Jacobian matrix. However, following the advancements in linearizing techniques and rapidly increasing computation power, it is possible to introduce deep learning techniques into DOT and FMT image reconstruction in the coming years.

Bibliography

[1] G Jarry, S Ghesquiere, JM Maarek, F Fraysse, S Debray, D Laurent, et al. Imaging mammalian tissues and organs using laser collimated transillumination. *J. Biomed. Eng.*, 6(1):70–74, 1984.

[2] Jeremy C Hebden and KS Wong. Time-resolved optical tomography. *Appl. Opt.*, 32(4):372–380, 1993.

[3] Simon R Arridge and Jeremy C Hebden. Optical imaging in medicine: II. Modelling and reconstruction. *Phys. Med. Biol.*, 42(5):841–853, 1997. [doi:10.1088/0031-9155/42/5/008].

[4] Andrew M Smith, Michael C Mancini, and Shuming Nie. Second window for in vivo imaging. *Nat. Nanotechnol.*, 4(11):710, 2009.

[5] JC Hebden and DT Delpy. Diagnostic imaging with light. *Br. J. Radiol.*, 70(Special-Issue-1):S206–S214, 1997.

[6] Lihong V Wang. Prospects of photoacoustic tomography. *Med. phys.*, 35(12):5758–5767, 2008.

[7] Venkata Radhakrishna Kondepati, H Michael Heise, and Juergen Backhaus. Recent applications of near-infrared spectroscopy in cancer diagnosis and therapy. *Anal. Bioanal. Chem.*, 390(1):125, 2008.

[8] C Li, SR Grobmyer, N Massol, X Liang, Q Zhang, L Chen, LL Fajardo, and H Jiang. Noninvasive *in vivo* tomographic optical imaging of cellular morphology in the breast: possible convergence of microscopic pathology and macroscopic radiology. *Med. Phys.*, 35(6):2493–2501, 2008. [doi:10.1118/1.2921129].

[9] Lihong V Wang and Hsin-i Wu. *Biomedical optics: principles and imaging*. John Wiley & Sons, 2012.

[10] L Wang, PP Ho, et al. Ballistic 2-d imaging through scattering walls using an ultrafast optical kerr gate. *Science*, 253(5021):769, 1991.

[11] David Huang, Eric A Swanson, Charles P Lin, Joel S Schuman, William G Stinson, Warren Chang, Michael R Hee, Thomas Flotte, Kenton Gregory, Carmen A Puliafito, et al. Optical coherence tomography. *Science (New York, NY)*, 254(5035):1178, 1991.

[12] Christoph Haisch. Optical tomography. *Annu. Rev. Anal. Chem.*, 5:57–77, 2012.

[13] Wolfgang Drexler and James G Fujimoto. *Optical coherence tomography: technology and applications*. Springer Science & Business Media, 2008.

[14] David A Boas, Dana H Brooks, Eric L Miller, Charles A DiMarzio, Misha Kilmer, Richard J Gaudette, and Quan Zhang. Imaging the body with diffuse optical tomography. *IEEE Signal Process. Mag.*, 18(6):57–75, 2001. [doi:10.1109/79.962278].

[15] Jing Bai and Zhun Xu. Fluorescence molecular tomography. In *Molecular Imaging*, pages 185–216. Springer, 2013.

[16] Gang Yao and Lihong V Wang. Theoretical and experimental studies of ultrasound-modulated optical tomography in biological tissue. *Appl. Opt.*, 39(4):659–664, 2000.

[17] Guillem Pratx, Colin M Carpenter, Conroy Sun, and Lei Xing. X-ray luminescence computed tomography via selective excitation: a feasibility study. *IEEE Trans. Med. Imag.*, 29(12):1992–1999, 2010.

[18] Changqing Li, Kun Di, Julien Bec, and Simon R Cherry. X-ray luminescence optical tomography imaging: experimental studies. *Opt. Lett.*, 38(13):2339–2341, 2013.

[19] Wei Zhang, Dianwen Zhu, Michael Lun, and Changqing Li. Multiple pinhole collimator based x-ray luminescence computed tomography. *Biomed. Opt. Express*, 7(7):2506–2523, 2016.

[20] Changqing Li, Arnulfo Martínez-Dávalos, and Simon R Cherry. Numerical simulation of x-ray luminescence optical tomography for small-animal imaging. *J. Biomed. Opt.*, 19(4):046002–046002, 2014.

[21] Wei Zhang and Changqing Li. Collimated superfine x-ray beam based x-ray luminescence computed tomography. *J. Xray. Sci. Technol.*, page (In Press.). [doi:10.3233/XST-17265].

[22] Michael C Lun, Wei Zhang, and Changqing Li. Sensitivity study of x-ray luminescence computed tomography. *Appl. Opt.*, 56(11):3010–3019, 2017.

[23] Akira Ishimaru. *Wave propagation and scattering in random media*, volume 2. Academic press New York, 1978.

[24] Akira Ishimaru. Diffusion of light in turbid material. *Appl. Opt.*, 28(12):2210–2215, 1989.

[25] Simon R Arridge. Optical tomography in medical imaging. *Inverse Probl.*, 15(2):R41–R93, 1999. [doi:10.1088/0266-5611/15/2/022].

[26] Keith D Paulsen and Huabei Jiang. Spatially varying optical property reconstruction using a finite element diffusion equation approximation. *Medical Physics*, 22(6):691–701, 1995.

[27] Hamid Dehghani, Matthew E Eames, Phaneendra K Yalavarthy, Scott C Davis, Subhadra Srinivasan, Colin M Carpenter, Brian W Pogue, and Keith D Paulsen. Near infrared optical tomography using NIRFAST: Algorithm for numerical model and image reconstruction. *Int. J. Numer. Method. Biomed. Eng.*, 25(6):711–732, 2009. [doi:10.1002/cnm.1162].

[28] Huabei Jiang, Brian W Pogue, Michael S Patterson, Keith D Paulsen, and Ulf L Osterberg. Optical image reconstruction using frequency-domain data: simulations and experiments. *JOSA A*, 13(2):253–266, 1996.

[29] Andrei Nikolaevich Tikhonov. Regularization of incorrectly posed problems. In *Soviet Math. Dokl*, volume 4, pages 1624–1627, 1963.

[30] Ann Franchois and Christian Pichot. Microwave imaging-complex permittivity reconstruction with a levenberg-marquardt method. *Antennas and Propagation, IEEE Transactions on*, 45(2):203–215, 1997.

[31] Huabei Jiang, Brian W Pogue, Michael S Patterson, Keith D Paulsen, and Ulf L Osterberg. Simultaneous reconstruction of optical absorption and scattering maps in turbid media from near-infrared frequency-domain data. *Opt. Lett.*, 20(20):2128–2130, 1995.

[32] Phaneendra K Yalavarthy, Brian W Pogue, Hamid Dehghani, and Keith D Paulsen. Weight-matrix structured regularization provides optimal generalized least-squares estimate in diffuse optical tomography. *Med. Phys.*, 34(6):2085–2098, 2007. [doi:10.1118/1.2733803].

[33] Brian W Pogue, Chris Abele, Howard Kaufman, and Keith D Paulsen. Calibration of near-infrared frequency-domain tissue spectroscopy for absolute absorption coefficient quantitation in neonatal head-simulating phantoms. *J. Biomed. Opt.*, 5(2):185–193, 2000.

[34] Ben Brooksby, Shudong Jiang, Hamid Dehghani, Brian W Pogue, Keith D Paulsen, John Weaver, Christine Kogel, and Steven P Poplack. Combining near-infrared tomography and magnetic resonance imaging to study *in vivo* breast tissue: implementation of a Laplacian-type regularization to incorporate magnetic resonance structure. *J. Biomed. Opt.*, 10(5):051504, 2005. [doi:10.1117/1.2098627].

[35] Ben Brooksby, Brian W Pogue, Shudong Jiang, Hamid Dehghani, Subhadra Srinivasan, Christine Kogel, Tor D Tosteson, John Weaver, Steven P Poplack, and Keith D Paulsen. Imaging breast adipose and fibroglandular tissue molecular signatures by using hybrid MRI-guided near-infrared spectral tomography. *Proceedings of the National Academy of Sciences*, 103(23):8828–8833, 2006.

[36] Juan Felipe Perez-Juste Abascal, Juan Aguirre, Judit Chamorro-Servent, Martin Schweiger, Simon Arridge, Jorge Ripoll, Juan J Vaquero, and Manuel Desco. Influence of absorption and scattering on the quantification of fluorescence diffuse optical tomography using normalized data. *J. Biomed. Opt.*, 17(3):0360131–0360139, 2012.

[37] Florian Stuker, Jorge Ripoll, and Markus Rudin. Fluorescence molecular tomography: principles and potential for pharmaceutical research. *Pharmaceutics*, 3(2):229–274, 2011.

[38] T Desmettre, JM Devoisselle, and S Mordon. Fluorescence properties and metabolic features of indocyanine green (ICG) as related to angiography. *Survey of ophthalmology*, 45(1):15–27, 2000.

[39] Chongwei Chi, Yang Du, Jinzuo Ye, Deqiang Kou, Jingdan Qiu, Jiandong Wang, Jie Tian, Xiaoyuan Chen, et al. Intraoperative imaging-guided cancer surgery: from current fluorescence molecular imaging methods to future multi-modality imaging technology. *Theranostics*, 4(11):1072–1084, 2014.

[40] F Fedele, JP Laible, and MJ Eppstein. Coupled complex adjoint sensitivities for frequency-domain fluorescence tomography: theory and vectorized implementation. *J. Comput. Phys.*, 187(2):597–619, 2003. [doi:10.1016/S0021-9991(03)00150-5].

[41] Dianwen Zhu and Changqing Li. Nonuniform update for sparse target recovery in fluorescence molecular tomography accelerated by ordered subsets. *Biomed. Opt. Exp.*, 5(12):4249–4259, 2014. [doi:10.1364/BOE.5.004249].

[42] Dianwen Zhu and Changqing Li. Accelerated image reconstruction in fluorescence molecular tomography using a nonuniform updating scheme with momentum and ordered subsets methods. *J. Biomed. Opt.*, 21(1):016004, 2016. [doi:10.1117/1.JBO.21.1.016004].

[43] Changqing Li, Gregory S Mitchell, Joyita Dutta, Sangtae Ahn, Richard M Leahy, and Simon R Cherry. A three-dimensional multispectral fluorescence optical tomography imaging system for small animals based on a conical mirror design. *Opt. Express*, 17(9):7571–7585, 2009. [doi:10.1364/OE.17.007571].

[44] Dianwen Zhu and Changqing Li. Nonconvex regularizations in fluorescence molecular tomography for sparsity enhancement. *Phys. Med. Biol.*, 59(12):2901–2912, 2014. [doi:10.1088/0031-9155/59/12/2901].

[45] Jeffrey A Fessler, Edward P Ficaro, Neal H Clinthorne, and Kenneth Lange. Grouped-coordinate ascent algorithms for penalized-likelihood transmission image reconstruction. *IEEE Transactions on Medical Imaging*, 16(2):166–175, 1997.

[46] Bruce H Hasegawa, Eric L Gingold, Susan M Reilly, Soo-Chin Liew, and Christopher E Cann. Description of a simultaneous emission-transmission CT system. In *Medical Imaging'90, Newport Beach, 4-9 Feb 90*, pages 50–60. International Society for Optics and Photonics, 1990.

[47] Thomas Beyer, David W Townsend, Tony Brun, Paul E Kinahan, et al. A combined PET/CT scanner for clinical oncology. *The Journal of nuclear medicine*, 41(8):1369, 2000.

[48] Simon R Cherry. Multimodality imaging: Beyond PET/CT and SPECT/CT. In *Seminars in nuclear medicine*, volume 39, pages 348–353. Elsevier, 2009.

[49] Rebecca Fahrig, Kim Butts, John A Rowlands, Rowland Saunders, John Stanton, Grant M Stevens, Bruce L Daniel, Zhifei Wen, David L Ergun, and Norbert J Pelc. A truly hybrid interventional mr/x-ray system: Feasibility demonstration. *Journal of Magnetic Resonance Imaging*, 13(2):294–300, 2001.

[50] George Alexandrakis, Fernando R Rannou, and Arion F Chatziioannou. Tomographic bioluminescence imaging by use of a combined optical-PET (OPET) system: a computer simulation feasibility study. *Phys. Med. Biol.*, 50(17):4225–4241, 2005. [doi:10.1088/0031-9155/50/17/021].

[51] Joseph Culver, Walter Akers, and Samuel Achilefu. Multimodality molecular imaging with combined optical and spect/pet modalities. *J. Nucl. Med*, 49(2):169–172, 2008.

[52] Ben Brooksby, Subhadra Srinivasan, Shudong Jiang, Hamid Dehghani, Brian W Pogue, Keith D Paulsen, John Weaver, Christine Kogel, and Steven P Poplack. Spectral priors improve near-infrared diffuse tomography more than spatial priors. *Opt. Lett.*, 30(15):1968–1970, 2005.

[53] Leon Lapidus and George F Pinder. *Numerical solution of partial differential equations in science and engineering*. John Wiley & Sons, 2011.

[54] Scott C Davis, Kimberley S Samkoe, Julia A OHara, Summer L Gibbs-Strauss, Keith D Paulsen, and Brian W Pogue. Comparing implementations of magnetic-resonance-guided fluorescence molecular tomography for diagnostic classification of brain tumors. *J. Biomed. Opt.*, 15(5):051602–051602, 2010. [doi:10.1117/1.3483902].

[55] Ralf B Schulz, Angelique Ale, Athanasios Sarantopoulos, Marcus Freyer, Eric Soehngen, Marta Zientkowska, and Vasilis Ntziachristos. Hybrid System for Simultaneous Fluorescence and X-Ray Computed Tomography. *IEEE Trans. Med. Imaging*, 29(2):465–473, 2010. [doi:10.1109/TMI.2009.2035310].

[56] Yiyong Tan and Huabei Jiang. Diffuse optical tomography guided quantitative fluorescence molecular tomography. *Appl. Opt.*, 47(12):2011–2016, 2008.

[57] Y Lin, H Gao, O Nalcioglu, and G Gulsen. Fluorescence diffuse optical tomography with functional and anatomical a priori information: feasibility study. *Physics in medicine and biology*, 52(18):5569, 2007.

[58] Yuting Lin, Han Yan, Orhan Nalcioglu, and Gultekin Gulsen. Quantitative fluorescence tomography with functional and structural a priori information. *Appl. Opt.*, 48(7):1328–1336, 2009.

[59] Rebecca L Siegel, Kimberly D Miller, and Ahmedin Jemal. Cancer statistics, 2016. *CA: a cancer journal for clinicians*, 66(1):7–30, 2016.

[60] Laszlo Tabar, Ming-Fang Yen, Bedrich Vitak, Hsiu-Hsi Tony Chen, Robert A Smith, and Stephen W Duffy. Mammography service screening and mortality in breast cancer patients: 20-year follow-up before and after introduction of screening. *The Lancet*, 361(9367):1405–1410, 2003.

[61] MC Segel, DD Paulus, and GN Hortobagyi. Advanced primary breast cancer: assessment at mammography of response to induction chemotherapy. *Radiology*, 169(1):49–54, 1988.

[62] Vilert A Loving, Wendy B DeMartini, Peter R Eby, Robert L Gutierrez, Sue Peacock, and Constance D Lehman. Targeted ultrasound in women younger than 30 years with focal breast signs or symptoms: outcomes analyses and management implications. *American Journal of Roentgenology*, 195(6):1472–1477, 2010.

[63] Debbie Saslow, Carla Boetes, Wylie Burke, Steven Harms, Martin O Leach, Constance D Lehman, Elizabeth Morris, Etta Pisano, Mitchell Schnall,

Stephen Sener, et al. American cancer society guidelines for breast screening with MRI as an adjunct to mammography. *CA: a cancer journal for clinicians*, 57(2):75–89, 2007.

[64] Rene Gilles, Jean-Marc Guinebretière, Caroline Toussaint, Marc Spielman, Marion Rietjens, Jean-Yves Petit, Genevieve Contesso, Jacques Masselot, and Daniel Vanel. Locally advanced breast cancer: contrast-enhanced subtraction mr imaging of response to preoperative chemotherapy. *Radiology*, 191(3):633–638, 1994.

[65] PJ Drew, MJ Kerin, T Mahapatra, C Malone, JRT Monson, LW Turnbull, and JN Fox. Evaluation of response to neoadjuvant chemoradiotherapy for locally advanced breast cancer with dynamic contrast-enhanced MRI of the breast. *European Journal of Surgical Oncology (EJSO)*, 27(7):617–620, 2001.

[66] C Balu-Maestro, C Chapellier, A Bleuse, I Chanalet, C Chauvel, and R Largillier. Imaging in evaluation of response to neoadjuvant breast cancer treatment benefits of MRI. *Breast cancer research and treatment*, 72(2):145–152, 2002.

[67] Brian W Pogue, Shudong Jiang, Hamid Dehghani, Christine Kogel, Sandra Soho, Subhadra Srinivasan, Xiaomei Song, Tor D Tosteson, Steven P Poplack, and Keith D Paulsen. Characterization of hemoglobin, water, and NIR scattering in breast tissue: analysis of intersubject variability and menstrual cycle changes. *J. Biomed. Opt.*, 9(3):541–552, 2004.

[68] Alper Corlu, Turgut Durduran, Regine Choe, Martin Schweiger, Elizabeth MC Hillman, Simon R Arridge, and Arjun G Yodh. Uniqueness and wavelength optimization in continuous-wave multispectral diffuse optical tomography. *Opt. Lett.*, 28(23):2339–2341, 2003. [doi:10.1364/OL.28.002339].

[69] Changqing Li, Hongzhi Zhao, Bonnie Anderson, and Huabei Jiang. Multispectral breast imaging using a ten-wavelength, 64× 64 source/detector channels silicon photodiode-based diffuse optical tomography system. *Med. phys.*, 33(3):627–636, 2006.

[70] Changqing Li, Stephen R Grobmyer, Lin Chen, Qizhi Zhang, Laurie L Fajardo, and Huabei Jiang. Multispectral diffuse optical tomography with absorption and scattering spectral constraints. *Appl. Opt.*, 46(34):8229–8236, 2007. [doi:10.1364/AO.46.008229].

[71] Troy O McBride, Brian W Pogue, Ellen D Gerety, Steven B Poplack, Ulf L Österberg, and Keith D Paulsen. Spectroscopic diffuse optical tomography for the quantitative assessment of hemoglobin concentration and oxygen saturation in breast tissue. *Appl. Opt.*, 38(25):5480–5490, 1999.

[72] Subhadra Srinivasan, Brian W Pogue, Shudong Jiang, Hamid Dehghani, and Keith D Paulsen. Spectrally constrained chromophore and scattering near-infrared tomography provides quantitative and robust reconstruction. *Appl. Opt.*, 44(10):1858–1869, 2005.

[73] Yaling Pei, Harry L Graber, and Randall L Barbour. Normalized–constraint algorithm for minimizing inter–parameter crosstalk in DC optical tomography. *Opt. Express*, 9(2):97–109, 2001. [doi:10.1364/OE.9.000097].

[74] Brian Pogue, Markus Testorf, Troy McBride, Ulf Osterberg, and Keith Paulsen. Instrumentation and design of a frequency-domain diffuse optical tomography imager for breast cancer detection. *Opt. Express*, 1(13):391–403, 1997. [doi:10.1364/OE.1.000391].

[75] Bruce J Tromberg, Olivier Coquoz, Joshua B Fishkin, Tuan Pham, Eric R Anderson, John Butler, Mitchell Cahn, Jeffrey D Gross, Vasan Venugopalan, and David Pham. Non–invasive measurements of breast tissue optical properties using frequency–domain photon migration. *Philosophical Transactions of the Royal Society B: Biological Sciences*, 352(1354):661–668, 1997.

[76] Quing Zhu, Scott H Kurtzman, Poornima Hegde, Susan Tannenbaum, Mark Kane, Minming Huang, Nan Guang Chen, Bipin Jagjivan, and Kristen Zarfos. Utilizing optical tomography with ultrasound localization to image heterogeneous hemoglobin distribution in large breast cancers. *Neoplasia (New York, NY)*, 7(3):263, 2005.

[77] Huabei Jiang, Nicusor V Iftimia, Yong Xu, Julia A Eggert, Laurie L Fajardo, and Karen L Klove. Near-infrared optical imaging of the breast with model-based reconstruction. *Academic radiology*, 9(2):186–194, 2002.

[78] Christoph H Schmitz, Mario Löcker, Joseph M Lasker, Andreas H Hielscher, and Randall L Barbour. Instrumentation for fast functional optical tomography. *Review of Scientific Instruments*, 73(2):429–439, 2002.

[79] Stephanie MWY Van de Ven, Sjoerd G Elias, Andrea J Wiethoff, Marjolein Van der Voort, Tim Nielsen, Bernhard Brendel, Claas Bontus, Falk Uhlemann, Rami Nachabe, Rik Harbers, et al. Diffuse optical tomography of the breast: preliminary findings of a new prototype and comparison with magnetic resonance imaging. *European radiology*, 19(5):1108–1113, 2009.

[80] SB Colak, MB Van der Mark, GW'T Hooft, JH Hoogenraad, ES Van der Linden, and FA Kuijpers. Clinical optical tomography and NIR spectroscopy for breast cancer detection. *Selected Topics in Quantum Electronics, IEEE Journal of*, 5(4):1143–1158, 1999.

[81] JP Culver, R Choe, MJ Holboke, L Zubkov, T Durduran, A Slemp, V Ntziachristos, B Chance, and AG Yodh. Three-dimensional diffuse optical tomography in the parallel plane transmission geometry: evaluation of a hybrid frequency domain/continuous wave clinical system for breast imaging. *Med. phys.*, 30(2):235–247, 2003.

[82] Gordon M Turner, Giannis Zacharakis, Antoine Soubret, Jorge Ripoll, and Vasilis Ntziachristos. Complete-angle projection diffuse optical tomography by use of early photons. *Opt. Lett.*, 30(4):409–411, 2005.

[83] Xavier Intes, Clemence Maloux, Murat Guven, Birzen Yazici, and Britton Chance. Diffuse optical tomography with physiological and spatial a priori constraints. *Physics in medicine and biology*, 49(12):N155, 2004.

[84] Phaneendra K Yalavarthy, Brian W Pogue, Hamid Dehghani, Colin M Carpenter, Shudong Jiang, and Keith D Paulsen. Structural information within regularization matrices improves near infrared diffuse optical tomography. *Opt. Express*, 15(13):8043–8058, 2007. [doi:10.1364/OE.15.008043].

[85] Gregory Boverman, Eric L Miller, Ang Li, Quan Zhang, Tina Chaves, Dana H Brooks, and David A Boas. Quantitative spectroscopic diffuse optical tomography of the breast guided by imperfect a priori structural information. *Physics in medicine and biology*, 50(17):3941, 2005.

[86] Ang Li, Greg Boverman, Yiheng Zhang, Dana Brooks, Eric L Miller, Misha E Kilmer, Quan Zhang, Elizabeth Hillman, and David A Boas. Optimal linear inverse solution with multiple priors in diffuse optical tomography. *Appl. Opt.*, 44(10):1948–1956, 2005.

[87] Brian W Pogue, Scott C Davis, Frederic Leblond, Michael A Mastanduno, Hamid Dehghani, and Keith D Paulsen. Implicit and explicit prior information in near-infrared spectral imaging: accuracy, quantification and diagnostic value. *Philosophical Transactions of the Royal Society of London A: Mathematical, Physical and Engineering Sciences*, 369(1955):4531–4557, 2011.

[88] Qianqian Fang, Juliette Selb, Stefan A Carp, Gregory Boverman, Eric L Miller, Dana H Brooks, Richard H Moore, Daniel B Kopans, and David A Boas. Combined optical and X-ray tomosynthesis breast imaging. *Radiology*, 258(1):89–97, 2011. [doi:10.1148/radiol.10082176].

[89] Qianqian Fang, Stefan A Carp, Juliette Selb, Greg Boverman, Quan Zhang, Daniel B Kopans, Richard H Moore, Eric L Miller, Dana H Brooks, and David A Boas. Combined optical imaging and mammography of the healthy breast: optical contrast derived from breast structure and compression. *IEEE Trans. Med. Imag.*, 28(1):30–42, 2009. [doi:10.1109/TMI.2008.925082].

[90] Vasilis Ntziachristos, AG Yodh, Mitchell D Schnall, and Britton Chance. MRI-guided diffuse optical spectroscopy of malignant and benign breast lesions. *Neoplasia*, 4(4):347–354, 2002. [doi:10.1038/sj.neo.7900244].

[91] Ben A Brooksby, Hamid Dehghani, Brian W Pogue, and Keith D Paulsen. Near-infrared (NIR) tomography breast image reconstruction with a priori structural information from MRI: algorithm development for reconstructing heterogeneities. *IEEE J. Sel. Topics Quantum Electron.*, 9(2):199–209, 2003. [doi:10.1109/JSTQE.2003.813304].

[92] Quing Zhu, Minming Huang, NanGuang Chen, Kristen Zarfos, Bipin Jagjivan, Mark Kane, Poornima Hedge, and Scott H Kurtzman. Ultrasound-guided optical tomographic imaging of malignant and benign breast lesions: initial clinical results of 19 cases. *Neoplasia*, 5(5):379–388, 2003.

[93] John M Boone, Alex LC Kwan, Kai Yang, George W Burkett, Karen K Lindfors, and Thomas R Nelson. Computed Tomography for Imaging the Breast. *J. Mammary Gland Biol. Neoplasia*, 11(2):103–111, 2006. [doi:10.1007/s10911-006-9017-1].

[94] Kai Yang, Alexander LC Kwan, DeWitt F Miller, and John M Boone. A geometric calibration method for cone beam CT systems. *Med. phys.*, 33(6):1695–1706, 2006.

[95] Simon Arridge and John Schotland. Optical tomography: forward and inverse problems. *arXiv preprint arXiv:0907.2586*, 2009.

[96] AP Gibson, JC Hebden, and Simon R Arridge. Recent advances in diffuse optical imaging. *Physics in medicine and biology*, 50(4):R1, 2005.

[97] T Durduran, R Choe, WB Baker, and AG Yodh. Diffuse optics for tissue monitoring and tomography. *Reports on Progress in Physics*, 73(7):076701, 2010.

[98] Changqing Li and Huabei Jiang. A calibration method in diffuse optical tomography. *J. Opt. A Pure Appl. Opt.*, 6(9):844–852, 2004. [doi:10.1088/1464-4258/6/9/005].

[99] Regine Choe, Alper Corlu, Kijoon Lee, Turgut Durduran, Soren D Konecky, Monika Grosicka-Koptyra, Simon R Arridge, Brian J Czerniecki, Douglas L Fraker, Angela DeMichele, et al. Diffuse optical tomography of breast cancer during neoadjuvant chemotherapy: a case study with comparison to mri. *Med. phys.*, 32(4):1128–1139, 2005.

[100] Shudong Jiang, Brian W Pogue, Colin M Carpenter, Steven P Poplack, Wendy A Wells, Christine A Kogel, Jorge A Forero, Lori S Muffly, Gary N

Schwartz, Keith D Paulsen, et al. Evaluation of breast tumor response to neoadjuvant chemotherapy with tomographic diffuse optical spectroscopy: Case studies of tumor region-of-interest changes 1. *Radiology*, 252(2):551–560, 2009.

[101] Dorota B Jakubowski, Albert E Cerussi, Natasha Shah, David Hsiang, John Butler, Bruce J Tromberg, et al. Monitoring neoadjuvant chemotherapy in breast cancer using quantitative diffuse optical spectroscopy: a case study. *J. Biomed. Opt.*, 9(1):230–238, 2004.

[102] Arjun Yodh and Britton Chance. Spectroscopy and imaging with diffusing light. *Phys. Today*, 48(3):34–41, 1995. [doi:10.1063/1.881445].

[103] Colin M Carpenter, Brian W Pogue, Shudong Jiang, Hamid Dehghani, Xin Wang, Keith D Paulsen, Wendy A Wells, Jorge Forero, Christine Kogel, John B Weaver, et al. Image-guided optical spectroscopy provides molecular-specific information *in vivo*: MRI-guided spectroscopy of breast cancer hemoglobin, water, and scatterer size. *Opt. Lett.*, 32(8):933–935, 2007. [doi:10.1364/OL.32.000933].

[104] Changqing Li, Hongzhi Zhao, Bonnie Anderson, and Huabei Jiang. Multispectral breast imaging using a ten-wavelength, 64×64 source/detector channels silicon photodiode-based diffuse optical tomography system. *Med. Phys.*, 33(3):627–636, 2006. [doi:10.1118/1.2171508].

[105] Jeremy C Hebden, Adam Gibson, Rozarina Md Yusof, Nick Everdell, Elizabeth MC Hillman, David T Delpy, Simon R Arridge, Topun Austin, Judith H Meek, and John S Wyatt. Three-dimensional optical tomography of the premature infant brain. *Phys. Med. Biol.*, 47(23):4155–4166, 2002. [doi:10.1088/0031-9155/47/23/303].

[106] David A Boas, Anders M Dale, and Maria Angela Franceschini. Diffuse optical imaging of brain activation: approaches to optimizing image sensitivity, resolution, and accuracy. *Neuroimage*, 23:S275–S288, 2004. [doi:10.1016/j.neuroimage.2004.07.011].

[107] Danial Chitnis, Robert J Cooper, Laura Dempsey, Samuel Powell, Simone Quaggia, David Highton, Clare Elwell, Jeremy C Hebden, and Nicholas L Everdell. Functional imaging of the human brain using a modular, fibreless, high-density diffuse optical tomography system. *Biomed. Opt. Express*, 7(10):4275–4288, 2016. [doi:10.1364/BOE.7.004275].

[108] Vasilis Ntziachristos, AG Yodh, Mitchell Schnall, and Britton Chance. Concurrent MRI and diffuse optical tomography of breast after indocyanine green enhancement. *Proc. Natl. Acad. Sci. U.S.A.*, 97(6):2767–2772, 2000. [doi:10.1073/pnas.040570597].

[109] Regine Choe, Soren D Konecky, Alper Corlu, Kijoon Lee, Turgut Durduran, David R Busch, Saurav Pathak, Brian J Czerniecki, Julia Tchou, Douglas L Fraker, et al. Differentiation of benign and malignant breast tumors by *in-vivo* three-dimensional parallel-plate diffuse optical tomography. *J. Biomed. Opt.*, 14(2):024020, 2009. [doi:10.1117/1.3103325].

[110] Changqing Li and Huabei Jiang. Imaging of particle size and concentration in heterogeneous turbid media with multispectral diffuse optical tomography. *Opt. Express*, 12(25):6313–6318, 2004. [doi:10.1364/OPEX.12.006313].

[111] Dirk Grosenick, Herbert Rinneberg, Rinaldo Cubeddu, and Paola Taroni. Review of optical breast imaging and spectroscopy. *J. Biomed. Opt.*, 21(9):091311, 2016. [doi:10.1117/1.JBO.21.9.091311].

[112] Zhen Jiang, Daqing Piao, Guan Xu, Jerry W Ritchey, G Reed Holyoak, Kenneth E Bartels, Charles F Bunting, Gennady Slobodov, and Jerzy S Krasinki. Trans-rectal ultrasound-coupled near-infrared optical tomography of the prostate part II: Experimental demonstration. *Opt. Express*, 16(22):17505–17520, 2008. [doi:10.1364/OE.16.017505].

[113] Daqing Piao, Kenneth E Bartels, Zhen Jiang, Gilbert Reed Holyoak, Jerry W Ritchey, Guan Xu, Charles F Bunting, and Gennady Slobodov. Alternative transrectal prostate imaging: a diffuse optical tomography method. *IEEE J. Sel. Topics Quantum Electron.*, 16(4):715–729, 2010. [doi:10.1109/JSTQE.2009.2034026].

[114] Jie He, Brian C Wilson, Daqing Piao, and Robert Weersink. Diffuse optical tomography to monitor the photocoagulation front during interstitial photothermal therapy: Numerical simulations and measurements in tissue-simulating phantoms. *Photonics Lasers Med.*, 3(3):241–254, 2014. [doi:10.1515/plm-2014-0011].

[115] Robert A Weersink, Sahil Chaudhary, Kenwrick Mayo, Jie He, and Brian C Wilson. Shape-based reconstruction for transrectal diffuse optical tomography monitoring of photothermal focal therapy of prostate cancer: simulation studies. *J. Biomed. Opt.*, 22(4):045004, 2017. [doi:10.1117/1.JBO.22.4.045004].

[116] Yong Xu, Nicusor Iftimia, Huabei Jiang, L Key, and Marcy Bolster. Imaging of in vitro and in vivo bones and joints with continuous-wave diffuse optical tomography. *Opt. Express*, 8(7):447–451, 2001. [doi:10.1364/OE.8.000447].

[117] Zhen Yuan, Qizhi Zhang, Eric S Sobel, and Huabei Jiang. Tomographic x-ray–guided three-dimensional diffuse optical tomography of osteoarthritis in the finger joints. *J. Biomed. Opt.*, 13(4):044006, 2008. [doi:10.1117/1.2965547].

[118] Martin Schweiger, Simon R Arridge, and Ilkka Nissilä. Gauss–Newton method for image reconstruction in diffuse optical tomography. *Phys. Med. Biol.*, 50(10):2365–2386, 2005. [doi:10.1088/0031-9155/50/10/013].

[119] Alper Corlu, Regine Choe, Turgut Durduran, Kijoon Lee, Martin Schweiger, Simon R Arridge, Elizabeth MC Hillman, and Arjun G Yodh. Diffuse optical tomography with spectral constraints and wavelength optimization. *Appl. Opt.*, 44(11):2082–2093, 2005. [doi:10.1364/AO.44.002082].

[120] Nannan Cao, Arye Nehorai, and Mathews Jacob. Image reconstruction for diffuse optical tomography using sparsity regularization and expectation-maximization algorithm. *Opt. Express*, 15(21):13695–13708, 2007. [doi:10.1364/OE.15.013695].

[121] Haijing Niu, Fenghua Tian, Zi-Jing Lin, and Hanli Liu. Development of a compensation algorithm for accurate depth localization in diffuse optical tomography. *Opt. Lett.*, 35(3):429–431, 2010. [doi:10.1364/OL.35.000429].

[122] Okkyun Lee, Jong Min Kim, Yoram Bresler, and Jong Chul Ye. Compressive diffuse optical tomography: noniterative exact reconstruction using joint sparsity. *IEEE Trans. Med. Imag.*, 30(5):1129–1142, 2011. [doi:10.1109/TMI.2011.2125983].

[123] Jaya Prakash, Calvin B Shaw, Rakesh Manjappa, Rajan Kanhirodan, and Phaneendra K Yalavarthy. Sparse recovery methods hold promise for diffuse optical tomographic image reconstruction. *IEEE J. Sel. Topics Quantum Electron.*, 20(2):74–82, 2014. [doi:10.1109/JSTQE.2013.2278218].

[124] Jaya Prakash, Hamid Dehghani, Brian W Pogue, and Phaneendra K Yalavarthy. Model-resolution-based basis pursuit deconvolution improves diffuse optical tomographic imaging. *IEEE Trans. Med. Imag.*, 33(4):891–901, 2014. [doi:10.1109/TMI.2013.2297691].

[125] Okito Yamashita, Takeaki Shimokawa, Ryota Aisu, Takashi Amita, Yoshihiro Inoue, and Masa-aki Sato. Multi-subject and multi-task experimental validation of the hierarchical bayesian diffuse optical tomography algorithm. *NeuroImage*, 135:287–299, 2016. [doi:10.1016/j.neuroimage.2016.04.068].

[126] Tanmoy Bhowmik, Hanli Liu, Zhou Ye, and Soontorn Oraintara. Dimensionality reduction based optimization algorithm for sparse 3-D image reconstruction in diffuse optical tomography. *Sci. Rep.*, 6:22242, 2016. [doi:10.1038/srep22242].

[127] Calvin B Shaw, Zhiqiu Li, Brian W Pogue, and Phaneendra K Yalavarthy. Direct sensitivity based data-optimization strategy for image-guided diffuse optical tomography. *IEEE J. Sel. Topics Quantum Electron.*, 22(3):69–77, 2016. [doi:10.1109/JSTQE.2016.2558178].

[128] Zhonghua Sun, Yaqi Wang, Kebin Jia, and Jinchao Feng. Comprehensive study of methods for automatic choice of regularization parameter for diffuse optical tomography. *Opt. Eng.*, 56(4):041310–041310, 2017. [doi:10.1117/1.OE.56.4.041310].

[129] Brian W Pogue and Keith D Paulsen. High-resolution near-infrared tomographic imaging simulations of the rat cranium by use of a priori magnetic resonance imaging structural information. *Opt. Lett.*, 23(21):1716–1718, 1998. [doi:10.1364/OL.23.001716].

[130] Yan Zhao, Michael A Mastanduno, Shudong Jiang, EI-Ghussein Fadi, Jiang Gui, Brian W Pogue, and Keith D Paulsen. Optimization of image reconstruction for magnetic resonance imaging–guided near-infrared diffuse optical spectroscopy in breast. *J. Biomed. Opt.*, 20(5):056009, 2015. [doi:10.1117/1.JBO.20.5.056009].

[131] Vasilis Ntziachristos, XuHui Ma, and Britton Chance. Time-correlated single photon counting imager for simultaneous magnetic resonance and near-infrared mammography. *Rev. Sci. Instrum.*, 69(12):4221–4233, 1998. [doi:10.1063/1.1149235].

[132] Quing Zhu, Edward B Cronin, Allen A Currier, Hugh S Vine, Minming Huang, NanGuang Chen, and Chen Xu. Benign versus malignant breast masses: Optical differentiation with US-guided optical imaging reconstruction. *Radiology*, 237(1):57–66, 2005. [doi:10.1148/radiol.2371041236].

[133] Quing Zhu, Susan Tannenbaum, and Scott H Kurtzman. Optical tomography with ultrasound localization for breast cancer diagnosis and treatment monitoring. *Surg. Oncol. Clin. N. Am.*, 16(2):307–321, 2007. [doi:10.1016/j.soc.2007.03.008].

[134] Yan Xu and Quing Zhu. Estimation and imaging of breast lesions using a two-layer tissue structure by ultrasound-guided optical tomography. *J. Biomed. Opt.*, 20(6):066002, 2015. [doi:10.1117/1.JBO.20.6.066002].

[135] Limin Zhang, Yan Zhao, Shudong Jiang, Brian W Pogue, and Keith D Paulsen. Direct regularization from co-registered anatomical images for MRI-guided near-infrared spectral tomographic image reconstruction. *Biomed. Opt. Express*, 6(9):3618–3630, 2015. [doi:10.1364/BOE.6.003618].

[136] Jinchao Feng, Shudong Jiang, Junqing Xu, Yan Zhao, Brian W Pogue, and Keith D Paulsen. Multiobjective guided priors improve the accuracy of near-infrared spectral tomography for breast imaging. *J. Biomed. Opt.*, 21(9):090506, 2016. [doi:10.1117/1.JBO.21.9.090506].

[137] Murad Althobaiti, Hamed Vavadi, and Quing Zhu. Diffuse optical tomography reconstruction method using ultrasound images as prior for regularization matrix. *J. Biomed. Opt.*, 22(2):026002, 2017. [doi:10.1117/1.JBO.22.2.026002].

[138] Guobao Wang and Jinyi Qi. PET Image Reconstruction Using Kernel Method. *IEEE Trans. Med. Imag.*, 34(1):61–71, 2015. [doi:10.1109/tmi.2014.2343916].

[139] Guobao Wang and Jinyi Qi. PET image reconstruction using kernel method. In *2013 IEEE 10th International Symposium on Biomedical Imaging*, pages 1162–1165. IEEE, 2013. [doi:10.1109/ISBI.2013.6556686].

[140] Will Hutchcroft, Guobao Wang, Kevin T Chen, Ciprian Catana, and Jinyi Qi. Anatomically-aided PET reconstruction using the kernel method. *Phys. Med. Biol.*, 61(18):6668–6683, 2016. [doi:10.1088/0031-9155/61/18/6668].

[141] Alain Berlinet and Christine Thomas-Agnan. *Reproducing Kernel Hilbert Spaces in Probability and Statistics*. Springer Science, 2004. [doi:10.1007/978-1-4419-9096-9].

[142] Thomas Hofmann, Bernhard Schölkopf, and Alexander J Smola. Kernel methods in machine learning. *Ann. Stat.*, 36(3):1171–1220, 2008. [doi:10.1214/009053607000000677].

[143] Dianwen Zhu, Yue Zhao, Reheman Baikejiang, Zhen Yuan, and Changqing Li. Comparison of regularization methods in fluorescence molecular tomography. *Photonics*, 1(2):95–109, 2014. [doi:10.3390/photonics1020095].

[144] Reheman Baikejiang, Wei Zhang, and Changqing Li. Diffuse optical tomography for breast cancer imaging guided by computed tomography: A feasibility study. *J. Xray. Sci. Technol.*, 25(3):341–355, 2017. [doi:10.3233/XST-16183].

[145] Reheman Baikejiang, Wei Zhang, Dianwen Zhu, and Changqing Li. CT guided diffuse optical tomography for breast cancer imaging. In *Proc. SPIE*, volume 9788, page 97882K, 2016. [doi:10.1117/12.2216402].

[146] Ben Brooksby, Shudong Jiang, Hamid Dehghani, Brian W Pogue, Keith D Paulsen, Christine Kogel, Marvin Doyley, John B Weaver, and Steven P Poplack. Magnetic resonance-guided near-infrared tomography of the breast. *Rev. Sci. Instrum.*, 75(12):5262–5270, 2004. [doi:10.1063/1.1819634].

[147] Changqing Li, Yongfeng Yang, Gregory S Mitchell, and Simon R Cherry. Simultaneous PET and multispectral 3-Dimensional fluorescence optical tomography imaging system. *J. Nucl. Med.*, 52(8):1268–1275, 2011. [doi:10.2967/jnumed.110.082859].

[148] Yibao Wu, Spencer L Bowen, Kai Yang, Nathan Packard, Lin Fu, George Burkett Jr, Jinyi Qi, John M Boone, Simon R Cherry, and Ramsey D Badawi. PET characteristics of a dedicated breast PET/CT scanner prototype. *Phys. Med. Biol.*, 54(13):4273, 2009. [doi:10.1088/0031-9155/54/13/020].

[149] Simon R Cherry. *In vivo* molecular and genomic imaging: new challenges for imaging physics. *Phys. Med. Biol.*, 49(3):R13–R48, 2004. [doi:10.1088/0031-9155/49/3/R01].

[150] Vasilis Ntziachristos, Jorge Ripoll, Lihong V Wang, and Ralph Weissleder. Looking and listening to light: the evolution of whole-body photonic imaging. *Nat. Biotechnol.*, 23(3):313–320, 2005. [doi:10.1038/nbt1074].

[151] Scott C Davis, Kimberley S Samkoe, Julia A O'Hara, Summer L Gibbs-Strauss, Hannah L Payne, P Jack Hoopes, Keith D Paulsen, and Brian W Pogue. MRI-coupled fluorescence tomography quantifies EGFR activity in brain tumors. *Acad. Radiol.*, 17(3):271–276, 2010. [doi:10.1016/j.acra.2009.11.001].

[152] Xiaolian Guo, Xin Liu, Xin Wang, Feng Tian, Fei Liu, Bin Zhang, Guangshu Hu, and Jing Bai. A combined fluorescence and microcomputed tomography system for small animal imaging. *IEEE Trans. Biomed. Eng.*, 57(12):2876–2883, 2010. [doi:10.1109/TBME.2010.2073468].

[153] Scott C Davis, Kimberley S Samkoe, Kenneth M Tichauer, Kristian J Sexton, Jason R Gunn, Sophie J Deharvengt, Tayyaba Hasan, and Brian W Pogue. Dynamic dual-tracer MRI-guided fluorescence tomography to quantify receptor density in vivo. *Proc. Natl. Acad. Sci. U.S.A*, 110(22):9025–9030, 2013. [doi:10.1073/pnas.1213490110].

[154] Yue Zhang, Bin Zhang, Fei Liu, Jianwen Luo, and Jing Bai. In vivo tomographic imaging with fluorescence and MRI using tumor-targeted dual-labeled nanoparticles. *Int. J. Nanomedicine*, 9(1):33–41, 2014. [doi:10.2147/IJN.S52492].

[155] Angelique Ale, Vladimir Ermolayev, Eva Herzog, Christian Cohrs, Martin Hrabé De Angelis, and Vasilis Ntziachristos. FMT-XCT: *in vivo* animal studies with hybrid fluorescence molecular tomography-X-ray computed tomography. *Nat. Methods*, 9(6):615–620, 2012. [doi:10.1038/nmeth.2014].

[156] Xiaopeng Ma, Jaya Prakash, Francesca Ruscitti, Sarah Glasl, Fabio Franco Stellari, Gino Villetti, and Vasilis Ntziachristos. Assessment of asthmatic inflammation using hybrid fluorescence molecular tomography–x-ray computed tomography. *J. Biomed. Opt.*, 21(1):015009–015009, 2016. [10.1117/1.JBO.21.1.015009].

[157] Alper Corlu, Regine Choe, Turgut Durduran, Mark A Rosen, Martin Schweiger, Simon R Arridge, Mitchell D Schnall, and Arjun G Yodh. Three-dimensional *in vivo* fluorescence diffuse optical tomography of breast cancer in humans. *Opt. Express*, 15(11):6696–6716, 2007. [doi:10.1364/OE.15.006696].

[158] Scott C Davis, Hamid Dehghani, Jia Wang, Shudong Jiang, Brian W Pogue, and Keith D Paulsen. Image-guided diffuse optical fluorescence tomography implemented with Laplacian-type regularization. *Opt. Express*, 15(7):4066–4082, 2007. [doi:10.1364/OE.15.004066].

[159] Anuradha Godavarty, Alan B Thompson, Ranadhir Roy, Mikhail Gurfinkel, Margaret J Eppstein, Chaoyang Zhang, and Eva Marie Sevick-Muraca. Diagnostic imaging of breast cancer using fluorescence-enhanced optical tomography: phantom studies. *J. Biomed. Opt.*, 9(3):488–496, 2004. [doi:10.1117/1.1691027].

[160] Nicolas Ducros, Cosimo D'andrea, Gianluca Valentini, Tim Rudge, Simon Arridge, and Andrea Bassi. Full-wavelet approach for fluorescence diffuse optical tomography with structured illumination. *Opt. Lett.*, 35(21):3676–3678, 2010. [doi:10.1364/OL.35.003676].

[161] Joyita Dutta, Sangtae Ahn, Anand A Joshi, and Richard M Leahy. Illumination pattern optimization for fluorescence tomography: theory and simulation studies. *Phys. Med. Biol.*, 55(10):2961–2982, 2010. [doi:10.1088/0031-9155/55/10/011].

[162] Vasilis Ntziachristos, Ching-Hsuan Tung, Christoph Bremer, and Ralph Weissleder. Fluorescence molecular tomography resolves protease activity *in vivo*. *Nat. Med.*, 8(7):757–761, 2002. [doi:10.1038/nm729].

[163] Nikolaos Deliolanis, Tobias Lasser, Damon Hyde, Antoine Soubret, Jorge Ripoll, and Vasilis Ntziachristos. Free-space fluorescence molecular tomography utilizing 360geometry projections. *Opt. Lett.*, 32(4):382–384, 2007. [doi:10.1364/OL.32.000382].

[164] Jong Hwan Lee, Hyun Keol Kim, Chandhanarat Chandhanayingyong, Francis Young-In Lee, and Andreas H Hielscher. Non-contact small animal fluorescence imaging system for simultaneous multi-directional angular-dependent data acquisition. *Biomed. Opt. Exp.*, 5(7):2301–2316, 2014. [doi:10.1364/BOE.5.002301].

[165] Daifa Wang, Jin He, Huiting Qiao, Ping Li, Yubo Fan, and Deyu Li. Non-contact full-angle fluorescence molecular tomography system based on rotary mirrors. *Appl. Opt.*, 54(23):7062–7070, 2015. [doi:10.1364/AO.54.007062].

[166] Joyita Dutta, Sangtae Ahn, Changqing Li, Simon R Cherry, and Richard M Leahy. Joint L^1 and total variation regularization for fluorescence molecular tomography. *Phys. Med. Biol.*, 57(6):1459–1476, 2012. [doi:10.1088/0031-9155/57/6/1459].

[167] Huangjian Yi, Duofang Chen, Wei Li, Shouping Zhu, Xiaorui Wang, Jimin Liang, and Jie Tian. Reconstruction algorithms based on l1-norm and l2-norm for two imaging models of fluorescence molecular tomography: a comparative study. *J. Biomed. Opt.*, 18(5):056013, 2013. [doi:10.1117/1.JBO.18.5.056013].

[168] Yu An, Jie Liu, Guanglei Zhang, Jinzuo Ye, Yamin Mao, Shixin Jiang, Wenting Shang, Yang Du, Chongwei Chi, and Jie Tian. Meshless reconstruction method for fluorescence molecular tomography based on compactly supported radial basis function. *J. Biomed. Opt.*, 20(10):105003–105003, 2015. [doi:10.1117/1.JBO.20.10.105003].

[169] Sedigheh Marjaneh Hejazi, Saeed Sarkar, and Ziba Darezereshki. Fast multislice fluorescence molecular tomography using sparsity-inducing regularization. *J. Biomed. Opt.*, 21(2):026012–026012, 2016. [doi:10.1117/1.JBO.21.2.026012].

[170] Jiulou Zhang, Junwei Shi, Huizhi Guang, Simin Zuo, Fei Liu, Jing Bai, and Jianwen Luo. Iterative correction scheme based on discrete cosine transform and l1 regularization for fluorescence molecular tomography with background fluorescence. *IEEE Trans. Biomed. Eng.*, 63(6):1107–1115, 2016. [doi:10.1109/TBME.2015.2483539].

[171] Yu An, Jie Liu, Guanglei Zhang, Jinzuo Ye, Yang Du, Yamin Mao, Chongwei Chi, and Jie Tian. A novel region reconstruction method for fluorescence molecular tomography. *IEEE Trans. Biomed. Eng.*, 62(7):1818–1826, 2015. [doi:10.1109/TBME.2015.2404915].

[172] Xuanxuan Zhang, Jiulou Zhang, Jing Bai, and Jianwen Luo. Shape-based reconstruction of dynamic fluorescent yield with a level set method. *Biomed. Eng. Online*, 15(1):6, 2016. [doi:10.1186/s12938-016-0124-y].

[173] Frederic Leblond, Scott C Davis, Pablo A Valdés, and Brian W Pogue. Pre-clinical whole-body fluorescence imaging: Review of instruments, methods and applications. *J. Photochem. Photobiol. B: Bio*, 98(1):77–94, 2010. [doi:10.1016/j.jphotobiol.2009.11.007].

[174] Scott C Davis, Brian W Pogue, Roger Springett, Christoph Leussler, Peter Mazurkewitz, Stephen B Tuttle, Summer L Gibbs-Strauss, Shudong S Jiang, Hamid Dehghani, and Keith D Paulsen. Magnetic resonance–coupled

fluorescence tomography scanner for molecular imaging of tissue. *Rev. Sci. Instrum.*, 79(6):064302, 2008. [doi:10.1063/1.2919131].

[175] Changqing Li, Guobao Wang, Jinyi Qi, and Simon R Cherry. Three-dimensional fluorescence optical tomography in small-animal imaging using simultaneous positron-emission-tomography priors. *Opt. Lett.*, 34(19):2933–2935, 2009. [doi:10.1364/OL.34.002933].

[176] Angelique Ale, Ralf B Schulz, Athanasios Sarantopoulos, and Vasilis Ntziachristos. Imaging performance of a hybrid x-ray computed tomography-fluorescence molecular tomography system using priors. *Med. Phys.*, 37(5):1976–1986, 2010. [doi:10.1118/1.3368603].

[177] Florian Stuker, Christof Baltes, Katerina Dikaiou, Divya Vats, Lucio Carrara, Edoardo Charbon, Jorge Ripoll, and Markus Rudin. Hybrid small animal imaging system combining magnetic resonance imaging with fluorescence tomography using single photon avalanche diode detectors. *IEEE Trans. Med. Imag.*, 30(6):1265–1273, 2011. [doi:10.1109/TMI.2011.2112669].

[178] Joerg Peter, Daniel Unholtz, Ralf B Schulz, Josef Doll, and Wolfhard Semmler. Development and Initial Results of a Tomographic Dual-Modality Positron/Optical Small Animal Imager. *IEEE Trans. Nucl. Sci.*, 54(5):1553–1560, 2007. [doi:10.1109/TNS.2007.902359].

[179] Yuting Lin, William C Barber, Jan S Iwanczyk, Werner Roeck, Orhan Nalcioglu, and Gultekin Gulsen. Quantitative fluorescence tomography using a combined tri-modality ft/dot/xct system. *Opt. Express*, 18(8):7835–7850, 2010. [doi:10.1364/OE.18.007835].

[180] Muhan Liu, Hongbo Guo, Hongbo Liu, Zeyu Zhang, Chongwei Chi, Hui Hui, Di Dong, Zhenhua Hu, and Jie Tian. In vivo pentamodal tomographic imaging for small animals. *Biomed. Opt. Exp.*, 8(3):1356–1371, 2017. [doi:10.1364/BOE.8.001356].

[181] Robert W Holt, Scott Davis, and Brian W Pogue. Regularization functional semi-automated incorporation of anatomical prior information in image-guided fluorescence tomography. *Opt. Lett.*, 38(14):2407–2409, 2013. [10.1364/OL.38.002407].

[182] Bernhard Schölkopf, Alexander Smola, and Klaus-Robert Müller. Kernel principal component analysis. In *International Conference on Artificial Neural Networks*, pages 583–588. Springer, 1997. [doi:110.1007/BFb0020217].

[183] Yanhua Wang and Leslie Ying. Undersampled dynamic magnetic resonance imaging using kernel principal component analysis. In *Engineering in Medicine and Biology Society, 2014 36th Annual International Conference of the IEEE*, pages 1533–1536. IEEE, 2014. [doi:10.1109/embc.2014.6943894].

[184] F Nouizi, H Erkol, A Luk, M Marks, MB Unlu, and G Gulsen. An accelerated photo-magnetic imaging reconstruction algorithm based on an analytical forward solution and a fast jacobian assembly method. *Phys. Med. Biol.*, 61(20):7448, 2016. [10.1088/0031-9155/61/20/7448].

[185] Yue Zhao, Reheman Baikejiang, and Changqing Li. Application of kernel method in fluorescence molecular tomography. In *Proc. SPIE*, volume 10057, page 100570P, 2017. [doi:10.1117/12.2252782].

[186] Yue Zhao, Wei Zhang, Dianwen Zhu, and Changqing Li. Optimization and performance evaluation of a conical mirror based fluorescence molecular tomography imaging system. In *SPIE Medical Imaging*, pages 97880R–97880R. International Society for Optics and Photonics, 2016. [doi:10.1117/12.2216523].

[187] Qianqian Fang and David A Boas. Tetrahedral mesh generation from volumetric binary and grayscale images. In *Proceedings of IEEE International Symposium on Biomedical Imaging: From Nano to Macro*, pages 1142–1145. IEEE, 2009. [doi:10.1109/ISBI.2009.5193259].

[188] Yue Zhao, Dianwen Zhu, Reheman Baikejiang, and Changqing Li. 3D mouse shape reconstruction based on phase-shifting algorithm for fluorescence molecular tomography imaging system. *Appl. Opt.*, 54(32):9573–9582, 2015. [doi:10.1364/AO.54.009573].

[189] Michael C Lun, Wei Zhang, and Changqing Li. Sensitivity study of X-ray luminescence computed tomography. *Appl. Opt.*, 56(11):3010–3019, 2017. [doi:10.1364/AO.56.003010].

[190] Benjamin Spencer, Jinyi Qi, Ramsey D Badawi, and Guobao Wang. Dynamic pet image reconstruction for parametric imaging using the hypr kernel method. In *SPIE Medical Imaging*, page 101324W. International Society for Optics and Photonics, 2017.

[191] Hu Chen, Yi Zhang, Weihua Zhang, Peixi Liao, Ke Li, Jiliu Zhou, and Ge Wang. alow-dose ct via convolutional neural network. *Biomed. Opt. Express*, 8(2):679–694, 2017.